# Superconducting Proximity Effect in Graphene Nanodevices:
# A Transport and Tunneling Study

A dissertation presented
by

I-JAN WANG

to

The School of Engineering and Applied Sciences

in partial fulfillment of the requirements
for the degree of
Doctor of Philosophy
in the subject of

Applied Physics

Harvard University

Cambridge, Massachusetts

December 2015

Dissertation Advisor: Professor Pablo Jarillo-Herrero I-Jan Wang

# Superconducting Proximity Effect in Graphene Nanodevices:

# A Transport and Tunneling Study

## Abstract

Provided that it is in good electrical contact with a superconductor, a normal metal can acquire superconducting properties when the temperature is low enough. Known as the superconducting proximity effect, this phenomenon has been studied for more than 50 years and, because of the richness of its physics, continues to fascinate many scientists.

In this thesis, we present our study of the superconducting proximity effect in a hybrid system made by bringing graphene, a monolayer of carbon atoms arranged in a hexagonal lattice, into contact with metallic BCS superconductors. Here graphene plays two roles: First it is a truly 2-dimensional crystal whose electron gas can be accessed on the surface easily. This property allows both transparent electrical contact with superconductors and direct observation of electronic properties made by a variety of probing schemes. Second, with its unique gapless band structure and linear energy dispersion, graphene provides a platform for the study of superconductivity carried by Dirac fermions.

Graphene's first role may facilitate endeavors to reach a deeper understanding of proximity effects. However, it is predicted that in its second role graphene may give rise to exotic phenomena in superconducting regime.

In order to realize these potentials, it is crucial to have good control of this material in regard to both fabrication and characterization. Two key elements have been recognized as necessary in fabrication: a graphene device with low disorder and a large induced gap in the normal region. In addition, a deeper understanding of the microscopic mechanism of supercurrent transport in graphene or any 2-dimensional system in general, is bound to provide a basis for abundant insights or may even produce surprises.

The research discussed in this thesis has been shaped by this overall approach. An introduction to the basic electronic properties of graphene is given in Chapter 1, which presents the band structure of graphene based on a tight-binding model. In addition, gate-tunability and the chiral nature of Dirac fermions in graphene, both of which are essential in our experiments, are also discussed.

Chapter 2 provides a theoretical background to superconductivity, with an emphasis on its manifestation in inhomogeneous systems at the mesoscopic scale. The Andreev reflection, the phase-coherent transport of particles coupled by superconductors, and the corresponding energy bound states (Andreev bound states) are studied in long- and short-junction limits. We will also show how the existence of impurity affects the physics presented in our experiments.

Chapter 3 demonstrates the first graphene-based superconducting devices that we investigated. Fabrication and low-temperature measurement techniques of SGS junctions made of graphene and NbN, a type II superconductor with a large gap ($T_C \sim 12K$) and a large critical field ($H_{C2}$> 9T ) are also discussed.

Chapter 4 focuses on the development of h-BN-encapsulated graphene Josephson junctions. The pick-up and transfer techniques for the 2-dimensional Van der Waals materials that we used to make these heterostructures are described in details. The device we fabricated in this way exhibits ballistic transport characteristics, i.e. the signs of low disorder in graphene, in both normal and superconducting regimes.

In Chapter 5, the tunneling spectroscopy of supercurrent-carrying Andreev states is presented. In order to study the intrinsic properties of the sample, we developed a new fabrication scheme aiming at preserving the pristine nature of the 2-DEGS as well as to minimize the doping introduced by external probes. The tunneling spectroscopy of graphene in superconducting regime reveals not only the Andreev bound states in the 2-dimensional limit, but also what we call the "Andreev scattering state" in the energy continuum.

# CONTENTS

# LIST OF FIGURES

## LIST OF TABLES

---

*The moon, by her comparative proximity,*
*and the constantly varying appearances produced by her several phases,*
*has always occupied a considerable share of the attention*
*of the inhabitants of the earth..*

— Jules Verne

# ACKNOWLEDGMENTS

---

After giving the interview presentation to my advisor, Prof. Pablo Jarillo-Herrero, we had dinner together at Porter square in Cambridge. My last question for him was: why is the existence of Josephson effect in graphene so important? With that, I was referring to the beautiful experiment that Pablo had performed in Delft University[70].

The results reported in the thesis demonstrate what I have learned about this topic. I would like to thank Pablo for taking me in this group, so I have the opportunity to purse the answer this question I have had when we first met. I also want to thank Pablo for his guidance and patience, as my Ph.D. project has a long and convoluted life. Pablo's enthusiasm and insight for science inspires me in many aspects, and has led to the successful completion of the thesis.

I would like to thank the members of my committee, Prof. Robert Westervelt, Prof. Jenny Hoffman and Prof. Zhigang Suo for their advice over the years.

It is a great pleasure to work on the project with many inspired individuals. Thanks to Michele Zaffalon for introducing me to the nanofabrication and low temperature measurement techniques, which had become the most important tools during my research. Two talented UROP (Undergraduate Research Opportunities Program) students contributed essential components to our project: Haofei Wei helped me to set up the filtering system in our cryofree dil. fridge; and Yu-An Chen successfully worked out the first dry polymer pick-up recipe for patterned h-BN (I confess I did not quite believe it would work when I first described the idea, but you amazed us!). Patrick Back, then a visiting student from EPFL, came with a strong passion and an unlimited supply of Swiss chocolate truffle, joined me at a time when there was uncertainty about the future direction of the project. His genuine belief in using the PC polymer led to our success in manipulating the ultra-thin h-BN, which resulted in our determination to keep working on the project of tunneling spectroscopy.

I feel very honored to work with Landry Bretheau. He not only teaches me so much about superconductivity but also shares the passion for food with me. Working on mesoscopic superconductivity experiments, especially when the cryo-free fridge is not always problem-free, can sometimes be depressing. The tedious work, such as fixing a pump in the basement or locating the ground-loop in our measurement rack, became far more bearable when seasoned with conversations about oyster or tajine. Thank you Riccardo for taking the responsibility of fabricating our devices while I was busy writing this thesis. I feel that I have deposited in you all my fabrication techniques, and they have been transformed and elevated to another level. Now I am excited to learn the evolved techniques from you, feeling like a wine maker prepared to taste the newest vintage of a Barolo from the barrel.

Working in Jarillo-Herrero lab is truly an intellectually and emotionally rewarding experience, and I attribute this to our group members. Thank you all for enriching my life during this journey. I am very lucky to have Ms. Monica Wolf, our assistant, for helping me with the administrative procedures. Her help is especially crucial to a Harvard student working at MIT. I would also like to express my appreciation for the Ray Ashoori's, Jing Kong's and Karl Berggren's groups for assistance to our research.

Wei, thank you for always being by my side: by doing so from 200 miles away, you have taught me about long-range phase correlation beyond the theory of superconductivity. Thanks to my parents and my sister's family for always being my source of strength. None of this would have been possible without you, I love you.

*Dedicated to my family*

# 1

# INTRODUCTION TO ELECTRONIC PROPERTIES OF GRAPHENE

Highly conductive, transparent, ambipolar, tunable, strong, flexible, light, thin, atomically flat, chemically inert, mechanically robust, and even compatible with biological entities, these are just a few of the properties that have been ascribed to graphene since it was first experimentally realized in 2004[97].

Given its versatility, graphene has drawn tremendous attentions from scientists and engineers from a range of backgrounds. Further, graphene sciences together with associated techniques span multiple fields such as nanofabrication, material growth, sample treatment, and device characterization, such that a foundation has been laid for an even broader field of research: that is, the 2-dimensional Van der Waals heterostructures[55], which significantly exceed graphene in terms of complexity and functionality.

This thesis focuses on the electronic properties that graphene acquires when it is attached to superconductors. Thus it is important to understand the intrinsic electronic properties of graphene before it forms a hybrid system with superconductors. We will discuss some of the basic electronic properties of graphene that motivated the present research, and provide a practical perspective on identifying the elements essential to realizing graphene's uses in a broader scientific and engineering landscape.

## 1.1 INTRODUCTION AND CARBON ALLOTROPES

One of the most abundant elements in nature, carbon is found in all kinds of materials. Owing to its flexibility in bonding, carbon forms countless kinds of molecules or compounds, which constitute the basis of organic chemistry and of all biological entities. Even when restricted to bonding to each other, carbon atoms form an orderly arrangement. That is, carbon atoms form crystals, and these crystals differ in regard to structure and dimensionality.

In the world of nanoscale electronics, graphene, a monolayer of carbon crystal arranged in a hexagonal lattice, was studied experimentally much later than other kinds of carbon crystals, yet it may be regarded as the most fundamental type of carbon allotrope. Fullerene, the spherically packed carbon atoms, can be obtained by wrapping-up a graphene sheet with the introduction of pentagons, behaves like a zero-dimensional object with discrete energy levels. Rolling up a graphene sheet and connecting the carbon atoms at the edges results in the carbon nanotube that is essentially a one-dimensional object. Graphite is probably the best known, and most commonly used carbon allotrope since the invention of the pencil in 1500's, which consists of a three-dimensional stack of graphene sheets.

The ease and smoothness that people have enjoyed for hundreds of years when writing with a pencil is rooted in the electronic structure, and therefore the bonding characteristics of graphene. Specifically, graphene has strong in-plane covalent bonding between carbon atoms, and couples weakly to its neighboring layer in the perpendicular direction via Van der Waals forces. It is this contrast between the robustness of graphene's bondings that makes it possible to write easily with graphite, which would separate into thin layers when a pencil is pressed against a piece of paper.

In a 1946 paper[125] P.R. Wallace used graphene as the starting point to calculate the band structure of graphite. His idea was that the inter-layer coupling would be weak enough to allow each graphene layer to be treated independently. At that time, producing an isolated graphene sheet was not considered possible. Instead, he graphene sheet was posited as a model system for theoretical construction due to the instability of this form of two-dimension carbon crystals[56, 57], as well as the difficulty of obtaining graphene in experiments.

In 2004, Andre Geim and Kanstantin Novoselov showed that graphene can easily be produced by mechanically exfoliating graphite using sticky tapes[97]. They also demonstrated that when depositing graphene on an $SiO_2$ substrate with proper thickness (285 nm) provides a good optical contrast, which enables single layer graphene to be identified with an optical microscope. This discovery opened the door to the experimental study of this "old" material that had been a subject of intensive theoretical investigation for many years.

The most noteworthy feature of graphene is its low energy excitation band structure. In this regime, the energy dispersion is linear and the behavior of the charge carriers mimics that of massless relativistic particles, the dynamics of which are described by the Dirac equation. We will discuss these unique properties and their implications in the following sections.

## 1.2 BAND STRUCTURE OF GRAPHENE

### 1.2.1 *A tight-binding approach*

We introduce the band structure of graphene, which is the foundation of the electronic properties of the crystal, in the frame work of a tight-binding model. Monolayer graphene is a 2-dimensional carbon

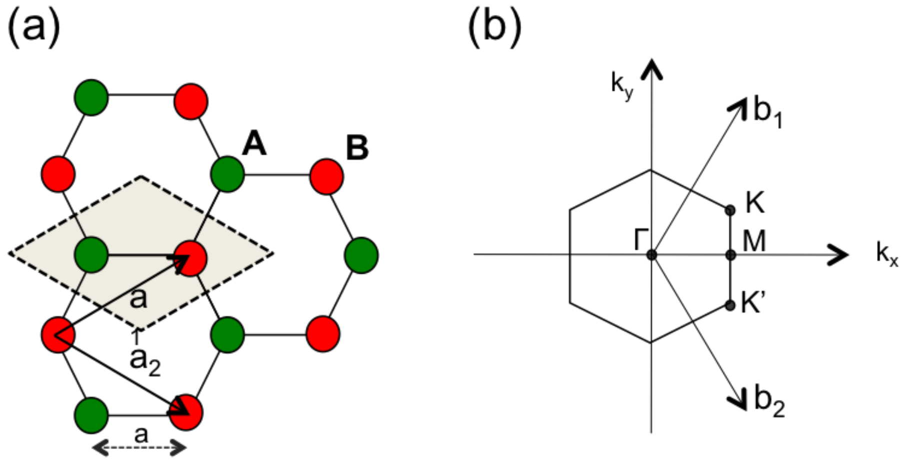

Figure 1.1: The hexagonal lattice of graphene in (a) real and (b) momentum space.

crystal arranged in a hexagonal lattice (Fig. 1.1 (a)). Here the lattice axes selected are:

$$\boldsymbol{a_1} = \frac{a}{2}(3, \sqrt{3}), \quad \boldsymbol{a_2} = \frac{a}{2}(3, -\sqrt{3}) \tag{1.1}$$

,where $a\sim$ 1.42$\AA$ is the distance between the carbon atoms that are nearest to each other, with respect to the coordinate shown in Figure 1.1. The dashed-line depicts a unit cell, which contains two identical carbon atoms that belong to two equivalent sublattices, denoted by A and B. Figure 1.1(b) shows the first Brillouin zone of the graphene lattice in momentum space. The first Brillouin zone is also a hexagon with some symmetry points labeled K, K′, M and Γ. Of particular interest are points $\boldsymbol{K}$ and $\boldsymbol{K'}$ at the corners given by

$$\boldsymbol{K} = \left(\frac{2\pi}{3a}, \frac{2\pi}{3a\sqrt{3}}\right), \quad \boldsymbol{K'} = \left(\frac{2\pi}{3a}, -\frac{2\pi}{3a\sqrt{3}}\right) \ . \tag{1.2}$$

As we will see, these points give rise to the unique electronic properties of graphene in the low energy regime. The tight-binding model under discussion herein is based on the assumption that an electron can only hop to the nearest neighbors with characteristic energy t (the hopping energy). Hence for the $p_z$ electron of sublattice $A$, the only relevant potential is given by three surrounding carbon atoms from sublattice $B$. The Hamiltonian in the second quantization formalism can be written as:

$$H = -t \sum_{\langle i,j\rangle,\sigma} \left(a^{\dagger}_{i,\sigma} b_{j,\sigma} + h.c\right), \tag{1.3}$$

where $a^{\dagger}_{i,\sigma}(b_{j,\sigma})$ creates (annihilates) an electron at the $\boldsymbol{R}_i$ ($\boldsymbol{R}_j$) site of sublattice $A$(sublattice $B$), with spin $\sigma$ ($\sigma =\uparrow$ *or* $\downarrow$). The hopping energy $t$ in graphene is about 2.8 eV.

Energy band $E(k)$ can be obtained by expanding the electron field operators in the $k$-space as:

$$a_{i,\sigma} = \frac{1}{\sqrt{N_c}} \sum_{\boldsymbol{k}} e^{-i\boldsymbol{k}\cdot\boldsymbol{R}_i} a_{\sigma}(\boldsymbol{k}), \tag{1.4}$$

which diagonalize the Hamiltonian, of which the secular equation gives the eigen-energy[125]:

$$E_{\pm}(\boldsymbol{k}) = \pm t \sqrt{3 + 2\cos(\sqrt{3}k_y a) + 4\cos\left(\frac{\sqrt{3}}{2}k_y a\right)\cos\left(\frac{3}{2}k_x a\right)}. \tag{1.5}$$

The band structure given by this dispersion is plotted in Figure 1.2. One of the most striking features of this band structure is that at the corners of the first Brillouin zone, namely $\boldsymbol{K}$ and $\boldsymbol{K'}$ given by (1.2), the band is gapless: $E(\boldsymbol{K}) = E(\boldsymbol{K'}) = 0$.

Note that in graphene, each carbon atom provides four valence electrons. Three of these electrons form the in-plane $\sigma$-bonding with neighboring carbon atoms through $sp^2$ hybridization, and shell-completing bonding results in a deep valence band due to the Pauli principle. The remaining electron occupies the out-of-plane $p_z$ orbital which can covalently bond to neighboring $p_z$ orbitals and form the $\pi$-band given in eqn.(1.5). As each unit cell contains two atoms, the $\pi$-band is half-filled: $E_F = 0$.

The fact that $E_F = 0$ at gapless K or K′ points has profound implications for graphene physics. In a typical transport experiment, graphene's chemical potential can reach as high as ~300 meV by gating, which corresponds to a gate voltage of $V_{bg}$ ~ 100 volts on an $SiO_2$ substrate. This value is much smaller than that of the hopping energy $t$~2.8 eV, which is the energy scale at which the dispersion singularity, referred to as the Van Hove singularity, occurs (red dashed circle in Fig. 1.2). Therefore the K and K′ points are the most accessible domains from an experimental point of view. The regions around these points are usually called K- or K′-valley.

### 1.2.2 *Linear dispersion and massless Dirac fermions*

Let us focus on the energy dispersion around the K (K′) valley where the upper and lower $\pi-$bands meet. The wave vector can be written as[125, 27]

$$\boldsymbol{k} = \boldsymbol{K} + \boldsymbol{q}, \quad |\,\boldsymbol{q}\,| \ll |\,\boldsymbol{K}\,| \;. \tag{1.6}$$

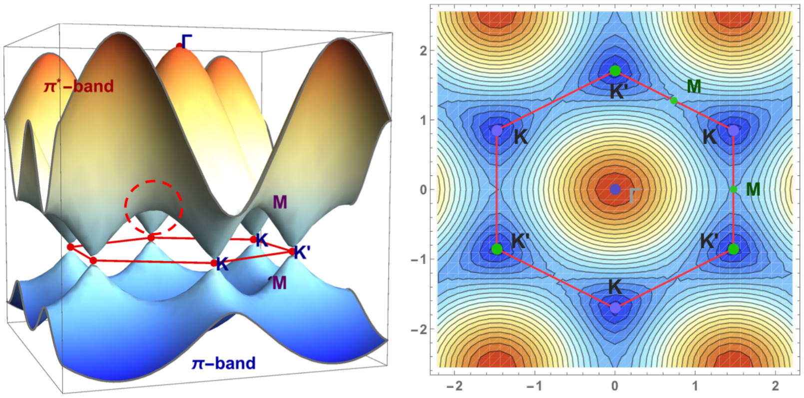

(a) The $\pi$- bands of graphene calculated with the tight-binding approach.

(b) First Brillouin zone of graphene.

Figure 1.2: The band structure of a monolayer graphene plotted for the first Brillouin zone.

In addition, the field operator in eqn. (1.4) can be decomposed into two parts, for each of which the Fourier component expands around the K and K′ point respectively as:

$$\begin{aligned} a_n &\sim e^{-i\boldsymbol{K}\cdot\boldsymbol{R}_n} a_{1,n} + e^{-i} e^{-i\boldsymbol{K}'\cdot\boldsymbol{R}_n} a_{2,n} \\ b_n &\sim e^{-i\boldsymbol{K}\cdot\boldsymbol{R}_n} b_{1,n} + e^{-i} e^{-i\boldsymbol{K}'\cdot\boldsymbol{R}_n} b_{2,n} \end{aligned} , \tag{1.7}$$

where $a_{1,n} = a_{1(2),n}(\boldsymbol{q})$ is the sublattice A field operator expanded around the K(K′) point. With $\mid \boldsymbol{q} \mid \ll \mid \boldsymbol{K} \mid$, one expects these new field operators to be slow-varying within the Brillouin zone. Note that we have integrated the spin index $\sigma$ into the new index $n$ for brevity. With this representation for the tight-binding Hamiltonian, it can be shown[125, 27] that the Hamiltonian around the K-point can be written as

$$H_{\pm} = v_F \begin{vmatrix} 0 & p_x \pm i p_y \\ p_x \mp i p_y & 0 \end{vmatrix}, \tag{1.8}$$

with $v_F = \frac{3ta}{2\hbar}$, and $H_{+}(H_{-})$ denotes the Hamiltonian around K (K′) valley.

The Hamiltonian can be written in a more concise form as

$$H_K = v_f \boldsymbol{\sigma} \cdot \hbar \boldsymbol{q} \tag{1.9}$$

, where $\boldsymbol{\sigma} = (\sigma_x, \sigma_y)$ is the Pauli matrix. Thus in graphene, the energy dispersion relation of the electron around K is linear in momentum, i.e., $E(q) = v_F \, |\boldsymbol{q}|$. Further, by virtue of $v_g \equiv \partial E / \hbar \partial k$, we can identify $v_F \sim 1 \times 10^6 m/sec$ as the electron group velocity which is irrespective of the energy. This linear dispersion is remarkable for distinguishing the electron in graphene from its counterparts in the other 2-DEGS, which typically exhibit a quadratic dispersion relation. The Dirac-like

Hamiltonian (1.9) and the linear dispersion relation suggests that electrons around the K (K′) point with low excitation energy behave like relativistic particles without rest mass. The charge carriers are, therefore, referred to as massless Dirac fermions, and the K's points as the Dirac points accordingly.

The eigen function of the Hamiltonian (1.9) in real space is written as a two component spinor

$$\Psi_{\boldsymbol{K}}(\boldsymbol{r}) = \begin{pmatrix} \Psi_A \\ \Psi_B \end{pmatrix}, \tag{1.10}$$

of which the amplitude $\Psi_A e^{i\boldsymbol{K}\cdot\boldsymbol{r}}$ and the amplitude $\Psi_B e^{i\boldsymbol{K}\cdot\boldsymbol{r}}$ gives the wave function on the $A$ and $B$ sublattices respectively. It appears that the Hamiltonian couples two wavefunctions to each other but not to themselves, which is compatible with the tight-binding assumption. In the momentum space, the wave function around K takes the form

$$\psi_{\pm,\boldsymbol{K}}(\boldsymbol{k}) = \frac{1}{\sqrt{2}} \begin{pmatrix} e^{-i\theta_k/2} \\ \pm e^{i\theta_k/2} \end{pmatrix}, \tag{1.11}$$

where $\theta_k \equiv arctan(\frac{k_x}{k_y})$. Plus(+) and minus(-) signs denote the positive and negative eigen-energies, corresponding to the $\pi$ and $\pi^*$ bands respectively.

Similarly, the Hamiltonian in the K′-valley takes the same form as eqn. (1.9) except that the Pauli matrix $\boldsymbol{\sigma}$ is replaced by $\boldsymbol{\sigma}^*$=($\sigma_x, \sigma_y$), with the corresponding wave function:

$$\psi_{\pm,\boldsymbol{K'}}(\boldsymbol{k}) = \frac{1}{\sqrt{2}} \begin{pmatrix} e^{i\theta_k/2} \\ \pm e^{-i\theta_k/2} \end{pmatrix}, \tag{1.12}$$

which is the time-reversed state of $\psi_{\pm,\boldsymbol{K}}(\boldsymbol{k})$.

### 1.2.3 *Chirality of Dirac fermions in graphene*

The spinor representation of the wave function (eqn. (1.10)) indicates that the total wave function is s superposition of contributions from sublattices $A$ and $B$ , and the weighting of each component is given by its orientation in the spinor space. We emphasize that although we use the formalism developed for the real spin degree of freedom, the associated spinor operator $\boldsymbol{\sigma}$ acts only on the sublattice space, or the pseudospin degree of freedom as it is usually called in the graphene literature, and is independent of the real spin of an electron.

It is useful to define a new quantum mechanical operator called the helicity operator (in the K-valley) as

$$\hat{h} = \frac{1}{2}\boldsymbol{\sigma} \cdot \frac{\boldsymbol{p}}{|\boldsymbol{p}|}, \tag{1.13}$$

where $\boldsymbol{p} \equiv \frac{\hbar}{i}\boldsymbol{\nabla}$ is the momentum operator as in eqn. (1.8). The helicity operator projects the momentum of a given state onto the axes in the pseudospin space. From the low-energy Hamiltonian spanned around K point (eqn. (1.9), it is evident that $\Psi_K(\boldsymbol{r})$ is also an eigenstate of $\hat{h}$ such that

$$\hat{h}\Psi_K(\boldsymbol{r}) = \pm\frac{1}{2}\Psi_K(\boldsymbol{r}). \tag{1.14}$$

This relationship implies that in graphene, the charge carrier around the Dirac point has a definite helicity, also called chirality, associated with its momentum. We refer to an electron(hole) with this property as chiral because its directions of motion and its pseudospin are "locked" together. In the simplest terms, how the wave function is made from the wave functions of lattices $A$ and $B$ determines the direction in which the electron(hole) moves. We will see in the next section that chirality has a profound influence on the electronic transport properties in graphene.

Finally, it should be noted that in the K'-valley, the chirality of the carriers is flipped relative to their counterparts in the K-valley, as the states of carriers and their counterparts are time-reversed to each other. The helicity operator in the K'-valley, $\hat{h}^* = \frac{1}{2}\boldsymbol{\sigma}^* \cdot \frac{\boldsymbol{p}}{|\boldsymbol{p}|}$ , is left-handed.

## 1.3 TRANSPORT PROPERTIES OF DIRAC FERMIONS IN GRAPHENE

In this thesis, we use graphene, a highly tunable 2-dimensional semimetal, as a basis for studying mesoscopic superconductivity. The discussion in this section ,therefore, focuses on the concepts in graphene transport that are most relevant to our experiments.

### 1.3.1 *A highly tunable 2-DEGS*

One of the most appealing features of graphene, from the experimental point of view, is the tunability via field effect, meaning that the charge carrier density in graphene can be tuned easily by applying a gate voltage.

In a typical graphene transport measurement setup, a graphene flake is deposited on an insulating $SiO_2$ surface (thickness~ 300 nm, relative permittivity $\varepsilon$~3.9) on top of a highly-doped silicon wafer, referred to as the backgate. Applying voltage $V_{BG}$ to the backgate will charge the graphene as one of the metallic sheets in a parallelplates capacitor. As the energy band is half-filled ($E_F = 0$) for neutral graphene, applying positive $V_{BG}$ will draw an excess of electrons into the graphene, making it an *n-doped* semi-metal, with a positive chemical potential $\mu$. Similarly, applying $V_{BG} < 0$ will dope the graphene into a *p-type* semi-metal with $\mu < 0$. The transition between *n-type* and *p-type* graphene through gating is continuous as graphene is gapless in a low energy regime. The backgate voltage at which the two $\pi$-bands meet is called the charge neutrality point $V_{CNP}$ or the Dirac point in the graphene literature.

The carrier density $n$ and the Fermi energy $E_F$ can be easily calculated with the parallel-plate capacitor model (regardless of quantum capacitance, given by the finite chemical potential, which is subtle in our experiments )

$$n = \frac{\varepsilon_0 \varepsilon V_{BG}}{de}, \tag{1.15}$$

or

$$n(\#/cm^2) = \frac{5.53 \times 10^{12} \varepsilon V_g(volts)}{d(nm)}, \tag{1.16}$$

where d is the thickness of the gate dielectric and $\varepsilon$ is the relative permittivity. The Fermi wave vector $k_F$ and the Fermi energy $E_F$ can be obtained (by quantization in x- and y-axis of the graphene plane) as

$$k_F = \sqrt{n\pi}, \tag{1.17}$$

$$E_F = \hbar v_F k_F = \hbar v_F \sqrt{n\pi}, \tag{1.18}$$

where $v_F \sim 1 \times 10^6 m/sec$.

### 1.3.2 *Klein paradox and chiral tunneling in graphene*

In classical mechanics, a potential barrier $V_0$ can confine a particle with lower energy $E$ ($V_0$>$E$). In quantum mechanics, a non-relativistic particle described by the Schrödinger equation has a finite probability of tunneling into the barrier as an evanescent wave. If the barrier has finite thickness $D$, the particle has a finite chance of transmitting with a probability that decays exponentially with $|V_0|$ and $D$.

A surprising situation happens if this quantum object is described by the linear Dirac equation (with a form similar to eqn.(1.9)), which allows positive- or negative-energy eigenstates. The potential barrier appears to be attractive to a particle in the negative eigenstate, and becomes more so if the barrier height $|V_0|$ increases. This phenomenon is called the Klein paradox, and the associated highly-transmissive tunneling is called Klein tunneling, as first proposed by Oskar Klein in 1929[80].

With it's negative energy eigenstate, this Dirac particle can enter the barrier and has a high probability to tunnel through it. For Dirac fermions in graphene with a sharp potential profile (Fig. 1.3, upper

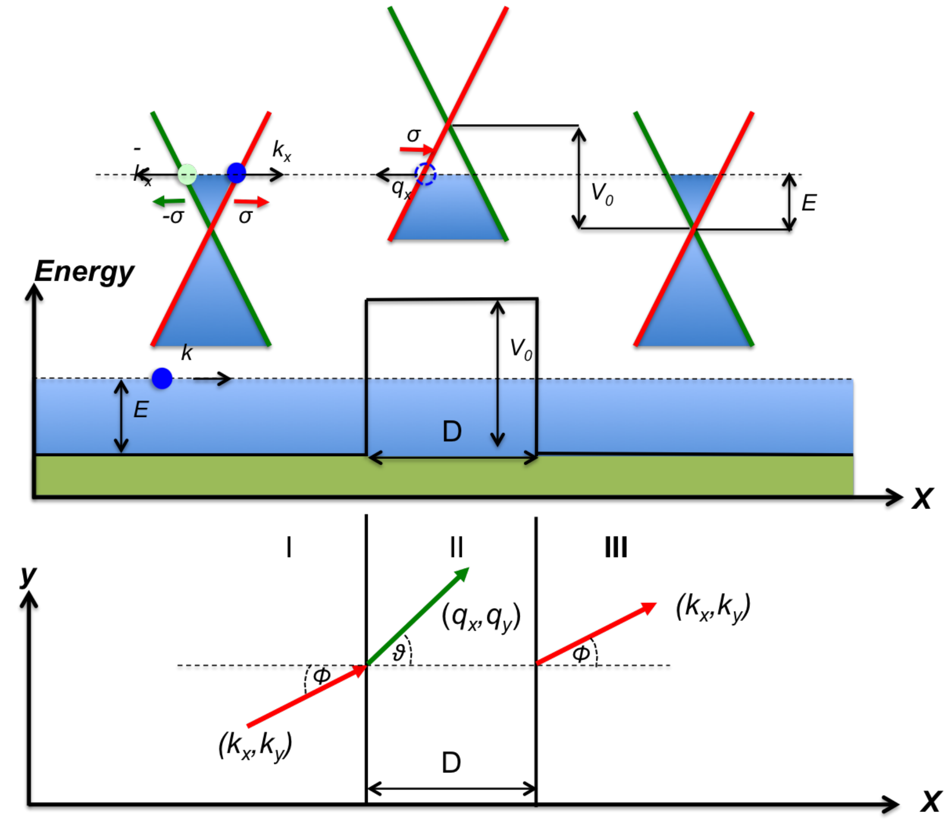

Figure 1.3: Klein tunneling of a Dirac Fermion in graphene.

panel), the transmission probability of this process can be obtained by matching wave functions at the boundaries, as expressed by[77, 27]

$$T(\phi) = \frac{\cos^2\theta\cos^2\phi}{[\cos(Dq_x)\cos\phi\cos\theta]^2 + \sin^2(Dq_x)(1 - ss'\sin\phi\sin\theta)^2}, \tag{1.19}$$

where $s = sgn(E)$, $s' = sgn(E - V_0)$, $\boldsymbol{q}$ is the wave vector in the potential region, and the angles are taken with respect to the normal as defined in Figure 1.3.

We can see immediately that for $\phi = 0$, or for $Dq_x = n\pi$ where n is an integer, the transmission is unity regardless of the barrier's height and depth ($|V_0|$ and $D$). This is very different from the situation with non-relativistic particles, in which the transmission probability is always less than one, and decreases exponentially as the strength of confinement increases. When $|E| \ll |V_0|$, $T(\phi)$ takes the asymptotic form

$$T(\phi) \sim \frac{\cos^2\phi}{1 - \cos^2(Dq_x)\sin^2\phi}, \tag{1.20}$$

which exhibits an oscillatory transmission rate as a function of the incident angle $\phi$(Fig. 1.4).

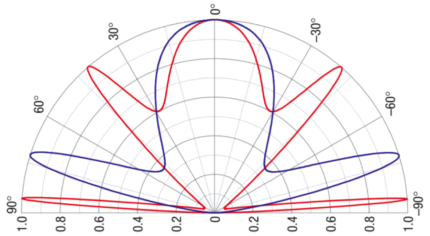

Figure 1.4: The angular dependence of transmission probability of chiral tunneling in monolayer graphene. The image is adapted from ref. [77]

### 1.3.2.1 *Chirality and perfect transmission*

Note that although Klein tunneling is a general property shared by Dirac particles, perfect transmission at normal incidence ($T(\phi = 0) = 1$), independent of the barrier height $|V_0|$ , is guaranteed only by the chirality in graphene. As discussed in subsection 1.2.3, the pseudospin degree of freedom $\sigma$ represents the relative contributions of sublattices $A$ and $B$ to the total wave function. The pseudospin is very robust, and thus a good quantum number of the system, since the pseudospin-flipping process would require scattering with a short-distance potential that acts differently on sublattice $A$ and $B$. This is important to note, as scattering of this nature is very difficult to achieve in practice.

Consider a 1-dimensional case as illustrated in Figure 1.3.When impinging on a potential barrier, the right-moving electron from region I with pseudospin $\sigma$ (($-k_x$,-$\sigma$), red branch), can scatter into two possible states: the left-moving electron (($-k_x$,-$\sigma$) , green branch), or the left-moving hole (($q_x, \sigma$), red branch). Given that back-scattering as an electron requires pseudospin flipping, an incoming electron is more likely to scatter into the hole state with the same pseudospin. The negative charge of the electron is therefore transferred to region III with 100% probability. This argument is based entirely on the conservation of pseudospin and the chirality of the Dirac fermion in graphene with no reference to details pertaining to any potential barriers such as $|V_0|$ and D. For a non-chiral system, the transmission of Klein tunneling becomes perfect as $|V_0| \to \infty$[36].

### 1.3.2.2 *Creating barrier in graphene*

The potential barrier as previously discussed of Klein tunneling can be created in graphene by the field effect. As discussed in subsection 1.3.1, graphene can be charged into an n-type semi-metal by applying a positive gate voltage or into a p-type semi-metal by applying a negative gate voltage. A combination of global and local gating in a graphene transistor can tune the graphene into an n- or p-type locally, resulting in a spatial variation of potentials. The *P*-*N* junctions

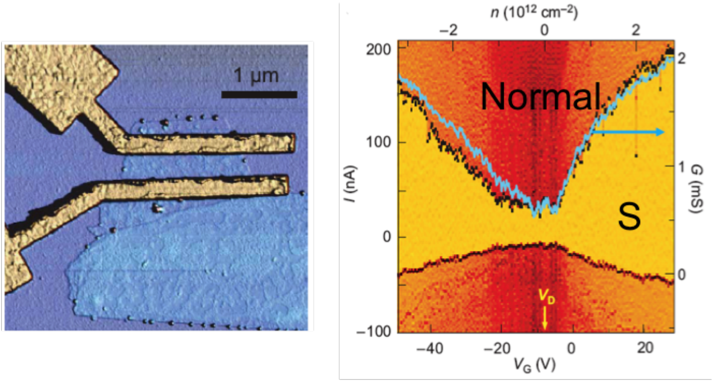

Figure 1.5: Image adapted from Ref. [70]. Bipolar Josephson effect in graphene.

thus created are equivalent to potential barriers and allow us to study chiral Klein tunneling in a solid state system.

## 1.4 SUPERCONDUCTIVITY CARRIED BY DIRAC FERMIONS

It has been found that when two superconducting electrodes are placed close enough to each other on graphene, a finite supercurrent can flow across the graphene sheet at a temperature well below the $T_c$ of superconductor[70]. The transport measurement at at low temperature shows that the supercurrent in the graphene is bi-polar, which means that the supercurrent can be carried by electron-like or hole-like excitations in graphene. The supercurrent is non-zero at the charge neutrality point where the Fermi energy is essentially zero (However there are always chemical potential fluctuations due to electron and hole puddles in the graphene flake[89], which is more pronounced in devices built on $SiO_2$ substrate). The transfer of supercurrent across the non-superconducting graphene is carried out by both $K$ and $K'$ valleys, due to the time-reversal nature of the Cooper pair constituents.

The fact that graphene is capable of carrying supercurrent, discovered less than three years after the realization of the material itself, stimulated the field immediately, as it suggests that graphene may be a great platform, for reasons explained next, for studying the physics of superconductivity at the mesoscopic scale.

Beenakker et al.([13, 121, 15, 14]) pointed out that with its gapless band structure and linear dispersion relation associated with the Dirac fermion, graphene provides opportunities to study superconductivity carried by relativistic particles. This, in a sense, brings together two of the greatest achievements in physics of the last century, which are typically explored at different energy scales. Some fascinating phenomena based on the gapless band structure and chiral nature of graphene have been predicted, including the specular An-

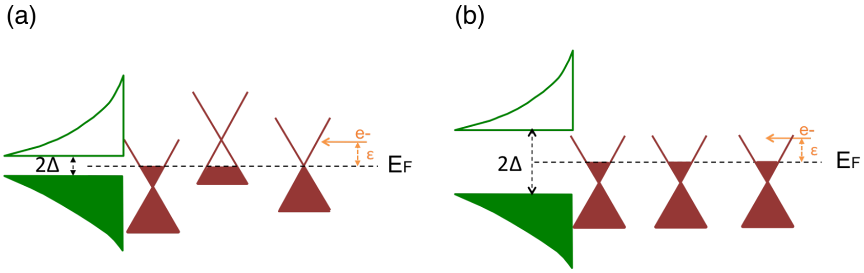

Figure 1.6: (a) Illustration of a disordered graphene in contact with superconductor with a relatively small gap. (b) Using a superconductor with a larger gap to contact graphene with lower disorder.

dreev reflection[13], the pseudo-diffusive Josephson effect[121], and topological superconductivity[108]. Thanks to the advances in the fabrication of high-quality (low-disorder) graphene devices with highly transparent contact to superconductors, the experimental realization of some of these predictions have been reported[92, 49, 24, 113, 4].

On the other hand, as a tunable, purely 2-dimensional metallic system whose charge carrier is highly accessible on the surface, graphene also hods great promise in regard to the study of some of the more traditional topics relating to superconductivity, including the superconducting proximity effect[16, 52, 47], the superconducting-insulating phase transition[78, 3], the (retro)Andreev reflection in a magnetic field[103], and the dynamics of supercurrent-carrying Andreev bounds states (discussed in Chapter 2) in both short- and long-junction limits.

## 1.5 MOTIVATION OF THIS THESIS

Our research explores the interplay between graphene physics and superconductivity in both realms as discussed above: the superconductivity carried by Dirac fermions, and topics relating to induced superconductivity in normal metals. In order to achieve this goal and experimentally investigate the associated physics to the greatest extent possible, two ingredients must be acquired:

1. Transparent contact between graphene and the superconductor, preferably with a large superconducting gap and a large critical magnetic field ($H_c$)

2. A high-quality (low-disorder) graphene device in which electrons travel ballistically.

These are essential to accessing the physics within or around the energy scale of the superconducting gap. As illustrated in Figure 1.6, if both requirements are met, the energy excitation always remains inside the gap.

In addition, a combination of high $H_c$ superconductors and high-quality graphene samples provides a basis for the study of 2-DEGS in the quantum Hall regime while the Andreev reflection (discussed in Chapter 2) at the graphene/superconductor interface remains appreciable.

The first experiment in this thesis (Chapter 3), the fabrication and measurement of NbN-grapehen-NbN Josephson junctions addresses the first ingredient listed above, as NbN's superconducting gap is about ten times larger than the widely used aluminum, and NbN's critical magnetic filed ($H_{c2}$) is much larger than the typical onset B-field of integer quantum Hall effect in graphene on $SiO_2$ substrate. The experiment discussed in Chapter 4 focuses on the fabrication and characterization of high quality graphene Josephson junctions of which the 2-DEGS is encapsulated in hexagonal boron nitride, an ultra-clean, ultra-flat 2-dimensional crystal that proved critical to all our device fabrication from that point on.

All the fabrication techniques and experiment described in the present study culminate in a final experiment, which was still in progress at the time of this writing. We will demonstrate how this experiment has allowed us to study some fundamental phenomena in mesoscopic superconductivity, manifested in the highly tunable 2-dimensional system provided by graphene, which has the potential to significantly improve understanding of this subject in the field in the near future.

# 2

# SUPERCONDUCTIVITY AND PROXIMITY EFFECT

Discovered in 1911, superconductivity is a profound and important field in solid state physics and continues to draw considerable interest because of the richness of its fundamental science and its potential in applications. This chapter presents the basic theoretical background in this field, with an emphasis on traditional BCS superconductivity at the mesoscopic scale, which is the most relevant scale to the present study. We will discuss basic postulates pertaining to superconductivity in a bulk superconductor, and show how these lead to an understanding of the macroscopic coherent phenomena observed in superconductors.

In the subsequent sections, we move on to inhomogeneous systems and demonstrate how normal metals can acquire superconducting-like properties and support supercurrent transport. The gauge-invariant phase difference, which is a signature property of superconductivity, and its relationship to the flow of supercurrent through (non-superconducting) weak links will be discussed and calculated for the type of device measured in our experiments.

The Andreev reflection and Andreev bound states constitute the underlying microscopic mechanisms of the superconducting proximity effect. We will discuss theses in terms of both short- and long-junction limits to determine how the presence of impurity can affect the dynamics of the hybrid system composed of a superconductor and normal metals.

## 2.1 MACROSCOPIC SUPERCURRENT IN SUPERCONDUCTOR

### 2.1.1 *Superconductivity: A different phase of matter*

Take a piece of lead (Pb), electrically link it to the measurement rack, submerge the lead in liquid helium, measure the resistance across the lead itself, and you see nothing. The disappeared electrical resistance, with accompanying phenomena such as diamagnetism below a certain magnetic field and the anomaly of specific heat, means that the metal is in a specific state called the superconducting phase. The current induced in a Pb ring kept in this phase can persist for more than a year without any external powering.

A metal capable of undergoing this type of phase transition is called a superconductor [1]. This type of material was discovered in 1911 by

---

[1] Here we focus on the classical superconductivity in metals or alloys. In particular, we use only the *s-wave* superconductor in our experiments.

H. Kamerlingh Onnes, three years after he had succeeded in liquifying helium gas, which enabled him to cool down mercury, in which the superconductivity was measured for the first time in history. In fact, a large number of metals have been found to be superconductors, with an individual transition temperature $T_C$ at which the metal turns to this phase. In the 1960's , Bardeen, Cooper and Schrieffer proposed a complete and highly satisfactory theoretical picture, which soon became the dominant theory used to explain most of the superconducting phenomenology found in classical superconductors. This microscopic theory, referred to as BCS theory, after Bardeen, Cooper and Schrieffer is built in reference to three crucial insights[11, 120, 39]:

1. The force between electrons can sometimes be attractive rather than repulsive. This electron-electron attraction is the result of the coupling between the electrons and phonos mediated by the underlying lattice of the superconductor.

2. The Cooper problem: In the presence of attractive potential, the ground state of the free electron gas that corresponds to the complete filling of the single-particle energy level up to the Fermi energy becomes unstable, regardless of how weak the attraction might be! Therefore there exists a two-electron bound state of energy $E < 0$.

3. A macroscopic (many-body) wave function in which each electron near the Fermi surface is paired with its individual spin and momentum counterpart (spin ↑and spin↓, $\overrightarrow{k}$ and $-\overrightarrow{k}$ ) was constructed. The BCS energy gap $2\Delta$ arises from this pairing, as it corresponds to the energy cost to break up the Cooper pair.

Soon after it was published, the BCS theory was recognized as correct in many essential aspects. Further, the BCS energy gap was discovered experimentally almost at the same time as the theory was published. Among these following experiments, electron tunneling spectroscopy is arguably the most important. The reason the tunneling experiment is considered so important is because it not only showed the existence of the $2\Delta$ energy gap, but also showed the phonon structure in the spectra which gives rise to the electron-phonon coupling induced pairing[58].

### 2.1.2 *Macroscopic wave function of supercurrent carriers in a superconductor*

The macroscopic behavior of supercurrent-carrying particles in superconductors was anticipated before BCS theory. The assumption is the existence of a macroscopic (many-body) wavefunction $\psi(\boldsymbol{r}, t) = \psi_0(\boldsymbol{r}, t)e^{i\theta(\boldsymbol{r},t)}$ that describes the behaviors of a collection of non-interacting electrons. In turn. this collection gives rise to superconducting properties such as dissipationless electric current, diamagnetism (Meissner effect), and the macroscopic coherence transport of supercurrent across non-superconducting materials (Josephson effect), as we will discuss following sections.

The wave function, which was treated as an order parameter in 2nd order phase transition by Ginzburg and Landau, obeys a Schrödinger-like equation for the ensemble of supercurrent in the electromagnetic field:

$$\alpha\psi + \beta \mid \psi \mid^2 \psi + \frac{1}{2m^*}\left(\frac{\hbar}{i}\boldsymbol{\nabla} - q^*\boldsymbol{A}(\boldsymbol{r},t)\right)^2 \psi = 0. \tag{2.1}$$

where $\boldsymbol{A}(\boldsymbol{r},t)$ is a vector potential associated with the electromagnetic field, and $m^*$and $q^*$ are the mass and charge of the "superelectrons" respectively. This is the celebrated *Ginzburg-Landu* equation for the superconducting order parameter $\psi$. It turns out that for BCS superconductors (traditional metallic superconductors), $m^* = 2m_e$ and $e^* = 2e$ as the supercurrent is carried by Cooper pairs. However the G-L equation makes no reference to the microscopic nature, which may differ for different types of superconductors. On the other hand, as it is independent of the pairing mechanism, the G-L formalism describes the superelectrons (often referred to as a charged-superfluid) as a quantum mechanical entity, from which many physical insights into the coherent phenomenology can be gained.

Before making a further analogy with the single-particle Schrödinger equation, we should first clarify the interpretation of the macroscopic wave function $\psi(\boldsymbol{r},t)$. In the single-particle Schrödinger equation, $\psi(\boldsymbol{r},t)$ is interpreted as the probability amplitude that gives the probability of finding a particle at a given location $\boldsymbol{r}$ at time $t$ as $\mid \psi(\boldsymbol{r},t) \mid^2$. Further, the normalization condition $\int \psi^*\psi dV$=1 implies that the probability of finding this particle somewhere in the whole space is unity at any time. For the macroscopic wave function associated with superelectrons, we require the following normalization condition to be satisfied:

$$\int \psi^*(\boldsymbol{r},t)\psi(\boldsymbol{r},t)dV = N_s^* \tag{2.2}$$

$$\mid \psi(\boldsymbol{r},t) \mid^2 = \psi^*(\boldsymbol{r},t)\psi(\boldsymbol{r},t) = n_s^*(\boldsymbol{r},t). \tag{2.3}$$

As we assume that $\psi(\boldsymbol{r},t)$ is the macroscopic wave function of the superelectron ensemble, it follows that $N_s^*$ represents the total number of superelectrons (the Cooper pairs in the BCS superconductors) in the entire superconductor, and that $n_s^*$ represents the local density of superelectrons at location $\boldsymbol{r}$ at a given time $t$. Accordingly, the wave function $\psi(\boldsymbol{r},t)$ takes the form

$$\psi(\boldsymbol{r},t) = \sqrt{n_s^*(\boldsymbol{r},t)}e^{i\theta(r,t)} \tag{2.4}$$

where $\theta$ is a real function that represents the phase of a complex number.

### 2.1.3 *Supercurrent density and gauge invariant phase gradient*

Based on the identity given in eqn.(2.2), eqn.(2.3) and eqn.(2.4), we can obtain the supercurrent density $\boldsymbol{J}_s$ by multiplying the superelectron charge $q^*$ with the particle flow density analogous to the probability current, which is standard in single-particle quantum mechanics. Hence,

$$\boldsymbol{J}_s = \frac{q^*}{2m^* i}(\psi^* \boldsymbol{\nabla} \psi - \psi \boldsymbol{\nabla} \psi^*) - \frac{q^*}{2m^*}\psi\psi^* \boldsymbol{A}. \tag{2.5}$$

Substituting eqn.(2.4) into eqn.(2.5) yields:

$$\boldsymbol{J}_s = q^* n_s^*(\boldsymbol{r}, t)\left(\frac{\hbar}{m^*}\boldsymbol{\nabla}\theta(\boldsymbol{r}, t) - \frac{q^*}{m^*}\boldsymbol{A}(\boldsymbol{r}, t)\right). \tag{2.6}$$

The term $\left(\frac{\hbar}{m^*}\boldsymbol{\nabla}\theta(\boldsymbol{r}, t) - \frac{q^*}{m^*}\boldsymbol{A}(\boldsymbol{r}, t)\right)$ is defined as the velocity of superelectrons $\boldsymbol{v}_s$ if the supercurrent density is written as $\boldsymbol{J}_s = q^* n_s^* \boldsymbol{v}_s$.

#### 2.1.3.1 *Gauge invariance and the current phase relation*

Note that variables such as $\boldsymbol{A}, \theta$ or $\phi$ are not physical observables. Therefore, certain kinds of formal transformations of these quantities can be found without changing the associated observables like $\boldsymbol{B}$,$\boldsymbol{E}$ or $\boldsymbol{J}_s$. By introducing a *gauge-invariant phase gradient*

$$\gamma = \boldsymbol{\nabla}\theta - \frac{q^*}{\hbar}\boldsymbol{A}, \tag{2.7}$$

and by substituting it into the expression of $\boldsymbol{J}_s$ in eqn.(2.6), we obatin the supercurrent given by

$$\boldsymbol{J}_s = \frac{q^* n_s^* \hbar}{m^*}\gamma. \tag{2.8}$$

We arrive at an essential relation in superconductivity which tells us that the supercurrent density $\boldsymbol{J}_s$ in a superconductor is proportional to the *gauge-invariant phase gradient* $\gamma$. This relation suggests that when a phase gradient is created in the superconductor, supercurrent will flow accordingly.

Finally, by identifying $q^* = (-2e)$ in a BCS superconductor, we can write

$$\gamma = \boldsymbol{\nabla}\theta - \frac{2\pi}{\Phi_0}\boldsymbol{A}, \tag{2.9}$$

where

$$\Phi_0 = \frac{h}{2e} \tag{2.10}$$

is the magnetic flux quantum.

## 2.2 JOSEPHSON EFFECT

In 1962, Brian D. Josephson predicted[75] that if two superconductors are separated from each other by a thin insulating layer (a tunneling barrier), finite supercurrent can flow . With established experimental evidence[8], this phenomenon, the Josephson effect, soon became a hallmark of superconductivity as it manifests macroscopically the coherent properties expected for charged superfluids. Although it was calculated for a superconductor-insulator-superconductor system (S-I-S junctions) in the original paper, the Josephson effect is principally a fundamental phenomenon that can be found in any system comprising two weakly-coupled superconductors. The weak link can be established in various configurations with numerous materials. Today, devices exhibiting the Josephson effect, known as the Josephson junction or the Josephson weak link, are widely used for many applications of superconductivity in sensors, high-frequency devices and quantum information. The Josephson effect also provides an effective platform for investigating fundamental physics such as macroscopic quantum coherent phenomena.

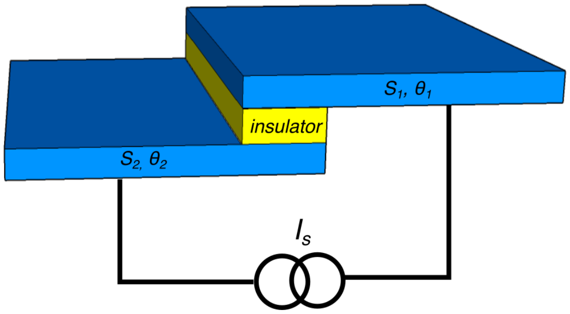

Figure 2.1: A Josephson tunnel junction.

In this thesis, we study Josephson weak links made with graphene in diffusive and ballistic regimes. The following section presents some basic concepts relating to the Josephson effect and to characteristics of Josephson junctions that will help us to understand our experimental results.

### 2.2.1 *Josephson equations*

Two Josephson equations describe the dynamics of supercurrent in an S-I-S junction:

$$J_s = J_c sin\varphi, \tag{2.11}$$

$$\frac{\partial\varphi}{\partial t} = \frac{2\pi}{\Phi_0}\int_1^2 \boldsymbol{E}(\boldsymbol{r},t)\cdot d\boldsymbol{l}. \tag{2.12}$$

where $J_c$ is the maximum supercurrent density, and $\varphi$ is the *gauge-invariant phase difference* between the two superconductors $S_1$ and $S_2$ (Fig. 2.1) given by

$$\begin{aligned}\varphi(\boldsymbol{r},t) = \quad & \textstyle\int_1^2 \gamma(\boldsymbol{r},t)\cdot d\boldsymbol{l} = \int_1^2 \left(\boldsymbol{\nabla}\theta - \frac{2\pi}{\Phi_0}\boldsymbol{A}\right)\cdot d\boldsymbol{l} \\ & = \theta_2(\boldsymbol{r},t) - \theta_1(\boldsymbol{r},t) - \textstyle\frac{2\pi}{\Phi_0}\int_1^2 \boldsymbol{A}(\boldsymbol{r},t)\cdot d\boldsymbol{l}\end{aligned}. \tag{2.13}$$

Here we simplify the discussion by focusing on a 1-D channel in which $J_s$ is the amplitude of the supercurrent density.

#### 2.2.1.1 *Current-phase relation in a Josephson junction*

Note that in the first Josephson equation (2.11), the gauge-invariant phase "difference" $\varphi$ between $S_1$ and $S_2$ has replaced the gauge-invariant phase gradient $\gamma$ in determining the supercurrent density $J_s$ (eqn. (2.8)). This substitution is made based on the assumption that the phase gradient $\gamma$ in the bulk superconductor is negligible compared to in the weak link, for the reasons described next.

Recall eqn. (2.8):

$$\boldsymbol{J}_s = \frac{q^* n_s^* \hbar}{m^*}\gamma.$$

Consider a homogeneous supercurrent density [2]: If we move along an electrical path from $S_1$ through the weak link to $S_2$ associated with a given $\boldsymbol{J}_s$, we would see that the phase gradient $\gamma$ in the superconducting leads is much smaller than that in the weak link part. This is because $\gamma$ is inverse proportional to the Cooper pair density $n_s^*$ ($\boldsymbol{J}_s$unchanged due to current conservation) . This assumption is true as long as the Cooper pair density in the bulk superconductor ($S_1$ and $S_2$) remains much larger than that in the weak link, which is clearly the case in the context of an *S-I-S* junction as discussed here. It also follows that the phase factors inside both leads vary slowly with space, and can be readily treated as homogeneous. The weak link is "weak" because it is much easier to twist the phase difference between its two ends than in a superconductor.

From eqn. (2.8), it is intuitive to assume that $J_s$ is proportional to the phase difference $\varphi$. However, the wave function $\psi_{1,2}$ in the leads

---

[2] This is a reasonable assumption for junctions with small areas, and it still holds for the local current density of large junctions.

must be single-valued with respect to the phase up to a multiple of $2\pi$, which should also result in a 2-$\pi$ periodicity in $J_s$:

$$J_s(\varphi) = J_s(\varphi + 2n\pi), \tag{2.14}$$

with the constraint that there is no supercurrent if the phase difference between the two leads is zero ($\theta_1 = \theta_2$):

$$J_s(\varphi = 0) = 0. \tag{2.15}$$

We conclude that the supercurrent density $J_s$ of a Josephson *S-I-S* junction changes sinusoidally with the phase difference between the two superconducting leads,

$$J_s = J_c sin(\varphi),$$

which gives us the *current-phase relation*.

### 2.2.1.2 *Voltage-phase relation in a Josephson junction*

We can also obtain a voltage-phase relation by drawing on the fact that in the 1-D case under discussion, $\int_1^2 \boldsymbol{E}(\boldsymbol{r}, t) \cdot d\boldsymbol{l}$ in eqn. (2.12) is simply the voltage drop $V$ across the junction. Hence, eqn. (2.12) can be written as

$$\frac{\partial\varphi}{\partial t} = \frac{2\pi}{\Phi_0} V, \tag{2.16}$$

and the time-dependent supercurrent density obtained is

$$J_s(t) = J_c sin(\varphi_0 + \frac{2\pi}{\Phi_0} V \cdot t). \tag{2.17}$$

We see that the Josephson junction can be driven as an oscillator by applying a voltage $V$ across the junction, with frequency $\nu_J$ (the Josephson frequency) given by $\frac{V}{\Phi_0}$, which in turn gives ~ 500 GHz/mV.

## 2.2.2 *Josephson effect in the presence of an external magnetic field*

We have seen in 2.2.1 the current-phase, and voltage-phase relations of a Josephson tunnel junction (S-I-S) manifested in the 1-dimensional limit. We now turn our attention to an extended 2-dimensional S-I-S junction in the presence of external magnetic field $\boldsymbol{B}$. We will see that applied voltage causes temporal oscillation of the gauge-invariant phase difference $\varphi$, and that the applied magnetic field induces a spatial variation of $\varphi$.

Consider the S-I-S junction geometry shown in Figure 2.2. Two superconducting leads are separated by an insulating layer with thickness $D$. An external magnetic field $\boldsymbol{B} = (0, 0, B_z)$ is applied perpendicularly to the x-y plane of the device. In order to illustrate the effect of external magnetic field, we can calculate the shift of the gauge-

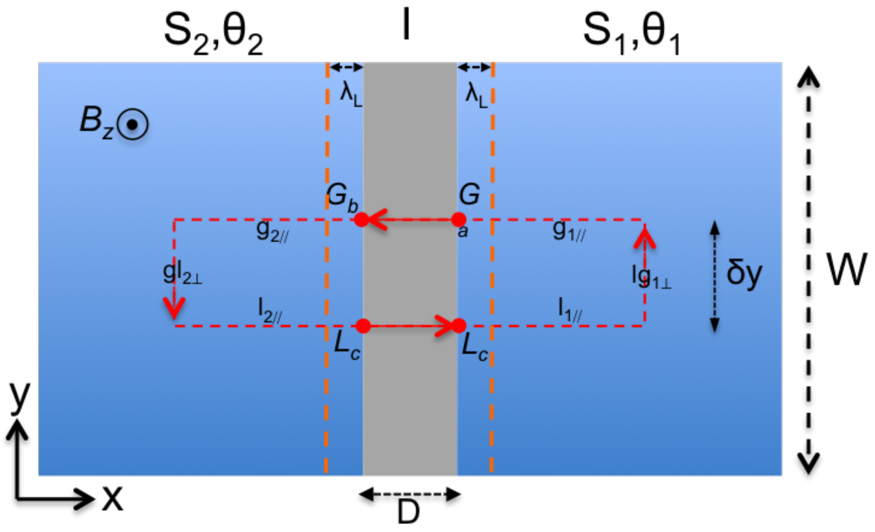

Figure 2.2: Schematic of 2-dimensional SIS junction.

invariant phase difference along y-axis from point $G$ to point $L$, which is the difference between $\varphi(L)$, and $\varphi(G)$. This can be achieved by taking a line integral of phase gradient $\boldsymbol{\nabla}\theta(x,y)$ along the contour depicted in red-arrow-lines. For a closed-loop contour, we require again the line integral to be single-valued up to a multiple of $2\pi$:

$$\begin{aligned} \oint_C \boldsymbol{\nabla}\theta\cdot d\boldsymbol{l} &= 0(modulo 2\pi) \\ = (\theta_{G_b}-\theta_{G_a}) + (\theta_{L_c}-\theta_{G_b}) &+ (\theta_{L_d}-\theta_{L_c}) + (\theta_{G_a}-\theta_{L_d}) \end{aligned} . \tag{2.18}$$

The first and third brackets represent the phase difference across a weak link at a single location. Therefore we can use the expression given in eqn. (2.13) directly to obtain

$$\theta_{G_b}-\theta_{G_a} = \varphi(G) + \frac{2\pi}{\Phi_0}\int_{G_a}^{G_b} \boldsymbol{A}\cdot d\boldsymbol{l} \tag{2.19}$$

$$\theta_{L_d}-\theta_{L_c} = -\varphi(L) + \frac{2\pi}{\Phi_0}\int_{L_c}^{L_d} \boldsymbol{A}\cdot d\boldsymbol{l} \tag{2.20}$$

The second and fourth brackets calculate the phase difference acquired along the contour inside the superconducting lead. To calculate these terms, we recall eqns. (2.8) and (2.9), and assign $\Lambda \equiv \frac{m^*}{n_s^* q^{*2}}$ (usually called the London coefficient) to obtain

$$\theta_{L_c}-\theta_{G_b} = \int_{G_b}^{L_c} \boldsymbol{\nabla}\theta\cdot d\boldsymbol{l} = \frac{2\pi}{\Phi_0}\int_{G_b}^{L_c} \Lambda\boldsymbol{J}_s\cdot d\boldsymbol{l} + \frac{2\pi}{\Phi_0}\int_{G_b}^{L_c} \boldsymbol{A}\cdot d\boldsymbol{l} \tag{2.21}$$

$$\theta_{G_a} - \theta_{L_d} = \int_{L_d}^{G_a} \boldsymbol{\nabla}\theta \cdot d\boldsymbol{l} = \frac{2\pi}{\Phi_0}\int_{L_d}^{G_a} \Lambda \boldsymbol{J}_s \cdot d\boldsymbol{l} + \frac{2\pi}{\Phi_0}\int_{L_d}^{G_a} \boldsymbol{A} \cdot d\boldsymbol{l} \tag{2.22}$$

By substituting these four equations into eqn. (2.18) , and rearranging for $\varphi(G) - \varphi(L)$, we obtain

$$\varphi(L) - \varphi(G) = \frac{2\pi}{\Phi_0}\oint_C \boldsymbol{A} \cdot d\boldsymbol{l} + \frac{2\pi}{\Phi_0}\int_{L_c}^{G_b} \Lambda \boldsymbol{J}_s \cdot d\boldsymbol{l} + \frac{2\pi}{\Phi_0}\int_{L_d}^{G_a} \Lambda \boldsymbol{J}_s \cdot d\boldsymbol{l} \tag{2.23}$$

$\boldsymbol{A}$ is the vector potential that gives rise to the magnetic field $\boldsymbol{B}$. Therefore by Stoke's theorem, the contour integral of $\boldsymbol{A}$ becomes $\oint_C \boldsymbol{B}\cdot d\boldsymbol{s}=\Phi$, the total magnetic flux in the contour-enclosed area.

The last two terms on the right hand side of eqn. (2.23) denote the line integrals of $\boldsymbol{J}_s$ along the inside of the superconductors (Fig. 2.2, dashed red lines). We argue that the line integrals vanish overall as follows. First, given the device geometry and the homogeneous current assumption, we can assume that $\boldsymbol{J}_s(x,y)=(J_x,0)$, so the part of the line integral taken along the y-axis ($gl_{2\perp}$, and $lg_{1\perp}$ ) is essentially zero. In addition, we note that the line integral along the x-axis ($g_{1,2/\!/}$and $l_{1,2/\!/}$ in the Fig. 2.2) also adds up to zero, as $G$ and $L$ are infinitesimally separated by $\delta y$ in the y-direction. Therefore the integrals of the neighboring path taken in opposite directions will cancel each other out. We can now conclude that

$$\varphi(L) - \varphi(G) = \frac{2\pi\Phi}{\Phi_0}. \tag{2.24}$$

The shift in the phase difference depends on the magnetic flux that penetrates the closed loop.

To calculate the flux $\Phi$, we first note that due to the Meissner effect, the magnetic field decays from the edge of a superconductor as

$$B(x) = B_{z0}exp(\frac{-(\mid x \mid -2/D)}{\lambda_L}) \tag{2.25}$$

,provided both that the insulating layer centers at x= 0, and $\lambda_L$ is the London penetration depth:

$$\lambda_L \equiv \sqrt{\frac{m^*}{\mu_0 n_s^* q^{*2}}}. \tag{2.26}$$

Thus the magnetic field is essentially zero beyond this length from the edge of the superconductor, and the area penetrated by the field is $2\lambda_L\delta y$. We can define an effective junction length $D' = D + 2\lambda_L$, such that the infinitesimal shift in phase difference equals $\frac{2\pi BD'\delta y}{\Phi_0}$.

Consequently, the phase difference across the junction as a function of the y-coordinate is

$$\varphi(y) = \frac{2\pi BD'y}{\Phi_0} + \varphi_0, \tag{2.27}$$

,where $\varphi_0 = \varphi(y = 0)$. By substituting (2.27) into (2.11), we obtain the spatial dependence of the supercurrent density as

$$J_s(y) = J_c sin\left(\frac{2\pi BD'y}{\Phi_0} + \varphi_0\right). \tag{2.28}$$

### 2.2.2.1 *Fraunhofer diffraction pattern of maximum supercurrent*

The total supercurrent $I_s(B_z)$ can be obtained by integrating $J_s(y)$ along the y-axis:

$$I_s(B_z) = \int_{-w/2}^{W/2} J_s(y)dy = \int_{-w/2}^{W/2} J_c sin\left(\frac{2\pi BD'y}{\Phi_0} + \varphi_0\right) dy. \tag{2.29}$$

Note that this is equivalent to the imaginary part of the integral

$$e^{i\varphi_0} \cdot \int_{-\infty}^{\infty} J_c(y) exp\left(i\left(\frac{2\pi BD'}{\Phi_0} y\right)\right) dy, \tag{2.30}$$

provided that $J_c(y) = J_c$ for $\mid y \mid \leq W/2$, and zero otherwise (no supercurrent outside the junction). The maximum supercurrent $I_c(B_z)$ of the junction is the magnitude of this complex integral:

$$I_c(B_z) = \left| \int_{-\infty}^{\infty} J_c(y) exp\left(i\left(\frac{2\pi BD'}{\Phi_0} y\right)\right) dy \right| \tag{2.31}$$

, and we see that the maximum supercurrent as a function of the external field is simply the *Fourier transform* of the supercurrent spatial distribution $J_c(y)$. Note that up to now, we have assumed a homogeneous current density along the y-direction. However, the result we obtained in eqn.(2.31) is more general, as the only constraint we imposed to establish equivalence is that the supercurrent disappears outside the junction (when $\mid y \mid > W/2$), irrespective of any detail inside (when $\mid y \mid \leq W/2$). For a spatially homogeneous current distribution $J_c(y)$, the integration of eqn.(2.31) yields

$$I_c(B_z) = I_c \left| \frac{sin(\frac{2\pi BD'}{\Phi_0}\frac{W}{2})}{\frac{2\pi BD'}{\Phi_0}\frac{W}{2}} \right| = I_c \left| \frac{sin(\frac{\pi\Phi}{\Phi_0})}{\frac{\pi\Phi}{\Phi_0}} \right|. \tag{2.32}$$

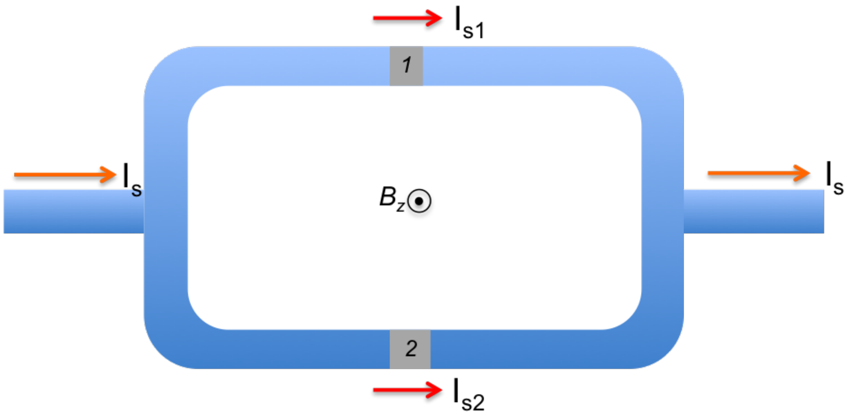

Figure 2.3: The schematic of a standard two-arm SQUID.

The flux $\Phi$ is the product of the external magnetic field B and the effective junction area with London penetration length $\lambda_L$ taken into account. This expression is identical to the well-known Fraunhofer diffraction pattern, which is the (spatial) intensity distribution of a coherent light after it has passed through a single slit.

### 2.2.3 *Phase drop across a weak link in a SQUID-like device*

The superconducting quantum interference device (SQUID) is a superconducting ring interrupted by two weak links (Fig. 2.3). In the presence of a perpendicular magnetic field $B_z$, two phase differences $\Delta\theta_1$ and $\Delta\theta_2$ across a weak link would result in a phase difference between the Josephson currents $I_{s1}$and $I_{s2}$ in two branches. The interference between $I_{s1}$ and $I_{s2}$ gives rise to the total supercurrent amplitude $\mid I_s(\Phi) \mid = \mid I_{s1} + I_{s2} \mid$ to oscillate with a periodicity equal to $\Phi_0$ . A SQUID typically encloses a much larger area than an extended Josephson junction does, as for the latter at least one dimension is limited by the coherence length $\xi$. For this reason,compared Josephson junction, SQUIDs are more sensitive to small changes in the $B$-field and are, therefore, widely used in magnetometry.

Here we do not derive the phase dynamics of a SQUID, which can be found in a rich body of literature on this subject[43, 120, 67]. Instead, let us consider a special case: a ring of superconductor interrupted by one weak link (Fig.2.4). Specifically, our goal is to deduce the phase drop across the weak link between two points $Q_a$ and $Q_b$, with the assumption that $J_s$ is homogeneous and $w' \ll W$.

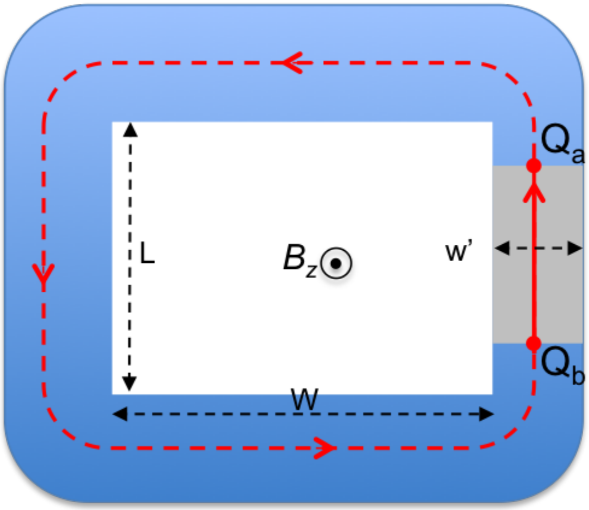

Figure 2.4: The schematic of a superconducting loop interrupted with a weak link.

Following the same reasoning as in eqn.(2.2.2), we can take a closed-loop as shown in Fig. 2.4, and calculate the line integral of $\nabla\theta$ along the contour

$$\oint_C \nabla\theta \cdot d\boldsymbol{l} = (\theta_{Q_a} - \theta_{Q_b})_{weaklink} + (\theta_{Q_b} - \theta_{Q_a})_{SC} = 0(modulo 2\pi), \tag{2.33}$$

where the first bracket denotes the gauge-invariant phase difference in the weak link (solid line), and the second bracket is calculated along a complementary path inside the superconductor (dashed line). Once again, we impose the single-value requirement for the phase acquired in a closed-loop.

The phase difference can be calculated from eqn. (2.13), which yields

$$(\theta_{Q_a} - \theta_{Q_b})_{weaklink} = \varphi(Q) + \frac{2\pi}{\Phi_0}\int_{Q_b}^{Q_a} A \cdot d\boldsymbol{l}. \tag{2.34}$$

whereas the second bracket can be written as

$$(\theta_{Q_b} - \theta_{Q_a})_{SC} = \int_{Q_a}^{Q_b} \nabla\theta \cdot d\boldsymbol{l} = \frac{2\pi}{\Phi_0}\int_{Q_a}^{Q_b} \Lambda \boldsymbol{J}_s \cdot d\boldsymbol{l} + \frac{2\pi}{\Phi_0}\int_{Q_a}^{Q_b} \boldsymbol{A} \cdot d\boldsymbol{l}, \tag{2.35}$$

according to eqn. (2.8) and (2.9). By adding up both equations above, imposing the single-value requirement, and rearranging for $\varphi(Q)$, we obtain

$$\varphi(Q) = -\frac{2\pi}{\Phi_0}\oint_C \boldsymbol{A} \cdot d\boldsymbol{l} - \frac{2\pi}{\Phi_0}\int_{Q_a}^{Q_b} \Lambda \boldsymbol{J}_s \cdot d\boldsymbol{l}. \tag{2.36}$$

Note that the device we are discussing typically consists of a piece of superconductor that is much thicker than its London penetration depth $\lambda_L$. In this situation, it is always possible to choose the path deep inside the superconductor, where $\boldsymbol{J}_s$ is zero. Based on this choice, we can omit the integral associated with $\boldsymbol{J}_s$. Finally, according to Stoke's theorem, $\oint_C \boldsymbol{A} \cdot d\boldsymbol{l} = \oint_C \boldsymbol{B} \cdot d\boldsymbol{s} = \Phi$, we have

$$\varphi(Q) = -\frac{2\pi\Phi}{\Phi_0} = -\frac{2\pi BLW}{\Phi_0}. \tag{2.37}$$

Therefore in a ring of superconductor interrupted by a weak link, *the phase change across the weak link is proportional to the magnetic flux that the ring encloses*. In Chapter 5, we will discuss how to study the dynamics of Andreev bound states (discussed in the next section) by performing tunneling spectroscopy in this kind of device.

Finally, it is important to note that although the derivation of the phase dynamics is established for the S-I-S junction, the main results should also hold for the SNS junction. Specifically, if $n_s$ in the normal region is much smaller than its counterpart in the superconducting leads, according to eqn.(2.8), the phase change across the weak link will dominate the total phase acquired in a loop.

## 2.3 ANDREEV REFLECTION AND THE SUPERCONDUCTING PROXIMITY EFFECT

When placed in good electrical contact with a superconductor, normal metal acquires some superconducting-like properties at a low temperature. This phenomenon is called the superconducting proximity effect (fig. 2.5). Known for 50 years, the proximity effect still attracts enormous interest owing to the richness of its physics.

The key mechanism responsible for the proximity effect, the Andreev reflection, offers phase correlations in a system without interacting electrons at mesoscopic scales; that is, the correlation is preserved at length scale that is larger than the Fermi wavelength or the mean free path of the system. The coupling between the electron and the hole excitation, when phase coherence is preserved, in either ballistic or diffusive normal metal is analogous to the clean and dirty limit of superconductors.

In this section, we employ a semi-classical picture to illustrate the processes of the Andreev reflection and the coherent transport of charge carrier across a junction normal, metallic junction (the *SNS* junction) .

### 2.3.1 *Andreev reflection*

A further confirmation of the existence of the Cooper pair and the BCS gap is provided by the discovery of the Andreev reflection. Let

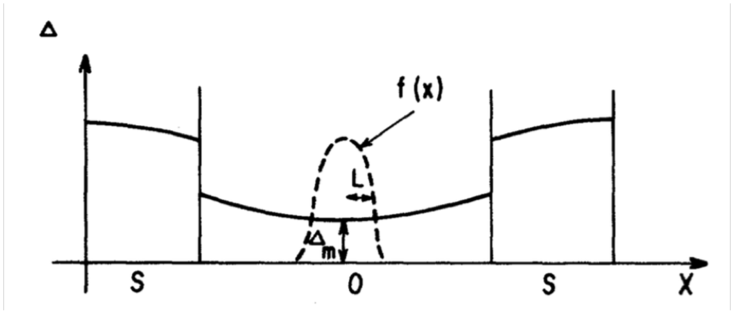

Figure 2.5: Image adapted from ref.[38]. Proximity effect in a SNS sandwich at $T \sim T_C$. Variation of order parameter ($\Delta(x)$) is plotted as a function of position. At the S/N interface, Δ decreases from its bulk value on the S side. In the normal region, Δ increases to its maximum when moving toward the interface, but sees a abrupt change across the interface. Also plotted in the middle is $f(x)$, the probability amplitude of finding two electrons in the condensed state at a given position x. $f(x)$ is reminiscent of the localized Andreev bound state as we know today.

us consider an interface between a normal metal and a superconductor, as shown in Figure 2.6. If an electron in a Bloch state is characterized by it's wave vector $k$ (assume a very low level of disorder in the crystal so that $k$ remains a good quantum number), energy $E_k$, and spin $\sigma$ moves toward the interface. Assume that the electron's energy is smaller than the superconducting gap of the superconductor,

$$E_k - E_F < \Delta$$

where $E_F$ is the Fermi energy of the normal metal. The electron can not propagate into the superconductor due to the lack of a single particle state in the gap. Therefore, the electron should be perfectly reflected at the interface. This is the normal reflection that one is familiar with. However, Andreev noticed that another type of reflection compatible with description given here: The incoming electron may grab an electron with a spin and momentum that is opposite to its own, thereby forming a Cooper pair that can propagate freely into the gap, and so join the condensate in the superconductor. In regard to conserving the momentum, spin , and charge, this process leaves behind an empty electronic state (hole) with the opposite spin $-\sigma$ and wave vector $-k$ [3]as shown in Fig. 2.6 by the dashed arrow. Known as the Andreev reflection, this is the only physical process responsible for charge transfer across the normal metal / superconductor (N/S) interface at energy smaller than the superconducting gap.

An electron from normal metal that impinges on the superconductor with energy smaller than the gap can either be reflected as an elec-

---

[3] In this chapter, the motion of the Andreev reflected missing electronic state is described in terms of electronic wave vector.

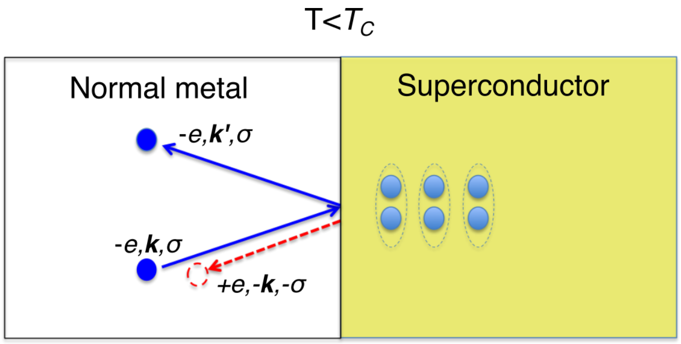

Figure 2.6: The Andreev scattering (reflection) in a normal metal that is in transparent electrical contact with a superconductor kept below its $T_C$.

tron with a specularly reflected wave vector $k'$ and original spin $\sigma$, or as a hole with exactly the opposite wave vector $-k$ and spin $-\sigma$. This means that the reflected hole would trace back exactly along the original path taken by the incoming electron, just like rewinding a video. In fact, one of the interesting features of Andreev reflection is that the superconductor couples the *time-reversed* quantum states with a correspondence of $k \to -k$, $\sigma \to -\sigma$ and$-e \to +e$, through the pairing potential (superconducting gap) $\Delta$. This coupling proceeds naturally from the fact that each Cooper pair in classical superconductors is comprised of electrons in time-reversed sates of each other.

### 2.3.2 *Normal or Andreev reflection?*

We have discussed the fact that when reflected from the N/S interface, an electron in a low-energy excitation state goes through one of two possible processes: The electron will either bounce back as an electron or Andreev-reflected as a hole. It will be helpful to see what determines the probability of these two distinctive events. Assume that the N/S interface is perfectly transparent; i.e., there is no other scattering potential despite the superconducting gap on the S side. And, also assume normal incidence of the incoming electron on the N/S interface. Under these assumptions, the only scattering force exerted on the electron is the negative potential gradient $-\nabla U$. We can estimate the force magnitude $F$ by considering the change of potential over a characteristic distance in the superconductivity as [4]

$$F = \frac{dU}{dx} \approx \frac{\Delta_{SC}}{\xi_0} \qquad (2.38)$$

---

[4] We follow the reasoning given in reference [95]

where $\Delta_{sc}$ is the superconducting gap and $\xi_0$ is the superconducting coherence length that can be viewed as the spatial extent (size) of a Cooper pair in a semiclassical picture. The force should cause a change in momentum by

$$\partial P = F\partial t = F\frac{2\xi_0}{v_F} \tag{2.39}$$

where $v_F$ is the Fermi velocity. Further, we assume that the particle experiences this force during a roundtrip over the distance $2\xi_0$. By plugging force $F$ into the expression of the change of momentum and rewriting force $F$ in terms of the Fermi momentum $P_F$ and the Fermi energy $E_F$, we obtain

$$\partial P = 2\frac{\Delta_{SC}}{v_F} = p_F\frac{\Delta_{SC}}{E_F}. \tag{2.40}$$

We see that the ratio between the momentum change caused by the superconducting gap and the incoming Fermi momentum is of the same order as $\Delta_{SC}/E_F$. This value is very small for metallic superconductors , as only a small fraction of the electron around the Fermi surface will form the paired-condensate upon the superconducting phase transition. In Nb ($T_C \sim$9K), for example, the ratio is ~ 1meV/5.4 eV~1.8$\times 10^{-4}$. As back-scattering an electron takes $\partial P = 2P_F$, normal reflection assisted solely by the superconducting gap is very unlikely. This reasoning also implies that to maximize the probability of the Andreev reflection at N/S interface, the electrical contact between the normal metal and the superconductor must be as clean (scatterer free) as possible. Formally, the transparency is characterized by $t = 1/(1+Z^2)$, where $Z$ is the barrier strength, which ranges from 0 for a perfect interface, to ∞ for a tunnel barrier[**?** ]. When the contact is perfect, i.e. $Z = 0, t = 1$, the Andreev reflection process dominates. One immediate consequence is that conductance is enhanced at a low bias ($V_{bias} < \Delta_{SC}$) and low temperature across the interface. In a ballistic system with a perfectly transparent N/S contact, each electron sent from the normal metal will end up in two electrons passing the interface, so that the conductance is twice as large as the conductance in the normal state.

### 2.3.3 *Andreev reflection and the Cooper pair transport across SNS junctions*

The fact that the superconducting gap, also called the pairing potential [5], couples two time-reversed quantum states of the electron and hole in normal metal suggests that the same process is possible for

---

[5] The two terms are equivalent in the BCS picture, and can also be interpreted as the density of Cooper pairs in the superconductor. It was shown later by Gorkov et al, that the gap is equivalent to the Ginzburg-Landau order parameter in the

hole excitation when the hole impinges on the N/S interface. Thus, a hole excitation characterized by $[+e, -k, -\sigma]$ from normal metal will be reflected by the superconductor as an electron characterized by $[-e, +k, +\sigma]$. This reflection provides a basis for considering an even more interesting situation: What happens when two N/S-interfaces are connected by a piece of normal metal?

Consider an SNS junction as illustrated in Figure 2.7. Two superconductors are linked by a piece of normal metal with length $L$. Let us assume the same transparent N/S interface as in our previous discussion, and let us assume further that there is no impurity scattering in the normal region. Under these assumptions, the Andreev reflection (AR) has the same probability of occurring at either interface. In equilibrium, the superconductor on the right converts an electron, denoted by $e_R$, into a hole excitation in its time-reversed state, which will trace the path taken by the electron back to the superconductor on the left-hand side. By the argument based on the symmetry described, the hole will pass through the N/S interface with another hole excitation that pairs with it (the Cooper pair of hole-like excitation). A Cooper pair of electrons is thus broken, and an electron, identical to $e_R$ in terms of charge, momentum and spin degree of freedom is ejected into the normal metal and completes a roundtrip on arriving at the superconductor on the right-hand side.

We can see that each roundtrip annihilates one Cooper pair in the left superconductor, and creates another Cooper pair in the right superconductor. Therefore, a Cooper pair is effectively transferred from left to right. This microscopic process gives rise to the transport of supercurrent across the *SNS* junction, in which current flows without dissipation from one superconductor to another by passing through a normal metal that is not inherently superconducting.

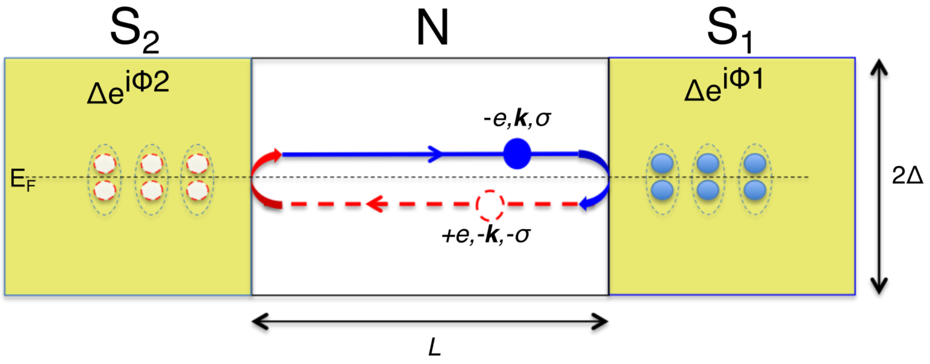

Figure 2.7: An SNS junction and Andreev roundtrips responsible for transporting Cooper pairs across a normal metal weak-link.

---

G-L formalism as proposed before BCS theory. In this thesis, we use these terms interchangeably in accordance with the context.

### 2.3.4 *Phase coherence in Andreev reflections*

As we have shown, through Andreev reflections at the N/S interface, some superconducting-like properties can be induced, at least in the proximity of the interface, in normal metals provided both metals are in good electrical contact. The most important property for the Andreev reflection and the proximity effect that follows is the phase coherence in the process.

The microscopic description of the superconducting state in an inhomogeneous system starts with the Bogoliubov-de Gennes equation for the electron- and hole-like wave functions $\psi_e(\vec{r})$, $\psi_h(\vec{r})$ of quasiparticles [39]:

$$\begin{pmatrix} H - E_F & \Delta(\vec{r}) \\ \Delta(\vec{r})^* & -(H^* - E_F) \end{pmatrix} \begin{pmatrix} \psi_e(\vec{r}) \\ \psi_h(\vec{r}) \end{pmatrix} = E \begin{pmatrix} \psi_e(\vec{r}) \\ \psi_h(\vec{r}) \end{pmatrix} \tag{2.41}$$

Here $H$ denotes the single particle hamiltonian of the system without superconductivity, $\Delta(\vec{r})$ the space dependent pairing potential (superconducting gap), $E_F$ the Fermi energy of the system, and $E$ the excitation energy measured with respect to $E_F$. The Bogoliubov-de Gennes equation describes the dynamics of electron- and hole-like excitations in a system with spatially-varying pairing potential $\Delta(\vec{r})$, in a way that is similar to how the Schrödinger equation describes the electron dynamics in a normal system.

An important distinction is the existence of the superconducting pairing potential $\Delta(\vec{r})$ as it couples the electron- and hole-like wave functions $\psi_e(\vec{r})$, $\psi_h(\vec{r})$ together. The coupling is the quantum mechanical description of the Andreev reflection process whereby an electron(hole) is absorbed into and a hole(electron) reflected onto the normal system. The Bogoliubov-de Gennes equation suggests that $\psi_e(\vec{r})$ and $\psi_h(\vec{r})$ are phase-correlated, meaning that there is a fixed relation between the phases of these two wave functions.

The phase acquired through the Andreev reflection that convert the incoming electron into a hole can be expressed as

$$\phi_{e \to h} = \phi_1 + \arccos(\frac{E}{\Delta}) \tag{2.42}$$

where $\phi_1$ denotes the phase of the superconductor on the right-hand side of Figure 2.7. The first phase term results from the requirement that particles absorbed by the superconductor must be in phase with the macroscopic wave function that describes the condensate. Therefore, the hole left behind by one of these particles will pick up the same phase. The second phase term $\arccos(\frac{E}{\Delta})$ comes from the reflection probability amplitude[18], which depends on the relative strength of the excitation energy $E$ and the barrier $\Delta$. Similarly, the same phase expression is expected for the opposite process:

$$\phi_{h\to e} = -\phi_2 + \arccos(\frac{E}{\Delta}). \tag{2.43}$$

We emphasize that so far, for simplicity, we have limited our discussion to ballistic normal metal, meaning that no scattering event takes place within the roundtrip. However, the general results presented here hold even for diffusive metals. P.W. Anderson pointed out[9] that in a highly disordered metal, where the Bloch wave vector $k$ is no longer a good quantum number, single-particle wave functions still come in time-reversed pairs i.e.

$$\psi_{i\uparrow}(r), \psi^*_{i\downarrow}(r).$$

The superconductivity is insensitive to the impurities as long as the phase coherence is preserved, whereas the characteristics of the dynamics differ depending on the regimes.

## 2.4 ANDREEV BOUND STATES IN BALLISTIC JUNCTIONS

We are ready to discuss one of the major topics of this thesis: supercurrent-carrying Andreev bound states (ABS). The current understanding in the field is that the Andreev reflection and the roundtrip taken by phase-correlated particles are responsible for the transport mechanism. However, the roundtrips differ in regard to the extent to which they contribute to the supercurrent transport: only the roundtrips that fulfill certain resonance conditions form energy bound states that dominate the transport in a superconducting regime.

### 2.4.1 *Transport resonance in the Andreev process*

The bound-state energy can be obtained by requiring the phase accumulated in the Andreev process to be multiples of $2\pi$. Processes that satisfy this requirement result in constructive interference of probability and will dominate the signal that can be measured.

Let us consider the roundtrip taken by the phase-conjugated electron and the hole excitation depicted in Figure 2.7. The phase related to the Andreev reflection is given by eqns. (2.42) and (2.43). In addition, the dynamic phase $\phi_{e(h)} = \int \overrightarrow{k_{e(h)}} \cdot d\vec{l}$ acquired by the traversing of the electron(hole) between the superconductors also contributes to the total phase accumulation. In a one-dimensional ballistic case, the phase picked-up by an electron traveling from $S_2$to $S_1$ can be calculated simply as

$$\phi_e = k_e \cdot L = \sqrt{\frac{2m}{\hbar^2}(E + E_F)} \cdot L \tag{2.44}$$

and for the hole that travels from $S_1$ to $S_2$, with excitation energy smaller than Fermi energy $E_F$, the dynamic phase is

$$\phi_h = k_h \cdot (-L) = \sqrt{\frac{2m}{\hbar^2}(E_F - E)} \cdot (-L). \tag{2.45}$$

As $E \ll E_F$, the total dynamic phase can be written as

$$\phi_e + \phi_h = k_F L \frac{E}{E_F} \tag{2.46}$$

to the first order approximation. We can now write the resonance condition for the total phase acquired in a roundtrip taken by the electron-hole pair coupled by the Andreev reflection as follows:

$$2 \arccos(\frac{E}{\Delta}) \pm (\phi_1 - \phi_2) + k_F L \frac{E}{E_F} = 2\pi n, \tag{2.47}$$

where n is an integer and ± accounts for the two possible directions the roundtrip can take. This resonance condition was first established by Kulik, who rendered it for a clean $S - N - S$ junction[83]. He showed that from this expression, the bound-state energy as a function phase difference between $S_1$ and $S_2$ can be found.

Before we demonstrate this, let's first look at the phase term associated with the junction length $L$. Eqns. (2.44) and (2.45) show that the individual dynamic phase of Andreev-conjugated electron and hole is not identical for $|E| \neq 0$. It is also suggested that the Andreev-reflected hole does not completely "erase" the phase footprint left by the incoming electron in a retro-reflection process. Thus, the net phase difference between the two motions, by electron and hole respectively, is given by $k_F L \frac{E}{E_F}$. The phase coherence between the Andreev-reflected electron-and- hole pair can be maintained only up to a certain distance, which is determined by $|E|$, the magnitude of the excitation energy.

### 2.4.2 *Andreev bound states in a short junction limit*

The $k_F L \frac{E}{E_F}$ term also gives us the criteria to distinguish between short- and long-junction limits. The junction is "short" if this term is negligible, so that the phase depends almost completely on the Andreev reflection and is insensitive to the geometry. This is equivalent to the condition $L \ll \xi$, where $\xi = \hbar v_F / 2\Delta$ is the coherence length in ballistic normal metal [6]. In the short-junction limit, the bound state energy can be solved from eqn. (2.47) as:

$$E^{\pm}_{A,L\ll\xi}(\Delta\phi) = \pm\Delta\cos(\frac{\Delta\phi}{2}), -\pi < \Delta\phi < \pi \tag{2.48}$$

where $\Delta\phi = \phi_1 - \phi_2$ is the phase difference between the two superconductors. Only one $\mid E_{ABS} \mid$ is allowed within $\Delta$.

### 2.4.3 *Andreev bound states in a long junction limit*

In the opposite limit, i.e., where $L$ is much larger than the coherence length while the metal remains ballistic, the phase acquired in each roundtrip is dominated by the term associated with $L$. In addition, due to the weaker quantum confinement in a long junction as compared to that in a short junction, the energy spacing between bound states decreases with $L$ and thus multiple bound states can be accommodated within the gap. The low-energy ($E \ll \Delta$) spectrum for the bound states can be expressed as

$$E^{\pm}_{A,L\gg\xi}(\Delta\phi) = \frac{\hbar v_F}{L}\left[(n-\frac{1}{2})\pi \mp \frac{\Delta\phi}{2}\right], -\pi < \Delta\phi < \pi \tag{2.49}$$

In both limits, phases of the macroscopic wavefunctions in superconductors play the central role in the dynamic of the normal region, where essentially no Cooper pairs are present. In a ballistic SNS junction with given geometry, it completely determines the the spectrum of energy bound states at equilibrium, without the application of any bias or other means of intervention. Dependence on the superconducting phase difference is a signature property of Andreev bound states. The phase dependence provides a very powerful tool for investigating the proximitized system.

### 2.4.4 *Andreev bound state and the supercurrent transport in an SNS junction*

We have established the relation between the Andreev reflection and the (effective) transport of Cooper pairs across an SNS junction, as well as the phase dependence of the Andreev bound state that carries supercurrent in short- and long-junction limit. However, the relation between the supercurrent and Andreev bounds states might not be as straightforward as it appears. In fact in our discussion earlier, we note that for each Andreev bound state, there is a degenerate state in which the carrier moves in the direction opposed to its degenerate counterpart, which cancels out the current flow carried by its coun-

---

[6] This is readily derived from $k_F L \frac{E}{E_F} \ll 1$ by substituting $E$ with the gap energy $\Delta$ as the upper bound.

terpart at the same energy. Does this mean that the net supercurrent should be zero according to this model?

To clarify this subtle issue, it should be noted that the Andreev bound states are simply discrete energy levels within the gap [7] that maybe occupied by quasiparticles in the normal metal. To obtain the total supercurrent, it is necessary to add up the electrical current[10] $I_n^{\pm}(\phi)$ [8] carried by quasiparticles occupying each Andreev level $E^{\pm}_{ABS(n)}(\phi)$ (under the assumption that $\mid E_{ABS(n)} \mid < \Delta$, so that the levels are discrete). As the supercurrent flows at thermal equilibrium, we assume that the levels are thermally populated by the quasiparticles according to the Fermi distribution function $f(E)$. The total current $I_d(\phi)$ contributed by the quasiparticles occupying all Andreev levels is

$$I_d(\phi) = \sum_n \{ I_n^+(\phi) f(E^+_{ABS(n)}(\phi)) + I_n^-(\phi) f(E^-_{ABS(n)}(\phi)) \}, \tag{2.50}$$

where the index "+(-)" denotes the left(right) moving particles at a level above(below) the Fermi energy $E_F$. From this perspective, the expectation is that only levels below the Fermi energy ($E_{ABS(n)} \leq 0$, measured with respect to $E_F$) can contribute to the supercurrent at $T = 0$. At $T \neq 0$, the imbalance of occupancy between the right- and left-moving states gives rise to a finite net supercurrent.

## 2.5 ANDREEV BOUND STATES IN DISORDERED JUNCTIONS

In the previous sections, we discussed the Andreev bound states in a ballistic (scattering-free) channel. In practice, it is difficult to achieve an absolutely impurity-free channel. The scattering source can be disorder in the normal metal or in the barrier between the superconductors and the normal metal. No matter its origin, the scattering results in a modification to the ABS energy spectrum and the corresponding supercurrent characteristics.

### 2.5.1 *Channel with a single point impurity*

Following Philip Bagwell ([10]), we model the impurity by a point potential placed inside the junction

$$V(x) = V_s \delta(x - a), \tag{2.51}$$

---

[7] We confine ourselves to the bound states within the gap. There exists, however, an energy continuum above the gap that also contributes to the total supercurrent which we will discuss in Chapter 5.

[8] For brevity, we use $\phi$ in place of $\Delta\phi$ from now on, as we can always set $\phi_2$ to zero without changing any of the physics.

where $0 \leq a \leq L$. The single-particle Hamiltonian that we used in the Bogoliubov-de Gennes equation (2.41) now becomes

$$H(x) = \frac{1}{2m}\left(\frac{\hbar}{i}\frac{d}{dx} - eA(x)\right)^2 + V(x). \tag{2.52}$$

We anticipate that elastic scattering between the electron and the potential will only introduce an extra phase shift, which can be absorbed into an effective phase term $\alpha$ that we will use to calculate the resonance condition. Hence, eqn. (2.47) can be rewritten as

$$2\arccos(\frac{E}{\Delta}) + \left(\frac{L}{\xi}\right)\left(\frac{E}{\Delta}\right) \pm \alpha = 2\pi n, \tag{2.53}$$

where we have rearranged the term associated with junction length $L$ in terms of $\Delta$ and coherence length $\xi = \frac{\hbar v_F}{2\Delta}$.

The effective phase $\alpha$ is defined by[10]

$$\cos\alpha = \tau cos(\phi) + \rho\cos\left[(\frac{L-2a}{\xi})(\frac{E}{\Delta})\right]. \tag{2.54}$$

Here, $\phi$ is the phase difference between $S_1$ and $S_2$, as we have set $\phi_2 = 0$. $\tau$ and $\rho$ are the normal electron transmission and reflection probability, respectively, through the channel given by a point-like $(\delta - function)$ potential:

$$\tau = 1 - \rho = \frac{1}{1 + (mV_s/\hbar^2 k_F)^2}. \tag{2.55}$$

We can see from eqn.(2.54) that if $\tau \to 1$, the impurity plays almost no role and the Andreev reflection is recovered for a ballistic channel. In the opposite limit, where $\tau \to 0$, the bound state becomes independent of the phase $\phi$ in the superconductor. This is the case because the particle is strongly confined in the channel, in which the bound state energy depends on the position of the potential barrier that defines the configuration of the cavity. The second term in the expression of the effective phase , eqn.(2.54), also suggests that the scattering potential contributes to the total acquired-phase in a similar way as in the dynamic phase, which is the phase the electron and hole would gain by traveling between the leads. From this perspective, we can say that the scattering effectively increases the junction length [9].

---

[9] This can be understood intuitively, as with $\tau < 1$, the electron must make multiple attempts to pass the barrier. Bouncing back and forth between the barrier and leads increases the average distance it needs to travel to complete an Andreev roundtrip.

### 2.5.2 *Andreev bound states in a short junction with impurity*

When the junction length $L$ is much shorter than the coherence length $\xi$, we omit the term associated with $L$ in eqn. (2.53) and solve for the bound state energy for a 1-D channel as in eqn.(2.4.2):

$$E^{\pm}_{A,L\ll\xi} = \pm\Delta\cos(\frac{\alpha}{2}) = \pm\Delta\sqrt{1-\tau sin^2(\frac{\phi}{2})}, \tag{2.56}$$

where

$$cos(\alpha) = \tau cos(\phi) + \rho. \tag{2.57}$$

This is similar to the $E^{\pm}_{A}$ in a short ballistic channel ($E^{\pm}_{A}$=$\pm cos(\phi/2)$) except that the degeneracy at $\phi = \pi$ is lifted. Furthermore, an energy gap is opened at $\phi = \pi$, as given by

$$E_{gap} = 2\Delta\sqrt{\rho}. \tag{2.58}$$

Note that in a impurity free channel, $E^{\pm}_{A}$ correspond to left- and right-moving states that are independent to each other. The presence of an impurity mixes the states going in opposite directions ,as the electron has a finite probability of back-scattering upon impinging on the potential. This back-scattering, which is most pronounced at the degeneracy point $\phi = \pi$, changes the entire spectrum of $E^{\pm}_{A}$ in exactly the opposite way, such that one travel direction becomes more energetically favored than the other.

### 2.5.3 *Andreev bound states in a long junction with impurity*

In the opposite limit where $L \gg \xi$, with low energy excitation $E \ll \Delta$,we obtain from eqn.(2.53):

$$E^{\pm}_{a} \sim \frac{\Delta\xi}{L}\left(2\pi n - \pi \mp \alpha\right) = \frac{\hbar v_F}{2L}\left(2\pi n - \pi \mp \alpha\right). \tag{2.59}$$

To see explicitly how the energy bound states vary with the superconducting phase $\phi$, we can rearrange eqn.(2.54) and write

$$cos^2(\frac{\alpha}{2}) = 1 - \tau sin^2(\frac{\phi}{2}) - \rho sin^2\left(\frac{(L-2a)E}{2\Delta\xi}\right). \tag{2.60}$$

If we place the impurity at the mid-point ($a = L/2$), the bound state energy becomes

$$E^{\pm}_{A} \sim \pi\left(\frac{\hbar v_F}{2L}\right)\left\{2n - 1 \mp \frac{2}{\pi}cos^{-1}\left[\sqrt{1-\tau sin^2(\frac{\phi}{2})}\right]\right\}. \tag{2.61}$$

The gap at $\phi = \pi$ around $E = 0$ can be obtained by taking the difference between $E_A^-(n)$ and $E_A^+(n-1)$, which yields

$$E_{gap} = 2\pi \left(\frac{\hbar v_F}{2L}\right) \left(1 - \frac{2}{\pi} cos^{-1}\sqrt{\rho}\right). \tag{2.62}$$

For small $\rho$, $cos^{-1}\sqrt{\rho}$ can be approximated by $\left(\frac{\pi}{2} - \sqrt{\rho}\right)$, such that

$$E_{gap} \sim 2 \left(\frac{\hbar v_F}{L}\right) \sqrt{\rho}. \tag{2.63}$$

We see that even when more states are packed within the superconducting gap $\Delta$ rather than only one $\mid E_A \mid$, the basic characteristics of ABS in long and short junctions in the presence of impurity are qualitatively similar. The degeneracy at $\phi = \pi$ which appears in the clean junctions is lifted due to the finite back-scattering rate, and the energy gap between neighboring left- and right-moving states is proportional to the square root of the reflection probability $\rho$. However, in the short-junction limit, $E_{gap}$ scales with the superconducting gap $\Delta$, whereas in the long-junction limit, the gap energy scales with the level spacing $\frac{\hbar v_F}{L}$ associated with the quantum confinement imposed by the device geometry.

In chapter 5, we have the opportunity to study devices as described in Figure 2.4, which allows us to see the manifestation of the theory that we discussed in this chapter.

# 3

# SUPERCURRENT TRANSPORT IN DIFFUSIVE GRAPHENE NANODEVICES

Our study of the superconducting proximity effect in graphene starts from the fabrication and characterization of superconductor-graphene-superconductor (SGS) junctions. The flow of zero-voltage bias current across the leads could be regarded as a benchmark for strong coupling between the superconductor and the graphene. This flow also ensures that the electronic temperature in the cryostat is well below the Josephson coupling energy of the hybrid system.

Basic graphene device fabrication techniques are presented in this chapter. In particular, some implementation issues and other issues likely to arise with sputtering deposition of metals on atomic thin layers will be discussed.

A cryo-free dilution refrigerator, and the associated measurement setup we use for superconducting devices are introduced. In particular, the implementation of a low-pass filtering setup, which is crucial to this type of measurements, is discussed.

## 3.1 NBN-GRAPHENE-NBN JOSEPHSON JUNCTIONS

Niobium nitride (NbN) is a type II superconductor with a relatively high $T_c$(about 10~14K, depending on growing condition and thickness). The induced superconducting gap in graphene contacted by NbN is expected to be 10 times larger than that induced by aluminum, which is commonly used in studies of SGS systems. In comparison, this larger superconducting gap results in a more "robust" proximity effect in graphene, which shows a higher critical current and an improved immunity to noise. SN- or SNS junctions made by a type II superconductor with large $H_{c2}$ (typically a few tesla) also provide the opportunity to study the magneto transport of superconducting charge carriers, such as the Andreev reflection at high magnetic field[51, 71], focused crossed Andreev reflection[69], and the coupling between Cooper pairs and quantum Hall states[116, 117, 138].

## 3.2 DEVICE FABRICATION

To fabricate an SGS device, a graphene monolayer is prepared by mechanical exfoliation following the procedure first developed by Geim et al[97]. Highly doped (conductivity: 0.001~0.005 ohm-cm) Si wafer (NOVA electronics, item # FP02-61160-AS), topped with 285 nm thermally grown $SiO_2$, serves as the substrate and backgate for the device. The thermal oxide is dry-chlorinated and annealed in forming gas by the manufacturer in order to reduce the charge trap in the oxide layer, which might otherwise dope the graphene. The alignment marker is defined by e-beam lithography followed by the deposition of 5 nm of chromium and 120 nm of gold. E-beam-defined marker typically gives alignment precision to within 100 nm. A standard Piranha cleaning (Appendix A.1) is performed on the substrate before the graphene deposition. After the proper graphene monolayer has been identified under an optical microscope, pictures of the flake are taken with respect to neighboring markers and imported to CAD software for patterning design. The lines that make up the pattern are 1 µm wide and are typically separated from each other by 500 nm for Josephson junctions. E-beam exposure (30 KeV, Raith 150) is performed on the PMMA (polymethyl methacrylate) tri-layer (discussed in 3.2.3) with a dosage of ~ 300 $\mu C/cm^2$. After lithography, the sample is immersed in a solution of MIBK (methyl isobutyl ketone) and IPA (isopropyl alcohol), with a 1:1 ratio, for one minute to dissolve the exposed PMMA. We use MIBK:IPA =1:1 instead of the standard 1:3 solution to achieve a more aggressive development, which leaves less PMMA residue in the developed area than the standard recipe would. Ti (5nm) and NbN (45 nm) thin films are deposited on the developed sample with a UHV magnetron sputtering system (discussed in 3.2.1), followed by a lift-off of the resists with acetone kept at 60°C. The sample is then ready to be measured. More details about the nanofabrication techniques are discussed in the following sections.

### 3.2.1 *Sputtering deposition of superconductor on monolayer graphene*

Sputtering deposition is a technique that is widely used to deposit dielectrics or metals with very high melting points, to which other physical vapor deposition, such as e-beam or thermal evaporation, is not applicable [1]. In a typical sputtering deposition process, gaseous plasma is first created in the chamber, and the ions from the plasma are accelerated toward the source material (target), which is mounted on a negatively-charged electrode. The energized ions erode the target via energy transfer and eject the source material in the form of neutral particles. A neutral particle travels in a straight line unless it collides with other particles in the chamber. Thus, if a substrate is placed in the path of these particles, it will eventually be coated with a thin film of the source material[1]. The working principle, namely the stochastic nature of sputtering deposition achieved by kinetic en-

---

[1] We did try to evaporate pure Nb onto some devices using a high-power e-beam evaporator. The resist (PMMA) hardened and cracked all over the entire surface. We think that the high energy radiation generated during e-beam evaporation cross-linked the PMMA, which actually can, in fact, be used as a negative-tone resist when exposed to UV.

ergy transfer among materials, implies two main issues in regard to the nanofabrication of graphene devices.

### 3.2.2 *Damage to graphene by energetic particles in sputtering*

The energetic particles such as ions, clusters of source material,and high-speed neutral gas atoms that populate the chamber during the sputtering process can damage the graphene's surface. Raman spectroscopy performed on graphene coated with thin sputtered film has shown significant suppression of the characteristic G and 2D peaks and a pronounced D peak, suggesting the amorphization of the $sp^2$C-C bonding[46, 74]. In addition, the damage caused to a multi-layer flake decreases as the number of layers increases. Further investigation by controlling the sputtering condition such as incident angle, substrate temperature, discharge power density, and pressure, shows that the gas neutrals constitute the primary cause of damage in graphene[30].

Note that in a DC magnetron sputtering setup, as is the case presented here, charged particles, including ionized Ar and ionized sputtered target species , seldom reach the substrate, as they are strongly confined around the cathode region by the electrostatic field. The two remaining kinds of energetic neutral particles are (1) the sputtered target species, of which the kinetic energy typically lies below 10 eV[128],and (2) the high-speed gas neutral , such as Ar atoms in the present case, created either by a recombination of Ar ions or a collision with other energetic particles. In fact the gas neutral is shown to be the dominant species in the energetic particles that bombard on graphene surface[30].

It is also discovered that the grazing-angle configuration, elevated substrate temperature (up to 200 °C), low discharge power density (controlled by the target bias voltage) and low processing pressure (<5 mTorr) in a DC sputtering process can preserve the crystallinity of graphene to an extent that is comparable to the result that can be obtained by e-beam evaporation [30].

Table 3.1 summarizes the typical sputtering condition of DC [2] magnetron sputtering for the devices discussed in this chapter. Instead of being formed by sputtering directly a NbN target, the compound is formed by reactive sputtering, that is, by sputtering Nb in a mixture of Ar and $N_2$ gases. Following this recipe, we consistently obtain NbN thin film (~ 40 nm) with a $T_c$ ~ 12K, and the film remains super-

---

[2] We found that our graphene device can only be contacted by DC sputtering. The RF mode of magnetron sputtering leads to very high contact resistance ( a few kilo ohms) , which prohibits the proximity effect. This is consistent with the finding in [30],as in RF sputtering, the polarity of the target is reversed every half cycle, allowing the charged particle to escape from the electrostatic confinement and reach the substrate with higher probability.

conducting up to at least 9 tesla, which is the highest magnetic field achievable in the cryostat.

| Parameter | Experiment condition |
|---|---|
| Chamber base pressure | 5x10$^{-9}$ Torr |
| Sputtering temperature | 50 °C |
| Sputtering pressure | 3 mTorr |
| Argon gas flow | 100 SCCM* |
| Nitrogen gas flow | 13 SCCM* |
| Beam incidence angle | ~ 45 degree |
| Distance from target to substrate | ~ 40 cm |
| DC power (for Ti target) | 300 watts |
| DC power (for Nb target) | 180 watts |
| Deposition rate | Ti: 0.1Å/sec, NbN: 1Å/sec |

*Standard cubic centimeter per minute

Table 3.1: Sputtering condition for making NbN-graphene-NbN Josephson junctions.

### 3.2.3 *Tri-layer PMMA resist for sputtering deposition and lift-off of Ti/NbN*

Given the isotropic nature of the sputtering process, we developed a tri-layer PMMA (polymethyl methacrylate) resist structure for e-beam lithography. PMMA 950 A4 (950,000 molecular weight, 4% in anisole, from MicroChem) on the top and the bottom layers guarantees high resolution in e-beam patterning whereas a more sensitive PMMA 120 A5 middle layer facilitates a pronounced undercut for the lift-off step. This PMMA structure allows us to easily lift off the sputtered thin film using acetone. Fig.3.1 illustrates (a) the stacking order and thickness of the tri-layer resist ,(b) the SEM micrographs of under cut, and (c) the NbN pattern after lift-off.

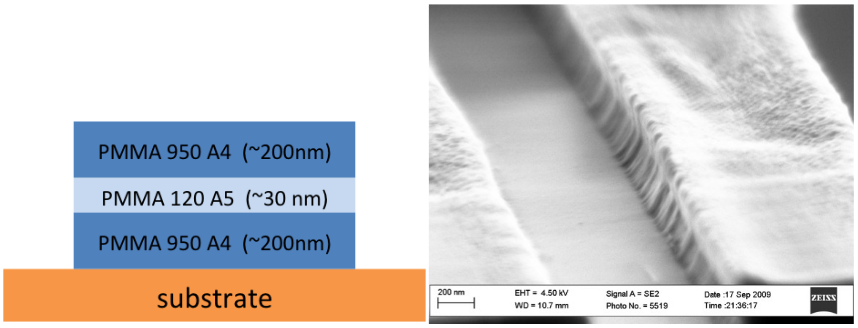

(a) Tri-layer PMMA structure.

(b) SEM (scanning electron microscope) image of the PMMA tri-layer resist after exposure and development. Pronounced undercut can be observed in the middle of the image.

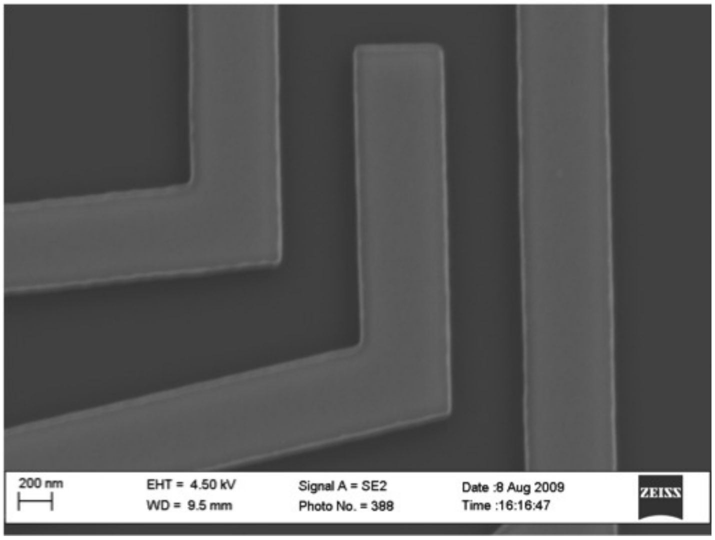

(c) SEM image of NbN pattern after lift-off in acetone. The pronounced undercut rendered by PMMA tri-layer enables a clean lift-off of metal, compatible with an isotropic metallization.

Figure 3.1: PMMA tri-layer stack for NbN sputtering and lift-off.

## 3.3 MEASUREMENT SETUP

### 3.3.1 *Cryo-free dilution refrigerator*

#### 3.3.1.1 *Pulse-tube cryocooler*

All quantum transport and spectroscopy measurements presented in this thesis are performed in our cryo-free dilution refrigerator (Leiden Cryogenics BV CF-450). The cryo-free system, usually referred to as a “dry fridge” because it does not need to be immersed in liquid helium, uses a closed-loop cryocooler to provide cooling power from room temperature to around 4K. Compared to a typical “wet fridge", the closed-loop system eliminates the cost of liquid helium, and requires less supervision during long measurement sessions. Our system uses a pulse-tube cryocooler which offers several significant advantages over other closed-loop cryocooler designs[50]. Specifically, the pulse-tube cryocooler has no moving parts at the cold end; therefore it vibrates less and in principle requires less maintenance than do other kind of cryocoolers. Modern design typically consists of two stages of pulse-tube cooling to achieve a temperature as low as 2K. Here, we show how a basic single-stage pulse-tube cryocooler works in order to capture the principle of operation.

Figure 3.2 shows the basic elements of a pulse tube cryocooler. The refrigeration cycle starts when the *piston* moves down to compress room-temperature helium gas to go through the *regenerator*, and pass the *cold stage* of the pulse tube. This hot compressed gas flows through a constriction into a *reservoir* that is kept at room temperature, while releasing the heat $q_{\mathrm{hot}}$ through a heat exchanger when passing the hot end of pulse tube. The gas flow stops when the pressure in the pulse tube equals that in the reservoir. The piston then moves up and causes the gas in the pulse tube to cool down due to *adiabatic expansion*. The cold, low-pressure gas in the pulse tube is forced back through the heat exchanger at the cold end by the reverse flow from the reservoir, the pressure of which becomes higher instantaneously, and absorbs heat $q_{\mathrm{cold}}$ from the cold stage. This back flow stops when the pressure in the pulse tube is in equilibrium with the pressure in the reservoir, such that one cycle is completed. The pulse tube must be well insulated at each of its ends and it must have sufficient volume so that the hot gas from the hot end never reaches the cold end in a cycle and vice versa. In fact, the gas in the middle of the tube never leaves the tube, thereby forming a temperature gradient that insulates both ends. Finally, the *regenerator*, which is made of materials with a large heat capacity and a large surface area, is a heat exchanger that pre-cools the incoming compressed gas before it reaches the cold end of the pulse tube. The heat is stored in the regenerator during the first half of the cycle, and is removed by the up-flowing cold gas.

#### 3.3.1.2 *Dilution refrigeration*

The cryostat cools to a temperature below 300 mK by dilution refrigeration[54]. This process uses a mixture of $^3$He and $^4$He gas, the two isotopes of helium, which is pre-cooled to a temperature below 1K by the pulse-tube refrigeration and pumping of the mixture. At temperature below 870 mK, the mixture undergoes spontaneous phase separation into an $^3$He-concentrated phase (highly purified $^3$He) and a diluted phase composed of 6.4% $^3$He in 93.6% $^4$He liquids. At equilibrium, the phase boundary is designed to settle within the *mixing chamber*, where the $^3$He-concentrated phase sits on top of the diluted phase of the mixture. $^3$He is the moving liquid in normal circulation driven by

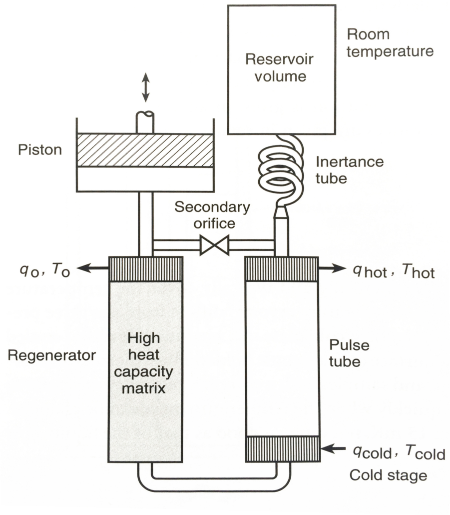

Figure 3.2: Operation of a pulse-tube cryocooler. Image adapted from [50]

several pumps within the mixture circuits. It is diluted when crossing the phase separation boundary from the concentrated phase to the diluted phase. Because the process of crossing the boundary is endothermic in nature, $^3$He absorbs heat from the environment and thus provides the cooling power of the fridge in a sub 1K regime. The diluted $^3$He leaves the mixing chamber and enters the "still" (i.e., the distillation chamber) , in which a gas-liquid phase boundary is maintained by pumping. The pump pumps out gaseous $^3$He, compresses it through cold capillary impedance, and the feeds $^3$He liquid back into mixing chamber (concentrated phase) to complete a cycle.

### 3.3.2 *Filtering for quantum transport measurement*

#### 3.3.2.1 *Why do we need to filter the signals?*

From the principle of dilution refrigeration discussed in the subsection 3.3.1.2, it is evident that the mixing chamber has the lowest temperature, known as the base temperature, inside a dilution fridge. Therefore, if it is to reach the lowest temperature possible, the sample must be thermally anchored to the mixing chamber plate. However, thermally anchoring the sample in this way does not guarantee that the sample will reach and then stay at the base temperature during the measurement for two reasons: First, thermal coupling between the sample and the cryostat is significantly suppressed at low temperature due to the reduction of phonon modes, which is responsible for the thermal conductivity in the lattice. Secondly, the leads that connect the device to the apparatus at room temperature constantly feed the "hot electrons" into the mesoscopic devices[124]. This implies that

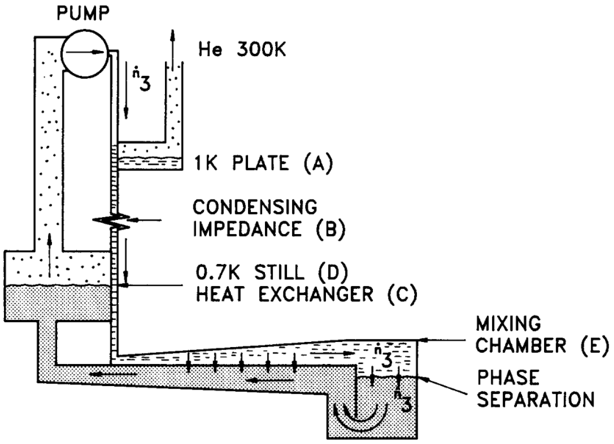

Figure 3.3: Schematic view of dilution refrigeration (adapted from [54])

electromagnetic noise at a frequency of up to 300 K $k_b/h$ ~ 6T Hz may couple to the device, for which the characteristic energy scale might be much smaller. For instance, NbN ($T_c$~10K in our experiment) has a BCS gap of 0.5 T Hz and a Josephson coupling energy $E_j$that can be as small as a fraction of the gap. In order to measure sizable Josephson current in Josephson junctions, it is necessary to reject high frequency (G Hz ) electromagnetic noise , i.e., the "hot electrons".

Most of the solutions proposed to effectively thermalize the experiment at milli-kelvin temperature rely on shielded distributive RC filters [110, 124, 85]. In comparison with reflective filters, RC filters, given their dissipative nature, are less sensitive to impedance mismatches in the rest of the lines, from which spurious transmission resonance may arise. Further, it is necessary for the RC filters to thermalize well with the mixing chamber in order to avoid a situation in which the latter generates thermal noise by itself.

#### 3.3.2.2 *Noise filtering using distributive RC filter*

Traditionally, low-pass filtering in an RF regime is achieved using a powder filter[90], in which each line consists of a copper tube filled with metallic powder (typically stainless steel or copper) with 1-meter-long resistive wire coils inside. Each channel terminates with a coaxial connector (e.g., SMA connector ) and the entire filter connects to coaxial cables. The space taken up by each channel and the amount of mass (~ 100 grams/wire) that must be cooled down significantly limits the number of DC lines that can be installed in a cryostat. In address this limitation, several designs have been proposed and investigated including micro fabricated filters[124, 85], silver-epoxy filters[110], thermo-coax cables, and lossy transmission lines[114, 17].

Our homemade RF filter is made in accordance with the design developed by Spietz *et al.* from Robert Schoelkopf's group [115]. The

(a) Leiden CF-450 dilution refrigerator

(b) Gas handling system panel

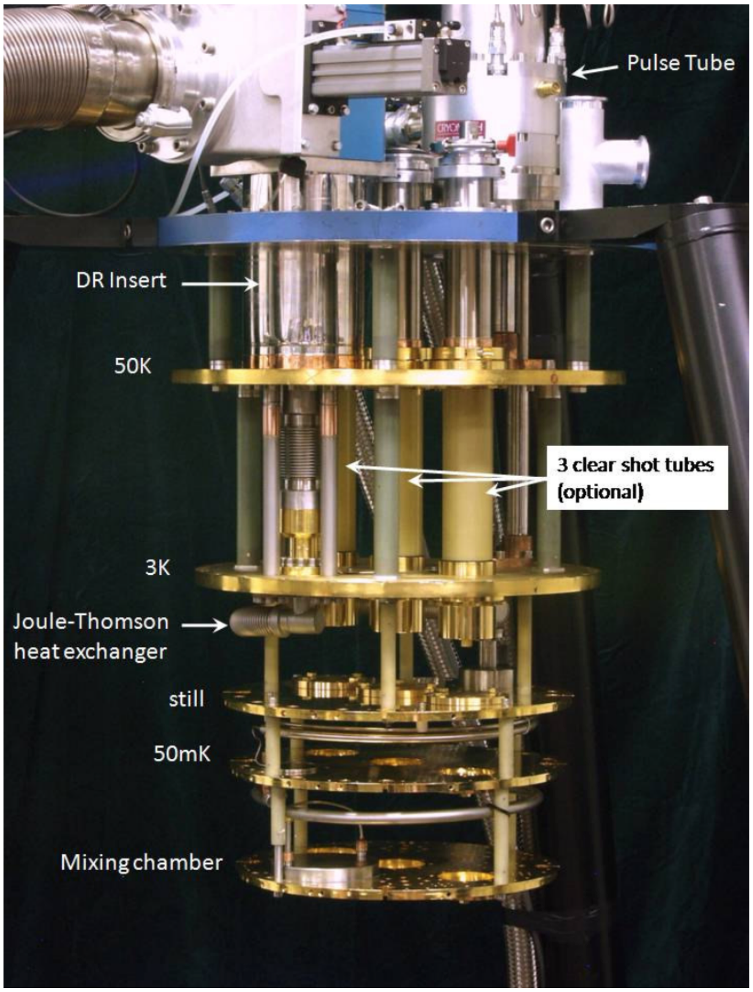

(c) Cf-450 DR (dilution refrigerator) unit (adapted from user's manual by Leiden Cryogenics)

Figure 3.4: Image of cryo-free dilution refrigerator

filter consists of twisted resistive wires tightly enclosed in copper tape (Fig.3.5 (a)). The tape acts both as the shield and the ground, to which wires are capacitively coupled. The combination of the high resistivity of the wire and its high capacitance to ground forms the distributive RC filter. This "copper tape filter" has several advantages over other customized designs: (1) it is relatively easy to make and requires minimal machining and no microfabrication processing; (2) the entire filter is compact in size and can easily be bent to fit into the space of the cryogenic stage; (3) it allows numerous lines (24 in our filter) to be packed into one filter without taking up either too much space or requiring too much cooling power.

To make the copper tape filter, insulated Manganin wires (dia. 0.004 inches, MWS Wire Industry item # 1357) are twisted together to form pairs of wires. Every four pairs of wires are enclosed in a single copper tape (3M # 1194), which is folded in half lengthwise and pressed with force to ensure a light-tight seal. Three identical copper tape filters were made and fit into grooves cut from a copper block (Fig.3.5 (b)), mounted on the (grounded) mixing chamber for thermalization. Each copper tape filter is about 2 meters long, and the resistance of each line is 120∓2 Ω. The tapes are joined together at both ends by two connectors (Cristek M83513/07-D ) ,which can readily connect to the rest of the lines.

In order to test the performance of the copper tape filter in as close to real-life condition as possible, we plugged the filter into a measurement circuit that runs from a BNC breakout box outside the fridge to the chip carrier on the cold finger. The transmission as a function of frequency was measured on an Agilent E5071C network analyzer from 100 KHz to 8.5 GHz with the fridge fully open. Figure 3.5(c) shows the measurement taken over 15 different channels across all three tape filters. In all the channels, -20 dB attenuation occurs at ~ 7 MHz, and -40 dB at 12 MHz ~ 23 MHz, well below the NbN superconducting gap at ~ 500 GHz. The filtering characteristics are similar to those in the filters presented in Ref.[115]. Note that we performed the transmission test in an open-fridge setup at room temperature, such that it is reasonable to assume that we captured the lower bound of the filtering capability. Characterization of electronic temperature of the DC lines revealed by tunneling spectroscopy is discussed in 5.4.

### 3.3.3 *Pseudo four-probe measurement of graphene Josephson junctions*

The proximity effect requires two electrodes to be in close proximity to each other. It is, therefore, difficult to perform a standard four-probe measurement of the device at mesoscopic scale. Instead, a "pseudo-four" probe measurement with superconducting leads can be taken in order to extract information about the 2-DEGS. Figure 3.6 shows a typical pseudo four-probe current bias measurement configuration

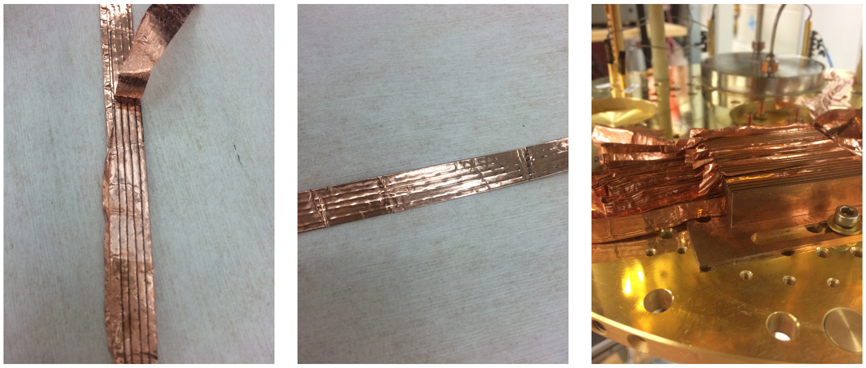

(a) Twisted pairs of resistive manganin wires embedded in the copper tape (opened for illustration).

(b) Copper tape filter after completion. Each tape includes 4 twisted-pairs of manganin wire.

(c) Installation and thermal anchoring of the copper tape filter on the mixing chamber plate.

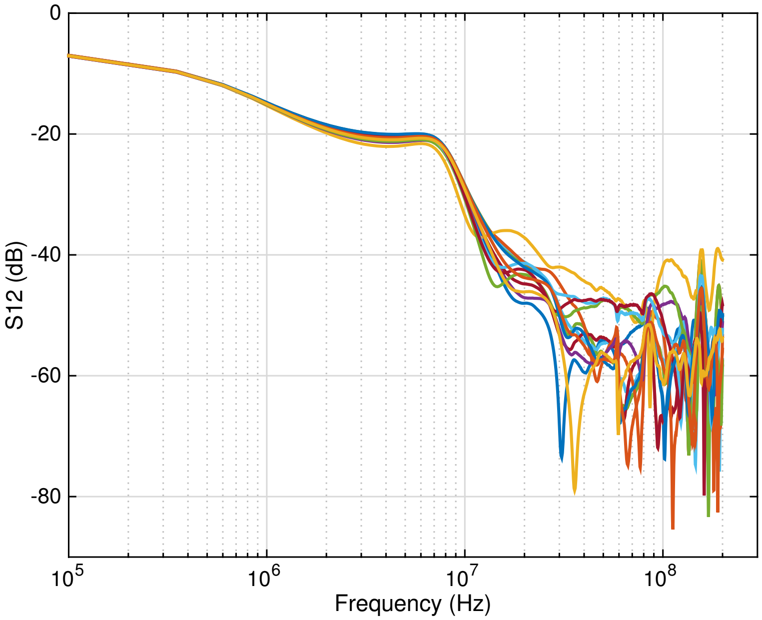

(d) Attenuation of transmission as a function of frequency, characterized for 15 different channels in our copper tapes. The -20dB point occurs at ~7 MHz. Well below the frequency corresponding to the NbN gap.

Figure 3.5: Copper tape filter

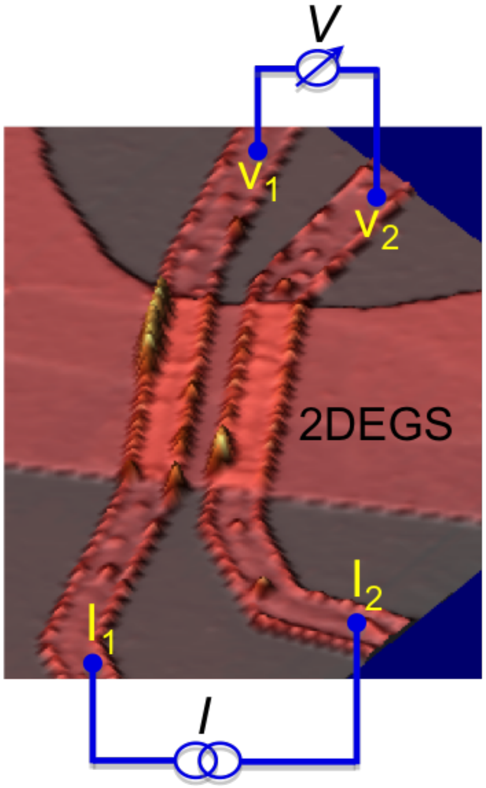

Figure 3.6: Pseudo-four probe configuration for measuring Josephson effect in a mesoscopic device.

across a piece of 2-dimensional material in contact with superconductors. If bias current I is injected from $I_1$ to $I_2$ and the voltage drop V is measured at $V_1$ with respect to $V_2$, the extracted resistance R is equal to $R_{2DEGS}+2R_{contact}$, provided that all the leads are superconducting so that no voltage drop occurs in any of the leads. In an SNS junction, the contact resistance $R_{contact}$ is small so that the extracted R is dominated by $R_{2DEGS}$, which is exactly what we want to study.

## 3.4 MEASUREMENT RESULTS

### 3.4.1 *Normal state characterization and quantum Hall measurement*

#### 3.4.1.1 *Field effect mobility and the mean free path of the junctions*

We first measured the sample at 4K in order to study the normal (non-superconducting) properties of the devices. At 4K, all the NbN leads were superconducting, but the temperature was still too high for the graphene to be fully proximitized. All the measurements presented in this chapter were taken using the pseudo-four probe technique as discussed in 3.3.3 unless otherwise noted.

Figure 3.7 shows the measurement taken in a standard monolayer graphene Josephson junction, with a lead-to-lead distance $L$ of 500 nm [3]. This junction (circled in red), with $LxW = 0.5\mu m \times 4.30\mu m$, shows a typical gate dependence in the resistance measurement as expected for a graphene device. The total resistance $R$ includes the resistance from graphene $R_{graphene}$ and the contact resistance $R_{contact}$ at two contact interfaces: that is, $R = R_{graphene} + 2 \times R_{contact}$. The variation of $R$ when the backgate voltage $V_{\mathrm{G}}$ is swept from -35V to +35V in Fig.3.7 shows that the Dirac point $V_{\mathrm{D}}$ (the charge neutrality point) appears at around -0.6 V and that $R$ is significantly higher in the p(hole)-doped region ($V_{\mathrm{G}}$<$V_{\mathrm{D}}$) than in the n(electron)-doped region ($V_{\mathrm{G}}$>$V_{\mathrm{D}}$). In Fig. 3.8(a), where a longer junction ($LxW = 2.5\mu m \times 3.7\mu m$, circled in yellow) from the same graphene flake is measured, we see that $R$ is more symmetric with respect to $V_{\mathrm{D}}$. This asymmetry can be attributed to the doping effect from metallic contact, as we will discuss in 3.4.2, and is more pronounced in a shorter junction than in a longer one, as in the latter the contribution from the bulk of graphene dominates the transport.

Figure 3.7(c) plots the field effect mobility calculated from the gate dependence measurement. The mobility $\mu$ is given by $\sigma = en\mu$ where $\sigma$ is the conductivity (plotted in (b)) and $n$ is the carrier density given by the gate voltage using a simple parallel plate capacitor model $C = \kappa\varepsilon_0 Area/d$. Here, we use $d$= 285 nm, and $\kappa = 3.9$ for the $SiO_2$ substrate in order to estimate the carrier density. The mobility of our devices ranges from 3,000 to 10,0000$cm^2/Vs$.

Using a semiclassical relation between the mobility and the mean free path $en\mu = \frac{2e^2}{h}k_f l$, where the Fermi wave is vector $k_f = \sqrt{\pi n}$, we can estimate the mean free path $l$ at different gate voltages from the measurement[73] (Fig.3.7(d) and Fig. 3.8(d)). At higher carrier density away from the Dirac point, $\mid V_G \mid > 10V$, it os possible to estimate $l$ and $k_f$ because the electron-hole puddles or other types of inhomogeneity are well screened out[33, 89]. In all the devices we measured, $l$ falls in the range of 25 nm ~ 200 nm, much shorter than the respective junction length $L$, thereby indicating that the junctions are diffusive.

#### 3.4.1.2 *Magneto resistance in a high magnetic field*

Figure 3.9 (a) shows the two terminal magneto conductance measured as a function of the magnetic field (B) and the gate voltage in one of the junctions: $LxW$= 0.5 µm x 4.3 µm, ξ = 0.12. The *Landau fan* diagram shows the evolution of the conductance as the magnetic field increases from 0.5 to 8.2 tesla. The two-probe measurement is presented after contact resistance has been subtracted in order to reflect the intrinsic transport properties of the sample. The conductance

---

[3] This is the nominal junction length as defined in the CAD software. The real junction may be shorter due to the over-development we purposely performed to obtain better electrical contact.

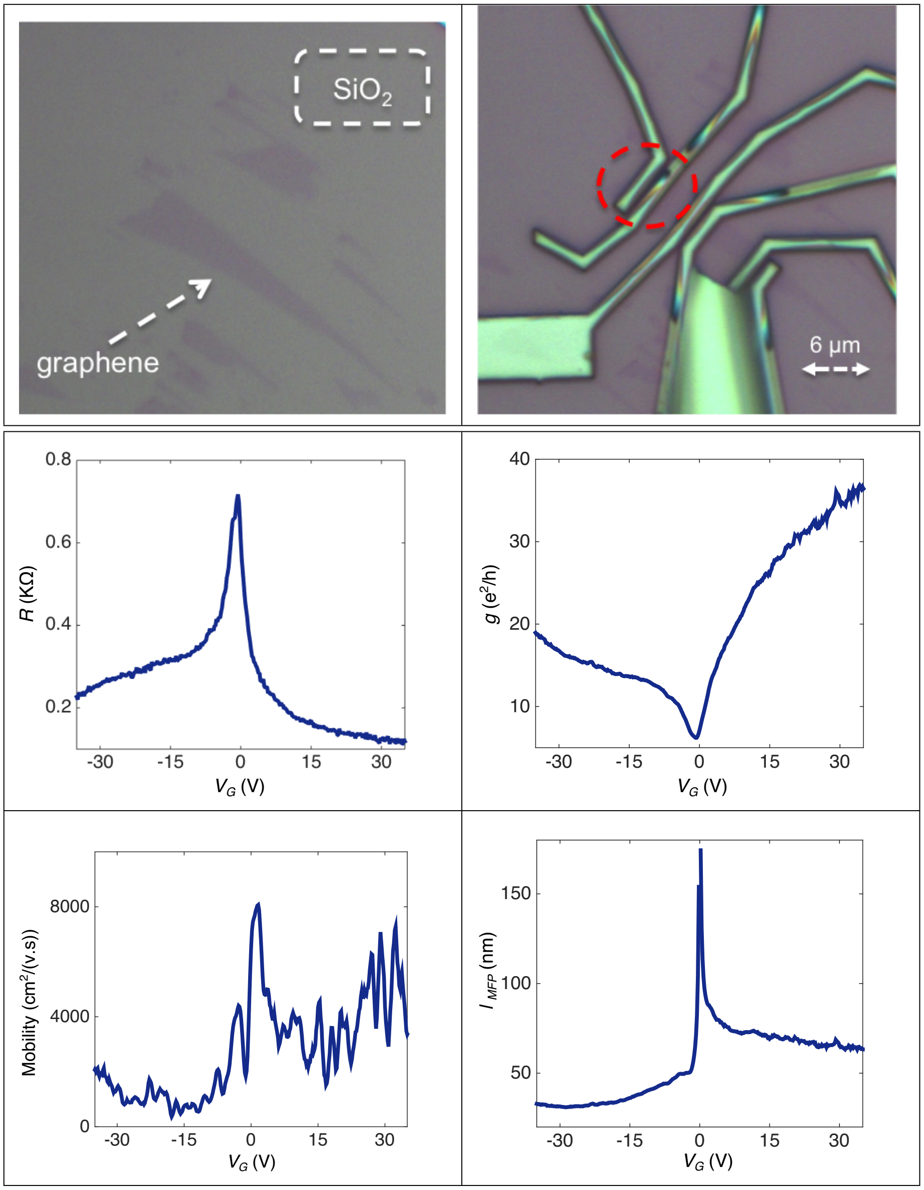

Figure 3.7: Normal state characterization of a short junction (L~500 nm), circled in red. Gate dependence of resistance, conductivity, field effect mobility and carrier mean free path are plotted.

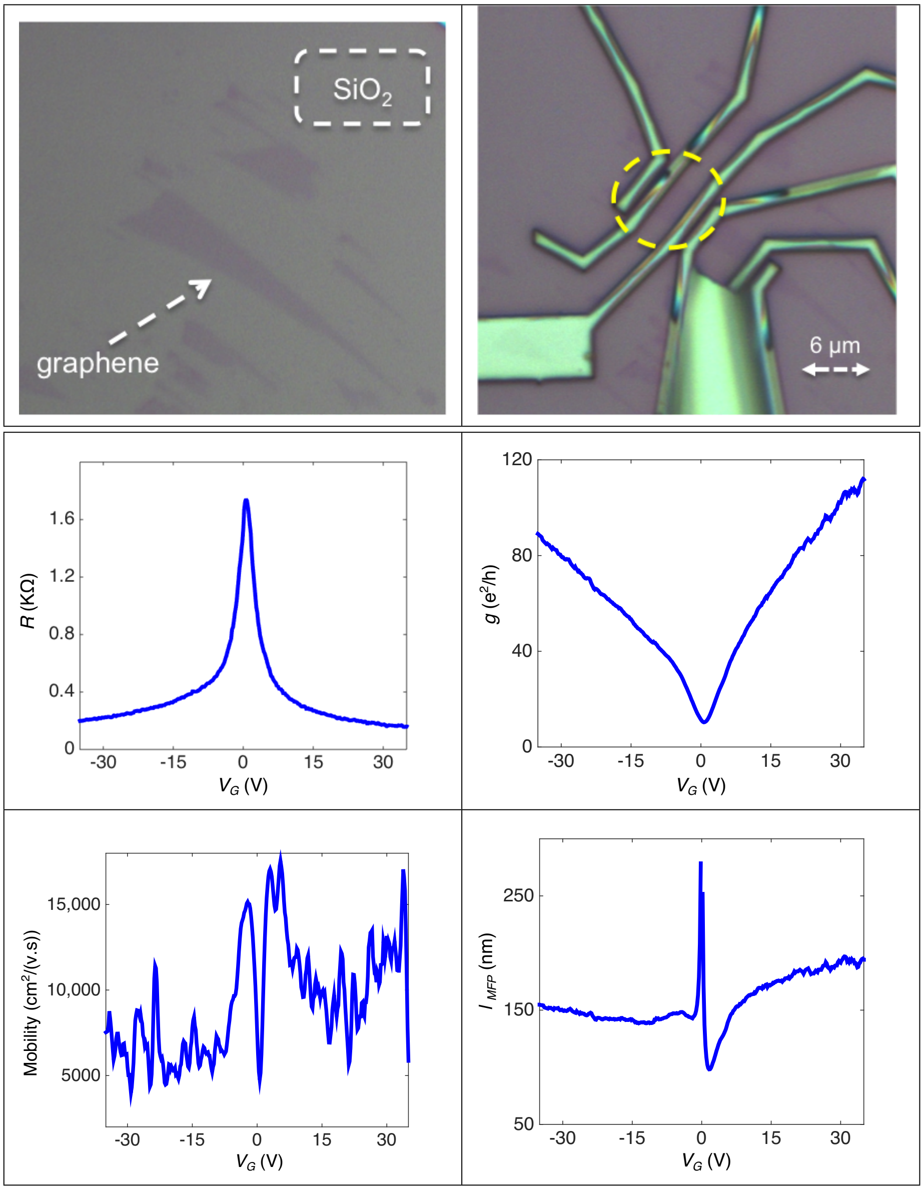

Figure 3.8: Normal state characterization of a long junction ($L = 2.5\mu m$), circled in yellow. Gate dependence of resistance, conductivity, field effect mobility and carrier mean free path are plotted.

quantization becomes more pronounced as the B field increases and pronounced plateaus emerge in both the n-doped and the p-doped region respectively, showing the signature quantum Hall effect in a 2-dimensional system. Due to the mixing of longitudinal and transverse signals in the two-probe QHE measurement, it is not as straightforward to interpret as the multi-probe measurement is. However, the two-probe QHE measurement is still a powerful tool for identifying the number of graphene layers, especially when the size of the device forbids other techniques such as Raman spectroscopy. The quantum Hall plateau measured in a two probe configuration may not be as well quantized as in a multi-probe measurement due to the non-zero longitudinal conductivity of the former. However, it has been demonstrated that for rectangular two-terminal devices with an aspect ratio of $\xi=L/W$ at extremum, that is to say, very wide or very narrow, the quantization can be well-defined and shows characteristics that depend on $\xi$ [131]. In particular, for a wide junction ($\xi<1$), the conductance minima are predicted to appear around the incompressible densities, whereas in a narrow junction ($\xi>1$), it is the maxima that are expected to center around incompressible states[2]. These predictions have been verified in reference [131] with two-terminal devices made with bi-layer and mono-layer graphene.

Figure 3.9(b) plots the conductance measured as a function of gate voltage at 9 tesla. The first two conductance minima away from the charge neutrality point ($V_{CNP}$= -0.6 V) align with $G$=2*$e^2/h$, and 6*$e^2/h$ with a high level of accuracy, corresponding to filling factor $\nu=\pm2,\pm6$ *Landau levels* in monolayer graphene. The conductance minima departs from the expected quantization values as the filling factor increases in both polarity. We also notice that the conductance peaks at the charge neutrality point up to G ~ 15 $e^2/h$. Qualitatively, these features are in good agreement with theoretical predictions and previous results [131, 2]for a wide junction ($\xi$ = 0.12) made with monolayer graphene. The QHE measurement was performed on all the devices, and we confirmed that all the devices discussed in this chapter are made with monolayer graphene.

### 3.4.2 *Josephson effect in NbN-Graphene-NbN junctions*

The NbN leads become superconducting as the fridge cools to below ~ 12K. However the proximity-induced superconductivity in graphene does not show up until the fridge reaches a much lower temperature, typically below 300mK, because (1) the Josephson energy $E_J$in a weak link is smaller than the superconducting gap energy; (2) the electronic temperature of the device deviates significantly from the base temperature of the fridge (~ 25 mK when we performed this experiment): and (3) it takes time, typically 48 hours, to thermalize the device mounted on the cold finger to equilibrium.

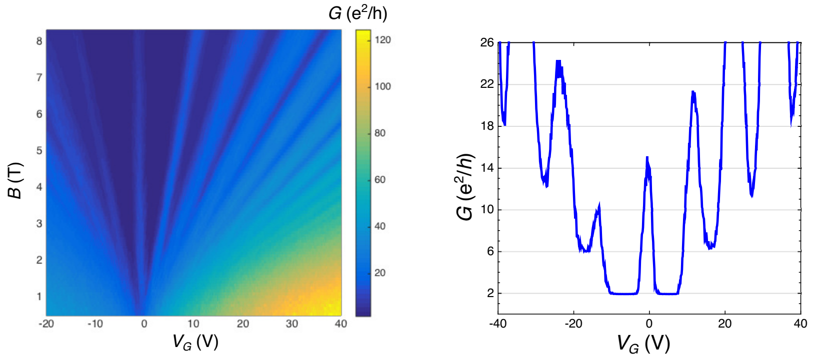

(a) Two-terminal magneto resistance as a function of gate voltage and $B$-field. Showing a typical *Landau fan* diagram

(b) Conductance quantization of a wide, monolayer graphene junction.

Figure 3.9: Two-terminal quantum Hall measurement of a monolayer graphene device

The Josephson effect is measured in a current-bias configuration either with a pure *DC* measurement or with the standard *AC+DC* differential measurement with a lock-in amplifier. Figure 3.10 (a) plots a typical low-bias current-voltage ($I$-$V$) characteristic of one junction measured at various gate voltages. Each plot has a finite current range with a zero voltage drop across the junction, meaning that the current is flowing without resistance, a signature of dissipationless Josephson current. The beginning and end of the zero voltage current defines the maximum Josephson current $I_C$, also called switching current in transport measurement, in each trace. In the framework of the RCSJ (resistively and capacitively shunted junction) model, the gauge-invariant phase difference of a Josephson junction is analogous to a particle confined in a so called "tilted washboard" potential [120]. In light of this model, $I_C$ is the maximum dissipationless current that the junction can support before the particle escapes from the local potential minimum. At finite temperature, $I_C$ is subject to the junction geometry and the actual electromagnetic environment in which the device is operated. Therefore, at finite temperature, $I_C$ is typically much smaller than the *intrinsic critical supercurrent* $I_0$of a weak link. In fact, only $I_C$ unlike $I_0$can be measured easily in transport measurements of SNS junctions [4]. As it is proportional to $I_0$, $I_C$ still offers very rich information about the electronic properties of the device in the superconducting regime. The value of $I_C$ demonstrates strong dependence on carrier density. This dependence is more clearly seen in Figure 3.10 (b), given that the gate-dependent critical current $I_C$ can be read from the boundary of the dark blue region, in which the differential resistance $dV/dI$ is essentially zero. In this junction , $I_C$ ranges from ~67 nA ($V_G$=$V_{CNP}$= -4V ) to ~1000 nA ($V_G$= 40 V). The gate dependence of the

---

[4] We will use $I_C$ to denote the maximum supercurrent that we measure in transport measurement.

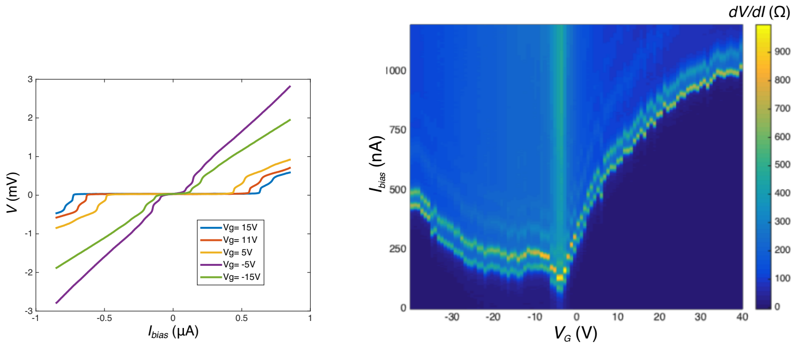

(a) $I$-$V$ characteristics of NbN-G-NbN junctions at different gate voltages.

(b) Differential resistance $dV/dI$ plotted as a function of $V_G$ and $I_{bias.}$ Graphene is superconducting in the dark blue region where $dV/dI = 0$. $I_C$ shows a pronounced dependence on carrier density, and is larger in $n$-doped region at same carrier density. Note that the critical current is nonzero at the charge neutrality point.

Figure 3.10: Josephson effect in graphene as a function of gate voltages.

critical current can be qualitatively understood in terms of the population of Andreev bound states, of which the highest energy must be smaller than the chemical potential.

The measurement shows pronounced asymmetry in both the normal and the superconducting state. For all the junctions we measured, charge neutrality points (the Dirac point $V_D$) appear at negative gate voltages ($V_D < 0$), suggesting that the graphene flake is subject to electron- or n-type doping, presumably from the contacting metals or the $SiO_2$substrate. First principle calculations based on density function theory (DFT) have shown that contact doping in graphene originates mainly from the difference in the work functions between graphene and the contacting metal. Depending on the type of metal and its distance from the graphene surface, this doping can shift the Fermi energy of neutral (not gated) graphene by as much as few hundred meV [63, 79]. Doping by metals becomes even more important in regard to tunneling spectroscopy, as this technique (discussed in Chapter 5) measures directly the doped region. As can be seen in Fig. 3.7, the resistance measured in the p-doped region ($V_G< V_D$) is larger than its counter part (same carrier density but with opposite charge) in the n-doped ($V_G< V_D$) region. We attribute this to *P*-*N* junctions formed at the interface between the differently doped regions. Assume that the graphene underneath the contact is always n-doped, then an *N*-*P*-*N* profile would form between contact and contact when $V_G< V_D$ , as the graphene in between is p-doped (Fig.3.11). However, in the $V_G> V_D$ regime, the device becomes an *N*-*N*′-*N* junction. The potential barrier across the *P*-*N* interface essentially reduces the coupling strength between the graphene and the superconductor,

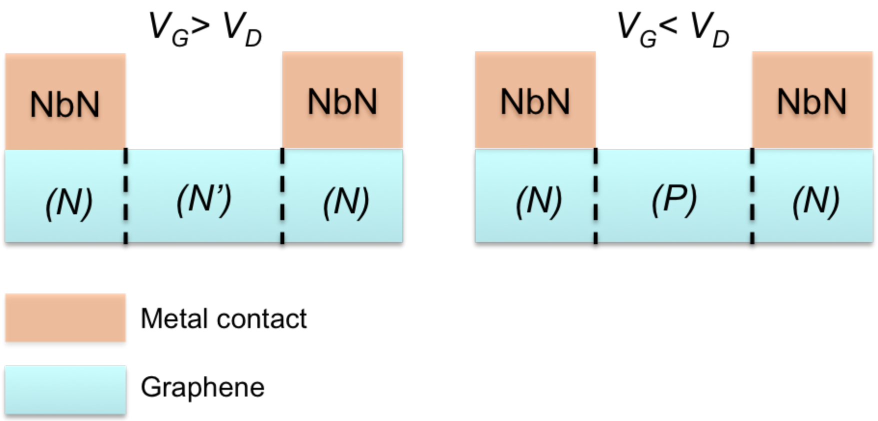

Figure 3.11: *P-N* junction created by contact doping in graphene

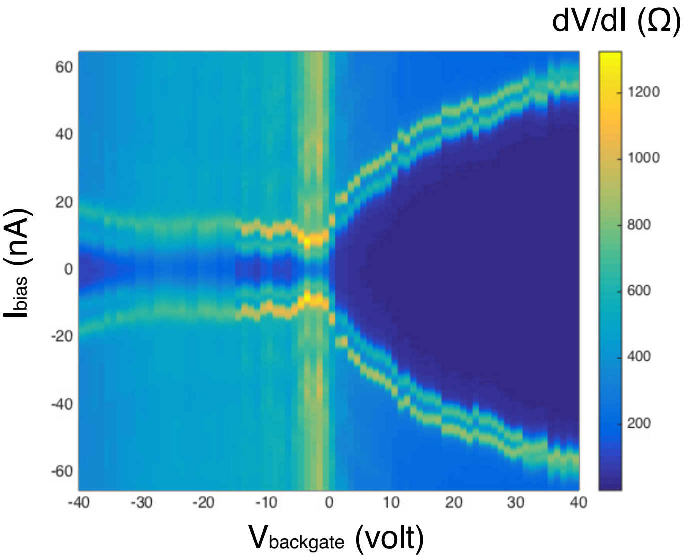

Figure 3.12: Gate dependence of $I_C$ in another device

which may diminish supercurrent charge carriers and/or weaken the induced superconducting gap in the graphene. However, it is difficult to discern the exact mechanism on the basis of transport measurement, as the critical current being measured results from the integration over all possible channels. We will return to this subject in Chapter 5 in which we discuss the tunneling spectroscopy of induced superconductivity in graphene.

We can investigate the NbN-Graphene-NbN junction further by applying a perpendicular magnetic field. Figure 3.13 plots the differential resistance $dV/dI$ measured as a function of magnetic field $(B)$ and bias current $I_{Bias}$ in a junction with $L \times W = 0.5 \times 2\mu m^2$. It is immediately evident that the critical current, defined by the boundary of zero $dV/dI$ region, oscillates and damps out as $B$ increases. As discussed in chapter 2 (2.2.2.1), what is known as the *Fraunhofer* pattern of the

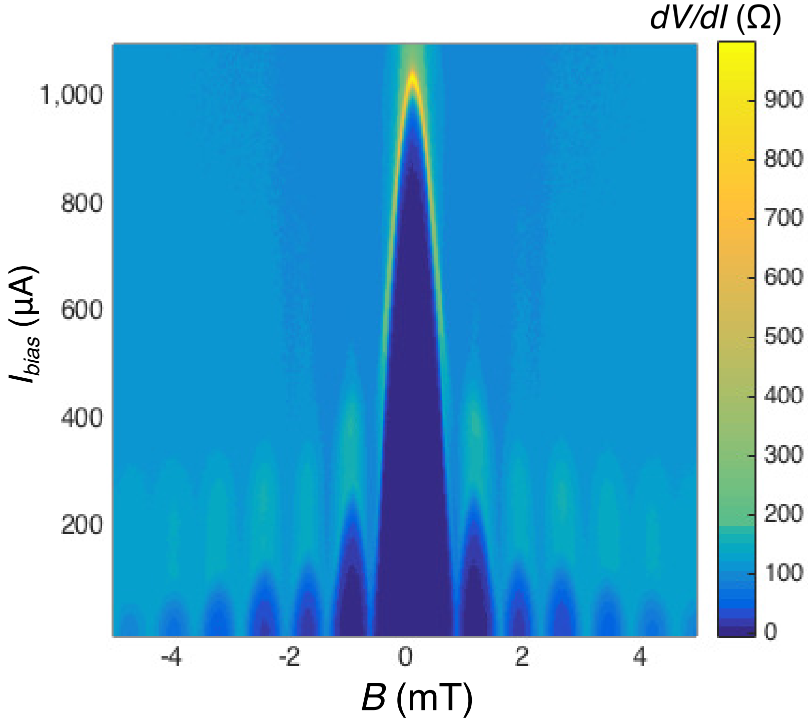

Figure 3.13: *Fraunhofer* oscillation of $I_C$ as a function of magnetic field at $V_G = 40V$. In a Josephson junction *Fraunhofer* oscillation of $I_C$ is the Fourier transformation of supercurrent distribution along the transverse axis. This pattern is indicative of a uniform distribution of supercurrent in our graphene device

critical current in an extended Josephson junction results from the gradient (in the direction parallel to the leads, or for example, across width w) of phase difference between the macroscopic BCS order parameter in two superconducting banks[120]. The *Fraunhofer* pattern shown in Figure 3.13 is indicative of a uniform supercurrent spatial distribution in a rectangular junction[5, 70].

In general, the flux in the SNS junction is given by $\Phi = A_{effective} \times B$, where $A_{effective} = (L + 2\lambda) \times W$ and $\lambda$ is the London penetration depth of the superconductor[120]. $\lambda$ extracted from our measurement is ~ 450 nm, in reasonable agreement with previous results that measure $\lambda(0) = 200nm \sim 700nm$ in epitaxially grown NbN thin films[82, 98, 76] [5]. On the other hand, field crowding, i.e., extra magnetic field in the junction that is expelled from the superconducting lead due to diamagnetism ( the Meissner-Ochsenfeld effect), can also

---

[5] Empirically, $\lambda(0)$ of NbN thin film varies significantly with the fabrication methods, thickness, and sample geometry. This $\lambda(0)$ decreases with film thickness, and is found to be larger in lower-quality film. Using DC magnetron sputtering, an ultra high vacuum chamber, and elevated substrate temperature (up to 800 °C) significantly reduces the measured $\lambda(0)$. We did prepare our NbN film in a system with such capability. However, we were forced to sputter the film at room or mildly elevated temperature (~50 °C) due to the presence of PMMA.

contribute to the total magnetic flux threading into the junction, causing a departure from expected periodicity. In Chapter 4 and 5, we will see that this effect takes on great importance in the device proximitized by aluminum contacts, whose *London* penetration depth $\lambda$ is in general much smaller than that of NbN. As the NbN used in the current experiment was not characterized explicitly, it is hard to quantify the contributions from the respective causes [6].

Finally, Figure 3.14shows the *dV/dI* measurements (in a flake different from the one in Fig. 3.13) with an applied B-field of up to 66 mT. The proximity effect in graphene is suppressed monotonously and disappears after 4 lobes of oscillations. We also see that at a field beyond ~ 5mT, the differential resistance increases as the bias current approaches zero (Fig. 3.14(a) inset, and (c)), which is indicative of pronounced suppression of the Andreev reflection at the superconductor/graphene interface.

---

[6] From the perspective of estimating the effective magnetic flux in the device, both mechanisms yield the same number, as in practice we would take half the width of lead $w_{lead}$ from both sides so that $A_{effective} = (L + W_{lead}) \times W_{graphene}$.

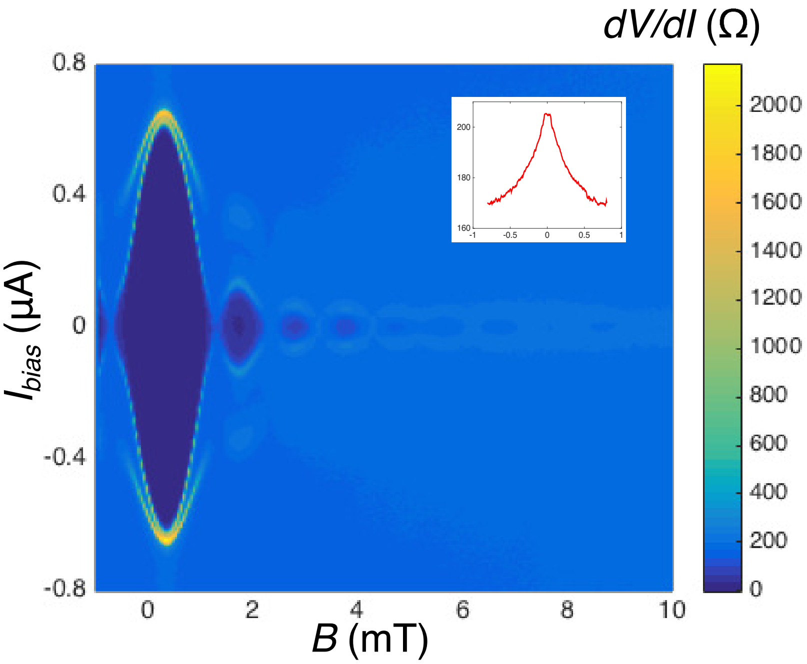

(a) Decrease of $I_C$ as the perpendicular B-field increases

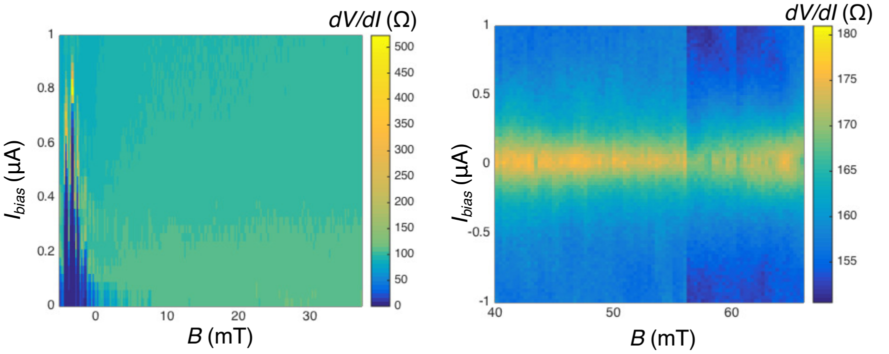

(b) Decrease of $I_C$ as the perpendicular B-field increases (larger field)

(c) Evident increase of $dV/dI$ at zero bias as the field increases further, showing strong suppression of Andreev reflections

Figure 3.14: $I_C$ measurement at higher field up to 80 mT. At B>5mT, zero-bias $dV/dI$ starts to become larger than finite-bias $dV/dI$, meaning that Andreev reflections are strongly suppressed

## 3.5 DISCUSSION

We have shown that graphene can be contacted by Ti/NbN by direct reactive sputtering at room temperature. The Josephson current was measured in all the short junctions ($L$ = 500nm) and the critical current reached a few micro ampere at a high carrier density. Compared to graphene Josephson junctions with aluminum leads ($T_C$~ 1.1 K) and similar dimensions (Chapter 4), the critical current of the NbN device is about one order of magnitude larger, indicative of a larger gap corresponding to $T_C \sim 12$K. From the field effect variance of conductivity, we infer the mean free path in each junction, and determine that $l_{mfp}$ is much smaller than the junction length $L$, suggesting that the devices are all in a diffusive transport regime. Given the dimension of our device, the Josephson effect is strongly suppressed when the perpendicular magnetic field is at a few mT. Beyond the disappearance of the Josephson effect, the junction becomes more resistive at zero bias than in the finite bias regime, which is indicative of strong depression of the Andreev reflection at the interface. In particular, we do not see in our data any enhancement of conductance at high magnetic field around the onset of the quantum Hall effect in our devices. This is in contrast to the finding in reference [103], which shows that in a Nb-contacted graphene device on $SiO_2$, the conductance enhances with respect to the expected value at certain quantum Hall plateau, at a magnetic field below the higher critical of $Nb$.

The results from this experiment suggest that although NbN contact provides a superconducting gap about 10 times larger than that of the commonly used aluminum, there is a significant drawback to building graphene devices on an $SiO_2$ substrate. That is, the process incorporates a high level of inhomogeneity, which renders the device unsuitable both for investigations that rely on ballistic transport properties[121, 69] and for studying the physics involved at a lower energy scale[13].

# 4

# SUPERCURRENT TRANSPORT IN DUAL-GATED, BALLISTIC GRAPHENE DEVICES

In Chapter 3, we demonstrated that although it is possible to proximitize graphene with large-gap, type II superconductors such as *NbN*, the transport properties of these devices are still in the diffusive regime. That is, the carrier will go through multiple scattering events before completing the transport ($l \ll L$,where $l$ is the mean free path and $L$ is the distance from lead to lead[37]). From the perspective of electronic transport, this means that a charge carrier sees a spatial variation of electrostatic potential that would scatter with the particle and deflect it from its ballistic trajectory. In order to realize some of the exciting theoretical prediction made for relativistic superconductivity[14], namely, the superconductivity carried by Dirac fermions, another ingredient is required: a graphene sample with low disorder.

The road to the promised *carbon flatland*[57, 96], however, remains bumpy and full of obstacles. It is the purpose of this chapter to demonstrate how we can realize ballistic transport in graphene by fabrication techniques that we have developed. In particular, ballistic transport of charge carriers in both normal and superconducting regimes are presented in this chapter.

## 4.1 GRAPHENE DEVICES WITH LOW DISORDER

The spatial variation of potential in $SiO_2$-supported graphene arises from several sources, including geometrical corrugation, strain, surface adatoms, and electrical or chemical doping. At low carrier density, in particular, the charge distribution breaks up into puddles of electrons or holes[89], which gives rise to scattering at the nanometer scale. Yet, the same experiment[89] also demonstrated that the density fluctuation may not primarily comes from the trapped ions in the oxide layer of the substrate. High resolution non contact atomic force microscopy (NC-AFM) shows that graphene conforms to the surface corrugation of the $SiO_2$, whose root-mean-square roughness (RMS) is typically 0.37 nm, down to 99% fidelity (RMS roughness of supported graphene ~0.35 nm)[34]. This means that the charge carrier traveling in graphene does not necessarily encounter an atomically flat surface but a rather uneven landscape where scattering events can take place. Finally, without post-fabrication treatment like forming gas annealing or Joule heating in vacuum, acrylic resists (PMMA) and other solvents used in nanofabrication inevitably leaves residue on the surface of the graphene flake (Fig.**??**(a)), particularly in the bulk region where the transport takes place. The residue inevitably causes structural inhomogeneity or chemical doping. These constituents and associated processes all contribute to the disorder in graphene that prohibits the ballistic transport , and thus the low-excitation physics as a research focus. It is, therefore, evident that a better substrate, or no substrate at all, is required.

The first attempt to reduce the disorder in graphene caused by the influence of substrate is to suspend the device. This suspension was first achieved by etching a thin layer of $SiO_2$ from substrate by using hydrofluoric acid (HF) and drying in a critical point dryer[19]. The suspension was also achieved later using polymer-based schemes[93, 122]. The mobility $\mu$ of this ultra-flat, ultra-clean (after Joule heating) graphene can exceed 100,000 $cm^2/Vs$ or 1,000,000 $cm^2/Vs$ at room or liquid helium temperature, respectively[48, 19, 26].

The improvement in device quality has, indeed, afforded the possibility of accessing the theoretical limits of graphene's intrinsic properties. Additinally, the improvement has led to the observation of fascinating physical phenomena, such as the fractional quantum Hall effect, ballistic transport of charge carriers, and broken-symmetry states in single or bi-layer graphene[48, 20, 53]. Yet, the complexity of the fabrication procedures and the fragility of the suspended structure significantly limits the production yield and the dimensions of the devices (usually in a 2-probe configuration).

Another approach to obtaining high-quality graphene device by reducing substrate-induced disorder is to use ultra-flat, ultra-clean insulating substrates[88, 40]. This is the strategy we are pursuing as discussed in detail in the following sections.

## 4.2 INTRODUCTION TO HEXAGONAL BORON NITRIDE (H-BN)

Hexagonal boron nitride (h-BN) is the material we used as an atomically flat and pristine substrate, a gate dielectric, an encapsulating over-layer, and a tunneling barrier for high-quality graphene devices for transport and spectroscopy experiments. The method, proposed and pioneered by Philip Kim's group at Columbia University (now at Harvard University), has become one of the most prominent fabrication schemes for graphene research. Since its introduction to graphene research in 2010[40], layered h-BN crystal has been used to contribute numerous tremendous results to the field[41, 118, 134, 72, 42, 102, 119, 81, 7]. In addition, layered hBN crystal has opened up several new directions in the physical sciences, including a brand new branch referred to as two dimensional Van-der-Waals heterostructures[55], a category of mesoscopic devices to which the samples presented in this study from this point on belong. We will discuss the latter in greater detail in 4.3.2 after the describing the fabrication techniques.

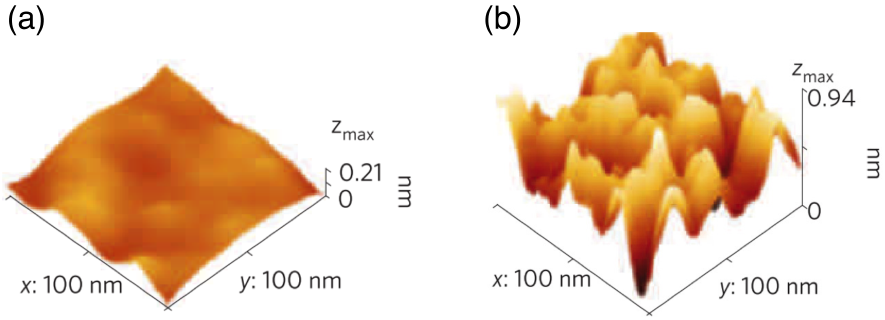

Figure 4.1: STM topography images of monolayer graphene on different substrates in a 100nm by 100nm area. (a) graphene on h-BN substrate, roughness ~30 pm, and (b) graphene on $SiO_2$ substrate, roughness ~ 220 pm. Images adapted from Ref.[133]

A number of methods have been developed to improve the process and the device quality thus rendered. Here we present only the method that we used for the devices discussed in this chapter followed by a more generalized version of the fabrication technique we used for a wide variety of samples. References [40, 118, 127, 137]offer a good overview for other techniques commonly used to integrate h-BN into graphene device fabrication.

### 4.2.1 *Basic properties of h-BN*

h-BN is an insulating, layered material that consists of nitrogen and boron atoms. An isomorph of graphite, h-BN's Bernal A and B sublattices are occupied by nitrogen and boron atoms respectively. The atomically flat surface oh h-BN and its slight (1.7%) lattice mismatch with graphite [64]makes it an ideal substrate for graphene, as the rippling in the flake due to surface corrugation can be significantly suppressed (Fig.4.1). Strong in-plane ionic bonding makes the h-BN surface relatively inert and free of dangling bond or trapped charges. These properties are all favorable for reducing doping or disorder in graphene, which can originate from various sources.

Electronically, h-BN is an insulator with a large direct bandgap (5.9 eV), relative permittivity ~ 3.9 ($\varepsilon \sim 3.9\varepsilon_0$), and breakdown voltage $V_{breakdonw} \sim 0.7V\mathrm{nm}^{-1}$ [129, 40], which makes it an appropriate substitute for $SiO_2$ ($\varepsilon = 3.4\varepsilon_0$) as a gate dielectric. As an insulating, single-crystal atomic sheet with a low defect density, h-BN can when reduced to a few atomic layers can serve as a tunneling barrier for mesoscopic devices ( [6, 23, 86, 22, 28]and Chapter 5).

Table 4.1 summarizes these parameters of h-BN as compared to $SiO_2$ and graphene. Note that all the h-BN crystals used in the experiments presented in this thesis are provided by the authors of reference [129].

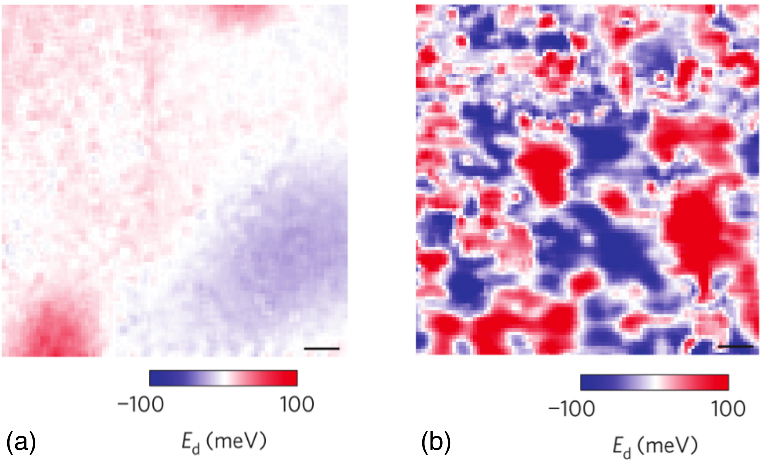

Figure 4.2: Spatial variation of density of states in monolayer graphene on different substrates revealed by STM [133]. (a) Tip voltage at Dirac point of monolayer graphene on hBN substrate as a function of position (b) Tip voltage at Dirac point of monolayer graphene on $SiO_2$ substrate as a function of position. Images adapted from Ref. [133]

| Material | bandgap | dielectric constant | lattice constant | structure |
|---|---|---|---|---|
| h-BN | 5.9 eV | 3-4 ($\varepsilon_0$) | 2.50Å | layered crystal |
| Graphene | gapless | 1.8*($\varepsilon_0$) | 2.46Å | layered crystal |
| $SiO_2$ | 9.3 eV | 3.9($\varepsilon_0$) | amorphous | amorphous |

(*in-plane[109])

Table 4.1: Comparting h-BN, graphene, and $SiO_2$

### 4.2.2 *h-BN for superconducting graphene devices: advantages and technical challenges*

Although h-BN is used a an remarkable substrate for non-superconducting graphene devices, extra caution must be taken when using h-BN for *SGS* samples. In fact, if h-BN is used only as a substrate, post fabrication (resist lift-off ) treatment is required to remove the polymeric residue left by the the e-beam or photolithography resists. The treatment typically involved with thermal annealing in forming gas or Joule heating in the cryostat [1], both reach temperatures of up to a few hundred degrees Celsius locally. Figure 4.3 shows the NbN-contacted SGS devices built on a h-BN substrate employing the fabrication method described in references [118, 119]. Without any annealing, the device exhibited the Josephson effect at a low temperature, as expected. However, the transport properties such as mobility did not appear to be any better than those of the devices on $SiO_2$ presented in Chapter 3.

On the other hand, a high-temperature environment may lead to a degradation of the graphene/metal interface for the superconducting devices discussed herein. Empirically, we found that after either kind of annealing, the contact resistance $R_C$ increased, the zero bias $dV/dI$ became greater than at finite bias, and the Josephson effect could no longer be measured, all of which suggest that Andreev reflection at the interface is strongly suppressed, even though the devices's mobility did improve significantly [2]. We ascribe the degradation of the contact quality to two possible causes: the oxidation of metallic contacts (assuming the existence of residual $O_2$ during annealing process), and the breakage of the graphene sheet under those contacts due to differing thermal expansion coefficients of graphene, which is negative[135], and the adhesion metal (we used *Ti* for superconducting devices and *Cr* for normal contacts). Note that the increase in $R_C$ may be more tolerable for devices intended for the quantum Hall regime, high-impedance measurement or in a four probe configuration in which the $R_C$ can be explicitly extracted. In addition, for devices with normal contact, the *Cr* adhesion layer is deposited with less than 1 nm to reduce the extent to which the graphene breaks due to the thermal expansion effect. On the other hand, for the superconducting contact on graphene, it is necessary to deposit a few nanometers of *Ti* to lower $R_C$ and achieve a highly-transparent interface[103, 92].

---

[1] Chemical treatments in a variety of solvents have been reported, see for example [32]. In our lab, we have tried cleaning the PMMA-contaminated graphene in chloroform and trichloroethylene (TCE), yet neither of these approaches is as effective as high temperature annealing.

[2] We are aware that the *SG*- or *SGS* devices reported in [49, 93, 5] and the bi-layer device in [4] did exhibit the proximity effect after undergoing current annealing (Joule heating). It is, therefore, possible to current anneal and maintain the contact quality in the *SGS* junctions simultaneously.

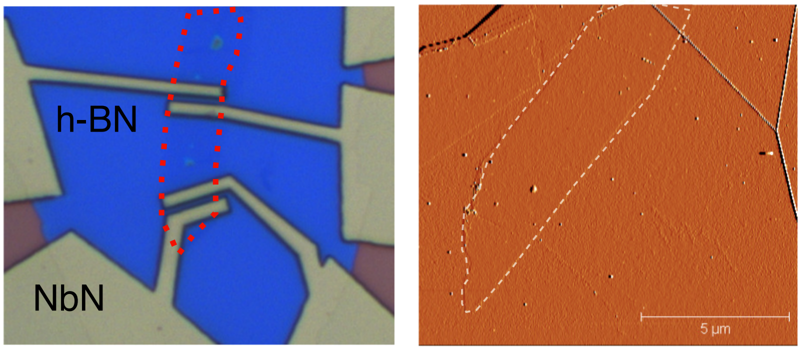

(a) Optical image of *NbN-Graphene-NbN* junctions on h-BN substrate (the blue background). Red dashed line depicts the graphene area.

(b) AFM micrograph (amplitude signal) of graphene (enclosed by dashed line) on a h-BN substrate

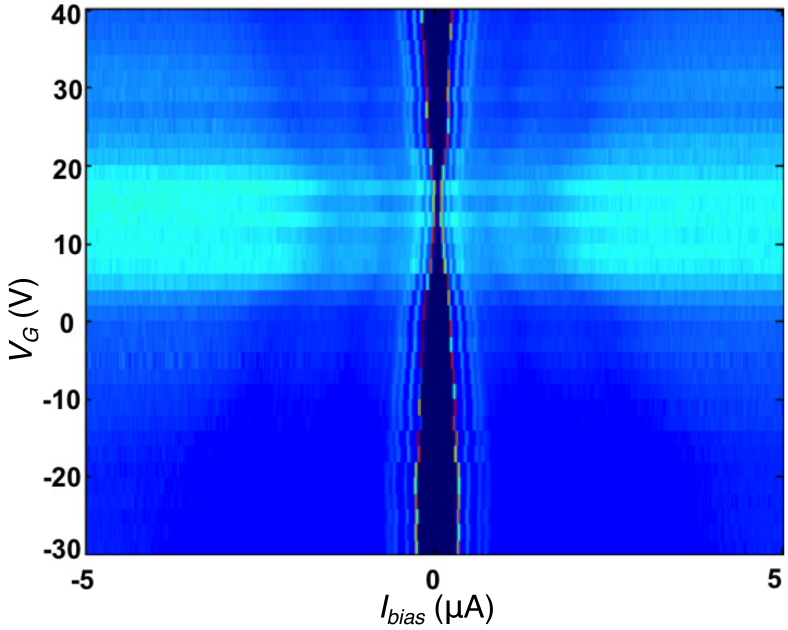

(c) $dV/dI$ plotted as a function of backgate $V_G$ and bias current $I_{bias}$. Superconducting state is exhibited in the dark blue region where $dV/dI = 0$

Figure 4.3: *NbN-Graphene-NbN* devices on h-BN substrate. The device shows typical behaviors in superconducting regime, as discussed in chapter 3, but without thermal annealing, it does not exhibit significant improvements in terms of mobility.

## 4.3 PICK-UP AND TRANSFER METHOD FOR MAKING ENCAPSULATED GRAPHENE DEVICES

Given the limitations on making superconducting graphene nanodevices on an h-BN substrate, as discussed in section 4.2.2, particularly when an open surface method is used, we decided to encapsulate the entire device in h-BN. In principle, the h-BN protects the top and bottom of the graphene, so that the pristine graphene flake is not susceptible to the ambient environment or contamination during the nanofabrication process. When we started to tackle this issue, a h-BN encapsulated graphene device in Hall bar geometry had been reported and showed micrometer-scale ballistic transport behavior at room temperature [91], which is very encouraging.

Encapsulation with h-BN is a promising technique for obtaining pristine graphene device without annealing. However, applying this technique to superconducting devices, particularly the Josephson junction, is far from straightforward. The proximity effect requires a small encapsulated region (characterized by the ballistic coherence length $\hbar v_f / \triangle_{sc}$where $v_f$ is the Fermi velocity of the normal metal and $\Delta_{sc}$ the superconducting gap energy) and rectangular geometry (for a regular Josephson junction), both of which make it difficult to use exfoliated h-BN on top of the flake as in reference [91].

### 4.3.1 *A polymer-based dry pick -up and transfer technique for Van-der-Waals materials*

As in the case of graphene, weak Van-der-Waals bonding between layers allows a thin h-BN flake to be obtained by mechanical exfoliation from pure crystal [3]. Our strategy for encapsulating graphene is to cover the graphene on a h-BN substrate with a patterned h-BN mask. The key to this fabrication is a method for picking-up and transfer the pre-patterned h-BN mask onto a designated location with micrometer scale precision.

We exploit the temperature dependence and thus the selectivity of the adhesion power rendered by the polymers that we used for h-BN transfer [118]. To pick up a flake from the $SiO_2$ substrate with the polymer, the adhesion between the polymer and the h-BN must be stronger than either polymer-to-$SiO_2$ or h-BN-to-$SiO_2$ adhesion. Although the adhesive power of the polymer increases monotonously as the temperature increases, we found that for PMMA, the 85~100°C temperature window offers the desired selectivity for picking up the h-BN flake. At temperatures above 135°C, PMMA starts to re-flow

---

[3] Empirically, h-BN seems to be more brittle and less ductile than graphene. When larger flakes (a few tens of micron in lateral dimensions) are desired, we would use less sticky tape than the one we use for graphene.

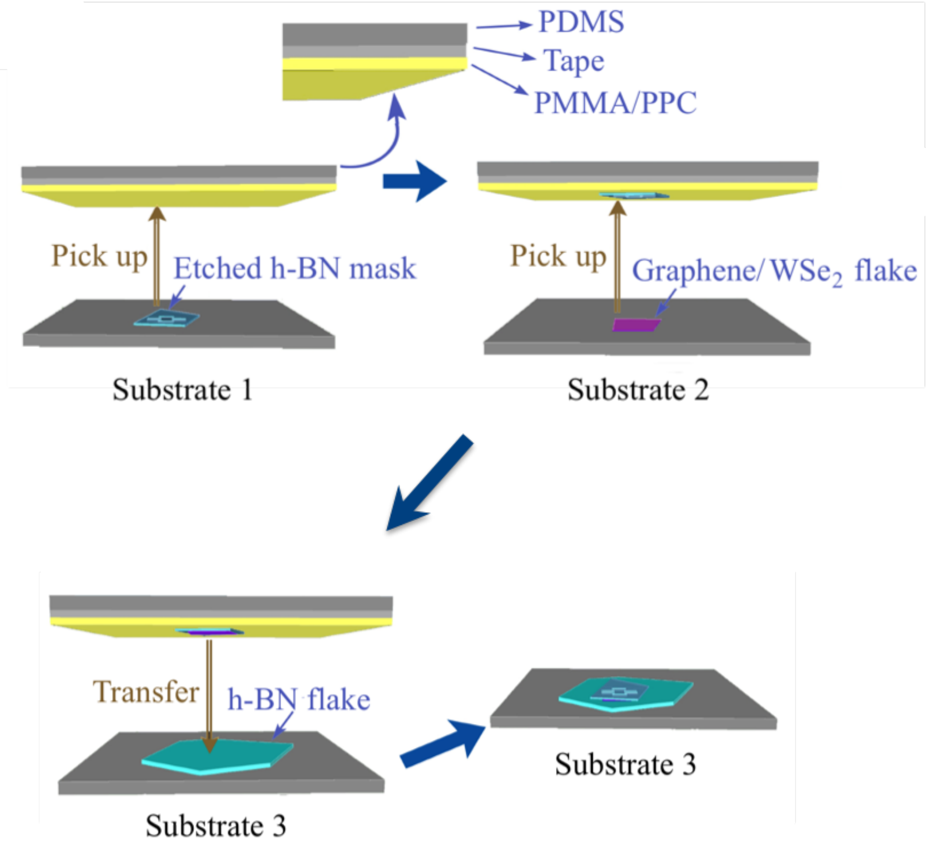

Figure 4.4: Schematic of polymer-based dry pick-up and transfer technique for Van-der-Waals materials

and sticks to the substrate very easily, which facilitates the transfer of the picked-up flake.

Figure 4.4 illustrates a generalized, step-by-step pick-up and transfer process[126]. A polymer stack consisting of PDMS (polydimethylsiloxane), clear tape, and sticking polymer ( PMMA or PPC(polypropylene carbonate) ) is mounted on a glass slide, through which the stack can be aligned with any target on the substrate with a long working distance microscope of the transfer setup (see 4.3.3). To pick the h-BN mask, the polymer stack is brought into contact with the h-BN and heated to ~100°C for 5 minutes. The polymer stack then disengages from the substrate by either an abrupt separation at 100°C (if using PMMA) or a gentle lift-off as the temperature decreases (if using PPC), whereas the h-BN will come off with the polymer. With more robust polymer like PPC or PC (polycarbonat), this step can be repeated several times until a desired heterostructure is obtained. Finally, the heterostructure is transferred onto the bottom part of the final device, which can be a h-BN substrate, a backgate electrode, or pre-deposited leads, and eventually heated to above 130°C in order to release the sticking polymer. After the polymer has been dissolved

| Polymer | Use/materials | P temp. | T temp. | Disengage |
|---|---|---|---|---|
| PMMA | single P&T/hBN | 85~100°C | >140°C | abrupt |
| PC | multi-P&T/graphene, hBN≥1L | 60~100°C | >150°C | smooth |
| | ,graphite nano rods, TMD | | | |
| PPC | multi-P & T/hBN, TMD | 30~ 100°C | >70°C | smooth |
| MMA | T/graphene, hBN, TMD | N/A | >130°C | N/A |

P: pick-up
T: transfer
PMMA: 950A5 (5% in anisole)
PC: polycarbonate (6% in chloroform)
PPC: polypropylene carbonate (15% in anisole)
MMA: EL-6 (6% in Ethyl Lactate)
TMD: transition metal dichalcogenide

Table 4.2: Sticking polymers used in pick-up and transfer process

in solvent, the heterostructure is ready for subsequent steps of the nanofabrication.

The choice of sticking polymer and related processing parameters varies a lot with the target materials. Table 4.2 summarizes some of the parameters used for different polymers in our lab at the time this dissertation was being composed.

### 4.3.2 *Van-der-Waals heterostructures*

The polymer-based pick-up and transfer technique applies not only to h-BN masks but also to a much wider variety of 2-D Van-der-Waals materials, including semi-metal, semiconductor, topologic insulator, and superconductor[55, 49, 126]. In addition, one-dimensional edge contact [127] has propelled advances in the fabrication of heterostructures consisting of several atomic layers of 2-D materials made in an ambient environment. In particular, fully encapsulated SGS junctions contacted by type-II superconductors at a one-dimensional edge have also been reported as showing ballistic transport behavior at low temperatures[24, 113].

### 4.3.3 *Transfer setup*

Figure 4.5 shows the home-built transfer setup used for the pick-up and transfer process. The whole setup is installed on a vibration isolation table sitting on a heavy, sturdy foundation (Fig.4.5(a)). The sample is vacuum-mounted on an aluminum block that can be heated to 200°C (Fig.4.5(c)). A glass slide mounted to a 3-axis micromanipulator stage allows alignment of the material on polymer stack with features on the chip with a micrometer-scale precision (Fig.4.5(e)).

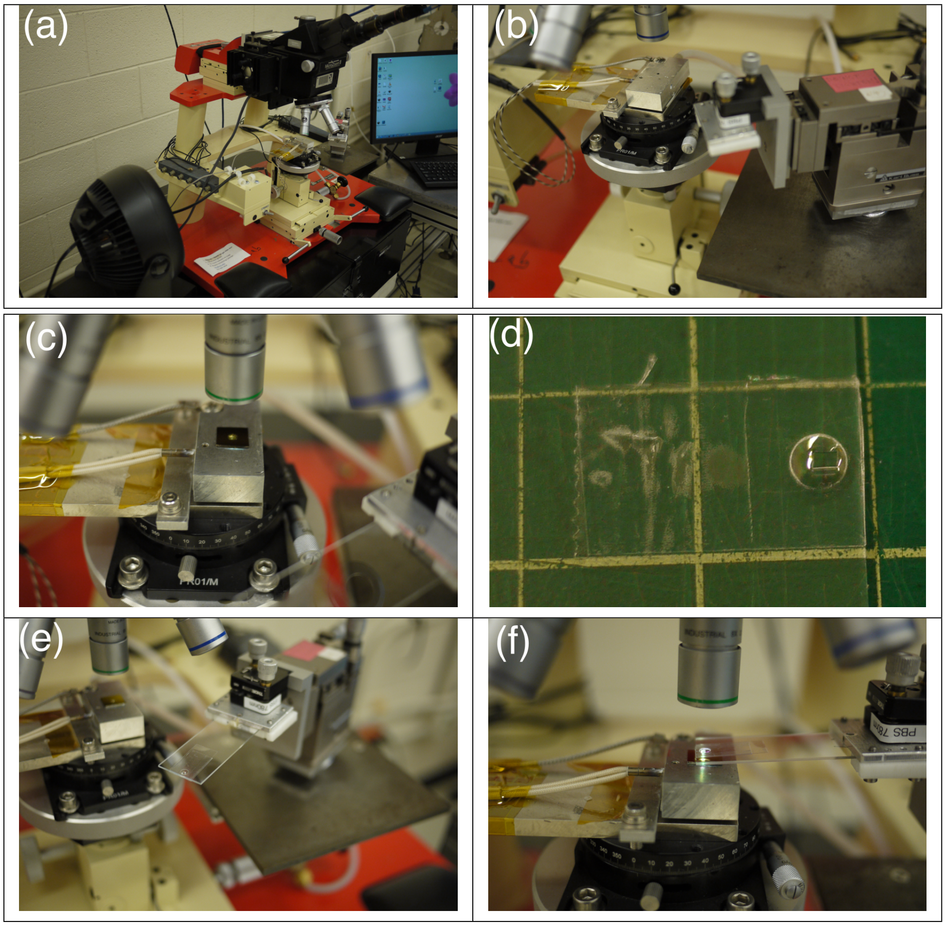

Figure 4.5: A home-built transfer setup in Jarillo-Herrero Lab. (a) Transfer setup. (b) Sample holder and microomanipulator for alignment. (c) Vacuum-mounted sample on a heated stage. (d) Polymer stack on a glass slide for picking-up flakes. (e) Polymer stack-/Glass slide mounted to the micro-manipulator (f) Engaging the polymer to substrate.

A microscope with a long working distance is attached to a CCD camera in order to observe the process on a monitor and minimize vibrations caused by manual manipulation (Fig.4.5 (a) (f)).

## 4.4 DUAL-GATED GRAPHENE JOSEPHSON JUNCTIONS IN BALLISTIC REGIME

Fully encapsulated graphene provides an ideal system for studying the ballistic transport in both the normal and the superconducting regimes. The h-BN-graphene-hBN heterostructure thus made allows electrostatic gating from both sides of the graphene and a combination of global amd local gating is possible. Owing to the gapless bandstructure and the chirality of Dirac fermions in graphene, an alternating texture of polarity, namely P-N or P-N-P(N-P-N) junctions with high transmission probability given by Klein tunneling[130, 100, 136, 68, 105], can be realized in nanoelectronics. In particular, the P-N interface in graphene can be highly transparent for charge carriers, while their trajectories could resemble that of refracted light at the interface of metamaterials with negative refractive index[29].

Thus, the combination of a ballistic device with electromagnetic field control of the charge carrier together with the quantum confinement thereby provided, also opens up an exciting field of electron-optics in solid state systems[29, 136, 25, 119, 105, 68] which, by analogy between optics and mesoscopic quantum transport of electrons, offers novel ways to manipulate electronic systems.

Klein tunneling in graphene is also of interest in the context of superconductivity. The Andreev reflection at the superconductor/-graphene interface and Klein tunneling across a P-N junction in graphene each couples the electron and hole excitation, through the superconducting pair potential $\Delta$ and the electrostatic potential $U$ respectively. Further, it has be shown theoretically that these two processes have identical energy spectra at low energies ($\varepsilon \ll \Delta$), suggesting that the analogy between the two goes beyond their quasi-classical trajectories but purely quantum mechanical[15].

Figure 4.6 illustrates the Andreev reflections in an S-G-S device with local gating. The charge carrier converts to its counterpart Dirac fermion upon entering the locally-gated region and converts back to the original type again when it re-enters the region with global back-gate only. Graphene P-N-P (N-P-N) junctions that carry Josephson current thus provide a system through which investigating the interplay between Klein tunneling and Andreev reflection is possible, whereas the quantum confinement and the focusing effect for electron flow[29] may offer new ways to modulate the supercurrent in a superconducting circuit.

## 4.5 DEVICE FABRICATION

### *Patterning h-BN mask*

The fabrication of the device discussed in this section started with preparing the h-BN mask. First, h-BN flakes were deposited on a piranha-cleaned (see A.1 ) $SiO_2$ substrate. Flakes ranging from 15 to 30nm thick (identified by optical microscope) are chosen and patterned with e-beam lithography. PMMA 950A5 serves as both e-beam resist and the dry-etch mask. After pattern development, the sample is etched by reactive ion etching (RIE) with a gas mixture of Ar (10 sccm), O2 (2 sccm), and CHF3 (10 sccm) at 10 mtorr total pressure [4].

---

[4] This is the current recipe being used at the time of writing. We first used a mixture of $Ar$, $O_2$, $H_2$and $CF_4$ as etching gas which etches h-BN much faster and showed

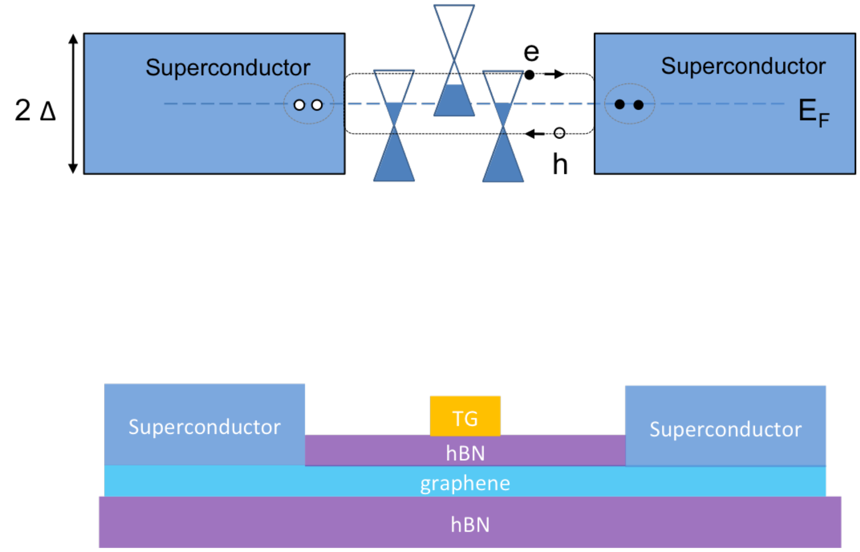

Figure 4.6: Schematics of the Andreev reflection with local variation of electrostatic potential

The etching rate is roughly 0.3 nm/sec, but we found that it varies from time to time (depending on the condition of the chamber) and that it is not linear for at least the first 10 seconds. Figure 4.7 (a) shows the h-BN (structures in blue) after dry etching. The anisotropic nature of reactive ion etching provides a very sharp and well-defined edge profile (confirmed by AFM) of the h-BN masks.

Figure 4.7(b) shows h-BN masks on the polymer stack after the pick-up step described in 4.3.1. This step can be followed by successive picking-up of other Van-der-Waals materials if robust polymers such as PC or PPC (Table 4.2) are used. PMMA has a much lower yield for successive picking-up, as it tears or ripples more easily when disengaged from the substrate.

### *A two-stack approach*

Although it is possible to build heterostructures by multiple pick-up followed by one final transfer to the bottom layer, we typically build our devices in a two-stack fashion especially when the heterostructures consist of many layers. The *bottom stack*, typically made of a large pirece of graphene (a few $\mu m^2$ in area) together with a h-BN substrate and a graphite backgate, can be made more efficiently (the alignment is trivial). However , in more efficient processes, bubbles from and ripples become trapped between layers more easily. Unfortunately, the majority of these surface irregularities can not be detected with an optical microscope during the transfer process, and

---

similar etching rate for both h-BN and $SiO_2$. The current recipe has a much higher selectivity between hBN and $SiO_2$.

only AFM imaging after the entire stack is annealed can reveal the quality of the heterostructures. On the other hand, *a top stack*, which typically includes smaller structures such as a h-BN mask, a fine graphite tunneling probe, and an ultra-thin h-BN tunneling barrier (discussed in Chapter 5) require highly invested fabrication but contain a much lower density of bubbles after annealing (the small scale of the structure allows them to flatten out relatively easily). In practice, when fabricating the top stack is the apparent bottleneck of the entire process, transferring the top stack onto a clean, flat area on the bottom stack will optimize yield and efficiency. The *bottom stack* in Figure 4.7(c) consists of a graphene flake (dark region in the middle) on a h-BN substrate. The graphene can be patterned by e-beam lithography and dry (RIE) etching if necessary and must be cleaned by thermal annealing or contact mode tip cleaning (Appendix A) before the *top stack* is transferred onto the graphene flake.

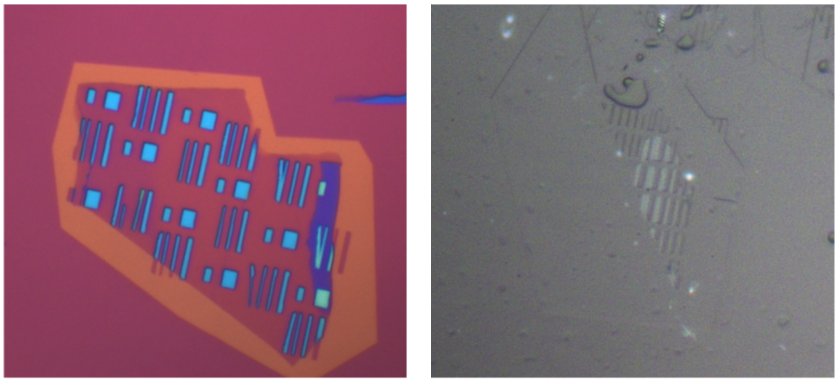

(a) Patterned h-BN mask on $SiO_2$ substrate Thickness of the h-BN ~25 nm.

(b) Optical image of picked-up h-BN mask on PMMA/tape/PDMS stack

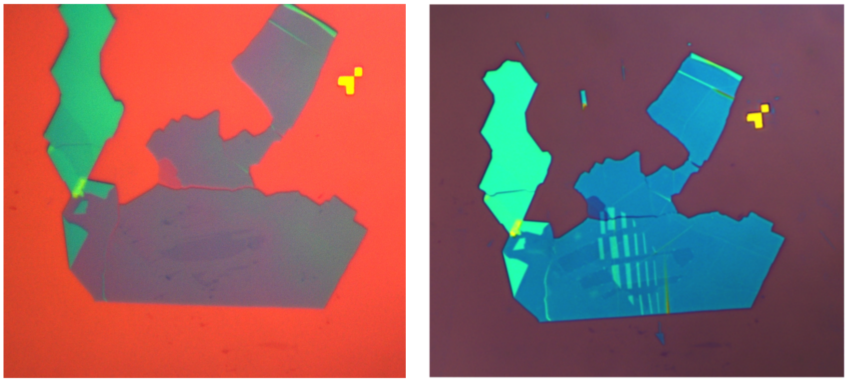

(c) The *bottom stack* of the heterostructure that consists of graphene (dark region in the middle) and h-BN substrate.

(d) h-BN-graphene-h-BN heterostructure after completion

Figure 4.7: Pick-up and Transfer h-BN mask onto a graphene/hBN structure.

| Parameter | Topgate | Superconducting leads |
|---|---|---|
| Material | Ti (5nm)/Au (35nm) | Ti (7nm)/Al (70nm) |
| Lateral dimension | min. line width ~ 150 nm | line width 1.15$\mu m$, |
| | | spacing 400~800 nm |
| E-beam lithography | 550 $\mu C/cm^2$@ 30KeV | 500 $\mu C/cm^2$@ 30KeV |
| Development | $H_2O$:IPA=1:3, 1min. @0°C | $H_2O$:IPA=1:3, 1min. @0°C |
| Evaporator base pressure | $1 \times 10^{-6} torr$ | Ti: $1.1 \times 10^{-7} torr^{*1}$, |
| | | Al: $\leq 3.5 \times 10^{-7} torr^{*2}$ |
| Deposition rate | 1Å/sec | 0.5Å/sec |

*1:After overnight pumping, at least 8 hours

*2:We found that if the pressure is larger than $\sim 5 \times 10^{-7} torr$ after the Ti evaporation is complete and before the Al evaporation starts, the number of fully proximitized graphene Josephson junctions yielded will be significantly lower than when the pressure is lower.

Table 4.3: Parameters for e-beam lithography and superconductor deposition.

### *Lithography and metallization*

E-beam lithography was performed on the heterostructure (fig.4.7(d)) after the structure had been flattened via thermal annealing (3 hours, 350°C in forming gas). The first lithography was performed for the topgate, which was evaporated with Ti/Au (5nm/35nm) using thermal evaporation (orange part in Fig. 4.8(b)). After the topgate had been made, another lithography is performed for the superconducting leads. Note that each window opened in the resist is purposely larger than the area between the neighboring h-BN mask in order to achieve a small overlap between the metal and the mask (circled in dashed lines in Fig. 4.8(c)). This ensured that the graphene can be fully sealed by either the h-BN or the metal.

We used a solution of water and IPA ($H_2O : IPA$ = 1:3 by weight) to develop the exposed PMMA resist at 0°C. Compared to the effect of the more popular MIBK/IPA developer, $H_2O/IPA$ has been found to subject the film to less stress and to render polymer higher sensitivity to the e-beam dosage. Developing the exposed PMMA at low temperature increases the contrast by a factor of ~2[107]. Therefore, $H_2O/IPA$ is a more favorable development procedure for heterostructures with finely-spaced leads than MIBK/IPA is [5].

The sample was deposited with Ti (7 nm) and Al (70 nm) in a thermal evaporator as superconducting leads. The evaporation conditions and other related fabrication parameters are summarized in Table 4.3.

---

[5] We often observe cracks in the resists around the corners of hBN substrates after developing in MIBK/IPA solvent.

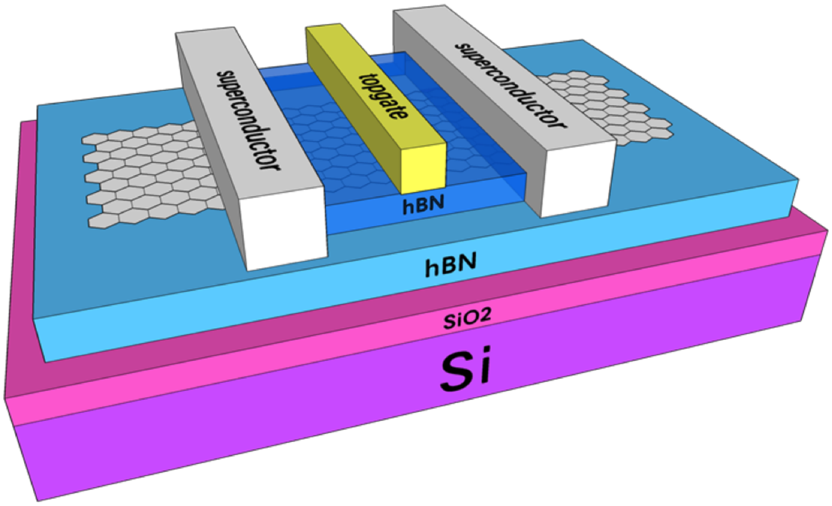

(a) 3-D schematic of a dual-gated *SGS* junction. The part of graphene participating in transport is fully sealed by either h-BN mask of the metallic contact.

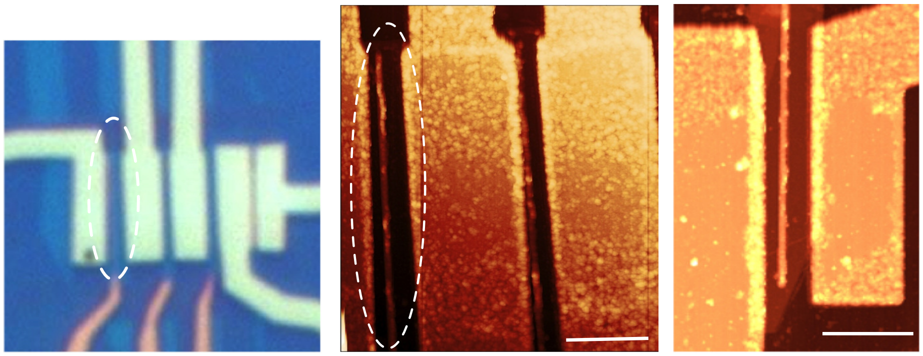

(b) Optical image of the device before measurement. The bright yellow leads are superconducting aluminum contacts, and the orange-color leads are Au topgate electrodes.

(c) AFM micrographs of the dual-gated *SGS* junctions. Junction circled in white dashed line is the same junction as the one circled in (b). The bright rims around each h-BN mask results from overlapping between metal(Al) and the h-BN in to ensure full encapsulation for the flake. Scale bars in both images represent $1\mu m$.

Figure 4.8: Dual-gated graphene Josephson junctions

### 4.6.1 *Implementation of discrete RC filters and characterization of electronic temperature in the measurement setup*

Measurements of the dual-gated *SGS* junctions were performed in the same setup described in Chapter 3. In order to measure the Josephson current induced by aluminum, whose superconducting gap is about 10 times smaller than that of NbN ($\triangle_{Al} \sim 170\mu eV$, $\triangle_{NbN} \sim 2meV$) , we installed at the mixing chamber stage a discrete RC (low-pass) filter consisting of surface mount components on a PCB board (Fig. 4.10(b)). The cut-off frequency (-3dB) is 8K Hz with two equivalent RC stages (R=2$K\Omega$, C=10nF). To demonstrate the effect of low-pass filtering, Figure 4.9 shows the I-V measurement of an Al-graphene-Al weak link on a $SiO_2$ substrate measured (a) with a cryogenic copper tape filter only and (b) with an extra RC circuit (using one stage of the same RC as in the PCB-board filter) connected to the break out box. The *I-V* characteristics recovers from nearly-ohmic to fully Josephson-like behavior when the RC filter is implemented. The effect of RC filtering is obvious even though the filter is installed at room temperature and was not properly shielded. In addition, the cable that connects the breakout box and the fridge's electrical feedthrough was not filtered and may still have picked up some noise along the path.

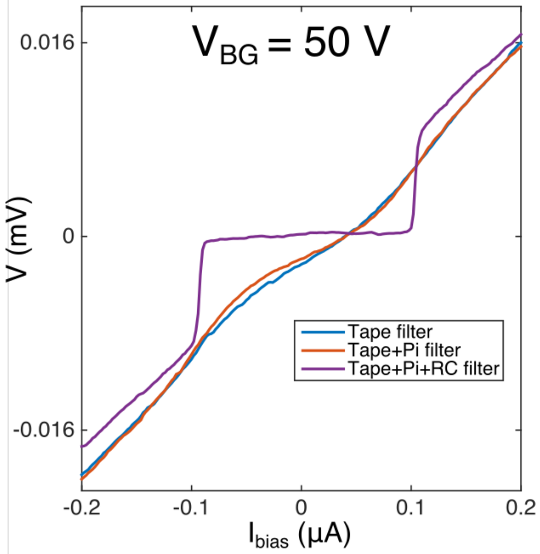

Figure 4.9: Effect of RC filtering on the measurement of Josephson current in a Al-graphene-Al weak link. R=2k, C=10 nF

We can further characterize the electronic temperature by performing tunneling spectroscopy on a superconductor with a superconduct-

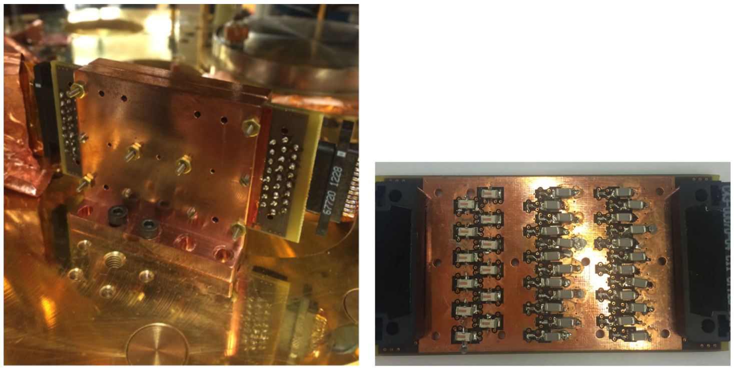

(a) Discrete PCB RC filter mounted on the mixing chamber of the fridge. (b) Surface mount components of discrete RC filter.

Figure 4.10: Pictures of home-made RC filter on a PCB board.

ing gap of a known size. The electronic temperature can be extracted from the measured gap based on BCS theory (see 5.4 in chapter 5).

### 4.6.2 *Normal state characterization*

#### *Quantum confinement and Fabry-Pérot oscillation of resistance in a locally-gated region*

Without loss of generality, we use the measurement taken on the longest junction ($L \times W = 0.85\mu m \times 2.80\mu m$) in Figure 4.8(b) (circled with white dashed lines) to demonstrate the main results of this experiment unless otherwise specified.

Figure 4.11 shows the resistance measured as a function of topgate $V_{TG}$ and backgate $V_{BG}$. The resistance was measured with a standard lock-in technique by applying $1\mu A$ current excitation, which was much larger than the critical Josephson current of the device. Therefore, no Josephson effect is assumed in this measurement.

The topgate in the middle of the SGS junction offers an extra knob to tune the carrier density in the locally gated region. The polarity of the entire device can, therefore, be determined by an arbitrary combination of $V_{TG}$ and $V_{BG}$. Regardless of the doping effect from the contacts, these combinations result in four distinct regions in the 2-D resistance map, i.e., P-N-P, N-P-N, P-P'-P, and N-N'-N as shown in Figure 4.11. If the aluminum contact doping is taken into account, the encapsulated device is terminated by two n-doped regions as shown in [70, 47].

The most obvious feature in the resistance plot is the oscillation observed in the bipolar (P-N-P or N-P-N) regions. In order to understand the oscillation, let us first look at the N-P-N potential profile in Figure 4.6 (superconductors play no role in the discussion here).

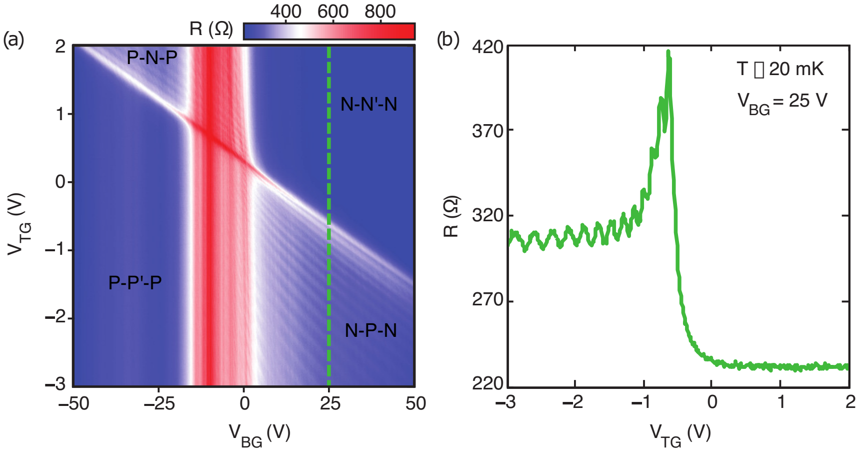

Figure 4.11: Normal state characterization: resistance as a function of topgate voltage $V_{TG}$ and backgate voltage $V_{BG}$ (a) A 2-D resistance map as a function of $V_{TG}$ and $V_{BG}$. Combination of the two gate voltages defines four different regions in the map. Pronounced oscillation is observed in the bi-polar (N-P-N, or P-N-P) regions as a result of quantum confinement and phase coherent transport. (b) Line-cut along $V_{TG}$ axis at $V_{BG} = 25V$, showing vivid oscillation of resistance.

The two N-P interfaces, and the corresponding potential barrier in the graphene create a quantum confinement cavity for the charge carriers. In graphene, however, the potential barrier can be highly transparent, as the chiral Dirac fermion can pass the potential barrier, regardless of the potential height and depth (the length of the cavity), via Klein tunneling with a high transmission probability as discussed in Chapter 1. Analogous to wave optics, the locally gated region can be regarded as a Fabry-Pérot cavity for the charge carriers (Fig. 4.12). When phase coherence is preserved, successive transmitted rays $T_1$ and $T_2$ have a dynamic phase difference $\Delta\phi = 2kL_{cavity}\cos\theta$ , where $k$ is the wave vector of the ray, $L_{cavity}$ the length of the cavity, and $\theta$ the incidence angle. Total transmission probability $T(\theta)$ can be obtained by summing all the partially transmitted rays which yields

$$T(\theta) = \frac{1}{1 + Fsin^2(\Delta\phi/2)}, \tag{4.1}$$

where $F$ is the finesse of the cavity defined as $F = 4 \mid r_1 \mid\mid r_2 \mid / \mid t_1 \mid^2\mid t_2 \mid^2$, with $r_{1,2}$ and $t_{1,2}$ the reflection and transmission rate amplitude at two interfaces. Constructive interference, or say the resonance condition $T(\theta) = 1$, occurs when $\Delta\phi = 2N\pi$,where $N = 0, 1, 2...$ corresponding to the number of roundtrips between two successive waves.

A Fabry-Pérot interferometer (etalon) can be tuned to resonance by varying $L_{cavity}$ or the wavelength of light. In a dual-gated graphene device, $L_{cavity}$ is pre-determined by the dimension of the topgate elec-

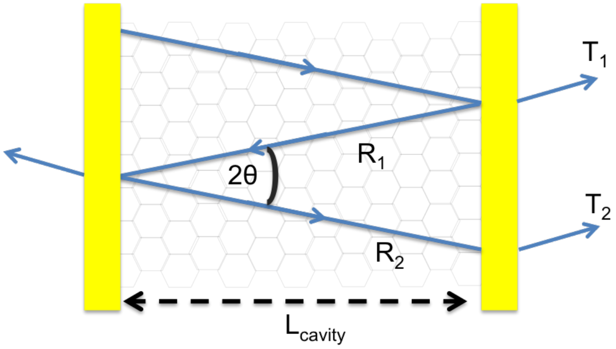

Figure 4.12: Schematic of a Fabry-Pérot cavity

trode and, therefore, cannot be changed. However, the wave vector $k_f$ can be tuned by gating by $k_f = \sqrt{n\pi}$,where $n$ is the carrier density. The conductance (resistance) resonance condition in a gate-tunable graphene P-N-P (N-P-N) junction is, therefore, $\Delta k_f L_{cavity} = \pi$, which can be expressed as $\Delta n = 2\sqrt{\pi n}/L_{cavity}$. $\Delta k_f$ and $\Delta n$ denote the difference in wave vector and density, respectively, between two consecutive conductance (resistance) peaks.

By taking a line-cut from the 2-D resistance map at $V_{BG}$= 25 V, we can identify the Fabry-Pérot cavity where oscillation in bipolar domains originate, as shown in Figure 4.11(b). In the $V_{TG} < -1$ volt region, peak separation around the Dirac point (more precisely, around the charge neutrality point in the locally-gated region) corresponds to $\Delta n \sim 10^{10} cm^{-2}$ at a gate voltage where $n \sim 10^{11} cm^{-2}$. The effective $L_{cavity}$ for our device is therefore ~ 100 nm, which is in good agreement with the geometrical width of the top gate. This result is consistent with those reported in the literature[136, 25] and tells us that charge carriers in the locally-gated region remain phase coherent and ballistic.

The line-cut in Figure 4.11(b) shows an oscillation with a fairly constant contrast, independent of the potential barrier at the P-N interfaces, whose height is set by $\mid V_{TG} \mid$, whereas $V_{BG}$ provides a global potential background. This is characteristic of Klein tunneling of Dirac fermions[77], in which the transmission amplitude $t_{1,2}$is independent of the barrier height and width ($L_{cavity}$ in our case) when impinging normally ($\theta = 0$ [6]) on the barrier. Note that in an Fabry-Pérot interferometer, visibility of the interference pattern is determined by the finesse $F = 4 \mid r_1 \mid\mid r_2 \mid / \mid t_1 \mid^2 \mid t_2 \mid^2$, so that the fairly constant contrast observed in our oscillation is consistent with what is expected for Klein tunneling.

---

[6] We consider mainly the contribution from normal incidence, as the transmission amplitude drops rapidly with $\theta$ . See, for example [77, 104]

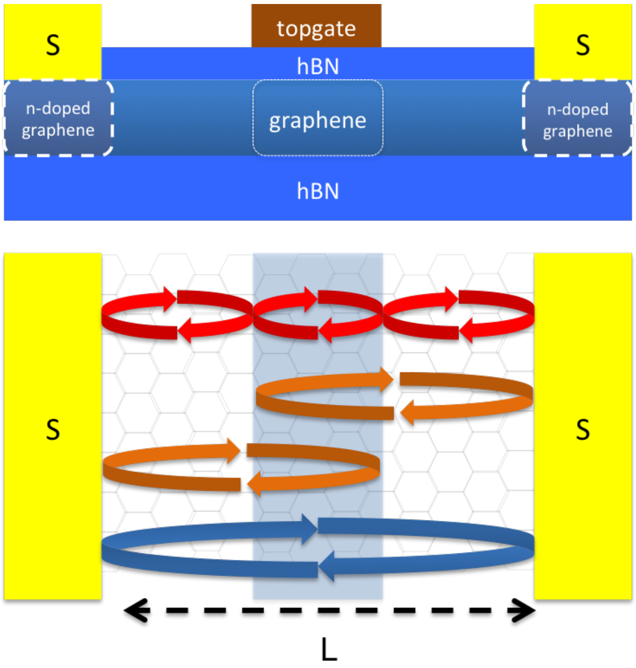

Figure 4.13: Fabry-Pérot cavities in a dual-gated junction. Multiple cavity modes are defined by different interfaces within the junction.

*Ballistic or diffusive?*

The goal of the experiment in this chapter is to induce superconductivity in ballistic graphene. However, the ballistic transport across the entire device can not be concluded from the Fabry-Pérot oscillation observed in the bipolar domains, as it only suggests the existence of phase-coherent, ballistic transport in the locally-gated region, which has been observed in devices on $SiO_2$ with topgate narrower than 20 nm[136]. In fact, as the inhomogeneity of carrier density imposes finite-reflective interfaces in the 2-DEGS, we should expect to see more than one Fabry-Pérot mode given the configuration of our device (Fig. 4.13).

In Figure 4.14, a numerical derivative of resistance is taken with respect to $V_{BG}$ shown as a function of gate voltages in order to clarify the oscillatory features in our measurement. With the n-doped graphene under the leads taken into account, the four domains can be relabeled as n-P-P'-P-n, n-N-P-N-n, n-N-N'-N-n, and n-P-N-P-n, where the lower-case $n$ denotes the aluminum contact-doped region (n-type doping by Al[63]). We observe at least one extra oscillation over the background which is shown in the n-P-P'-P-n domain (guided by the black lines in Fig. 4.14 ), whereas the n-N-N'-N-n domain, which is unipolar and imposes much weaker confinement in comparison, remains featureless.

This new oscillation is omnipresent in the n-P-P'-P-n domain with varying visibility, as can be seen in the zoomed-in image shown in figure 4.14(b). At carrier density $n \sim 2.0 \times 10^{12} cm^{-2}$ (enclosed by the dashed lines in Fig. 4.14(b)), the change of carrier density $\Delta n$ that corresponds to one oscillation is ~$5.8 \times 10^{10} cm^{-2}$, leading to a cavity length of $L$ ~ 870 nm. This value agrees fairly well with the size of our hBN mask ($L$=850 nm) for this junction. We conclude that this oscillation in an n-P-P'-P-n domain must arise from quantum interference over the entire device, that is, from the p-type charge carriers traveling ballistically across the entire length of device $L$ and partially bouncing back by the n-doped region. In general, the occurrence of the Fabry-Pérot oscillation in electronic transport implies that the phase-coherence length exceeds twice the cavity length[104]. The fact that we can deduce a Fabry-Pérot cavity length that is close to the contact-to-contact distance from the interference pattern can be regarded as a sign of phase coherent ballistic transport across the entire device [7].

---

[7] We also calculated $l_{mfp}$ using the semiclassical relation as described in Chapter 3 (3.4.1). Due to the limit in device geometry, we could only perform a two-probe measurement, which revealed only the lower-bound of the mobility and $l_{mfp}$. The extracted $l_{mfp}$is about 390 nm, comparable to the longest distance from the contact to the edge of the locally gated region[126]. The result was expected, as the transport measurement integrates all transport channels whereas with an interference pattern it is possible to distinguish among different modes.

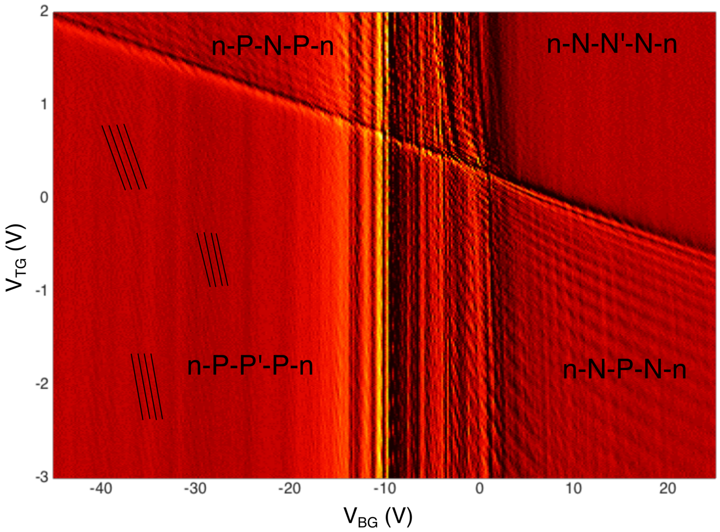

(a) Numeric derivative of the measurement shown in fig.4.11(a) with respect to $V_{BG}$. An extra set of oscillation now can be observed in the n-P-P′-P-n region (highlighted by black dashed lines for guiding) The small periodicity corresponds to a longer cavity, which is the lead-to-lead distance in our device.

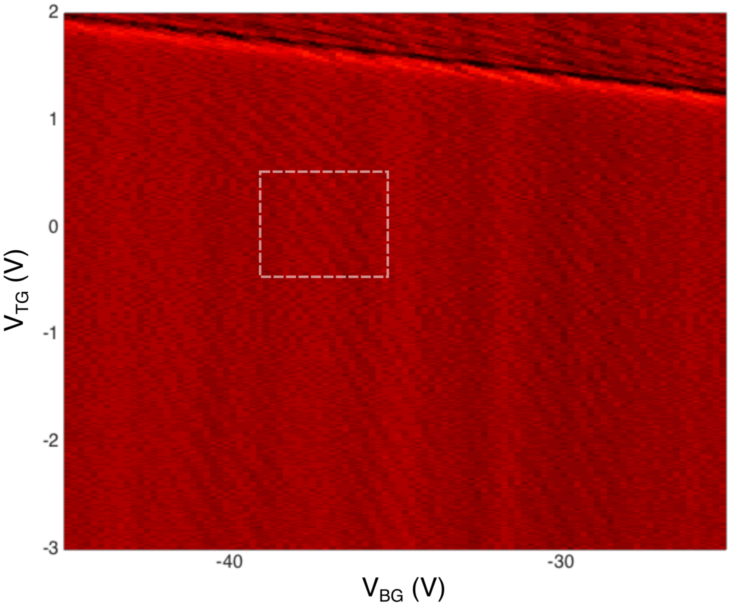

(b) A closer look into the P-P′-P region of (a). The oscillation highlighted by the white box exhibits a Fabry-Pérot mode that corresponds to a cavity length ~ 870 nm, which is very close to the length h-BN mask, i.e. the entire encapsulated region.

Figure 4.14: Fabry-Pérot cavity corresponding to the full length of the junction.

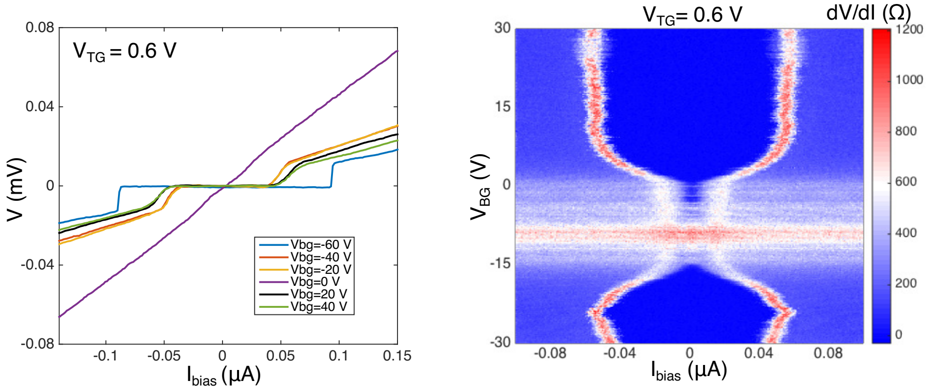

(a) *I-V* characteristic of a dual-gated Josephson junction, plotted against different gate voltatges

(b) Differential resistance $dV/dI$ as a function of backgate voltage $V_{BG}$. Topgate voltage $V_{TG}$ is set at 0.6 V

Figure 4.15: Induced superconductivity in dual-gated, ballistic graphene device

### 4.6.3 *Measurement in the superconducting regime*

*Induced superconductivity in the Josephson weak-link made with ballistic graphene*

Figure 4.15 (a) plots the *I-V* characteristics of a dual-gated Josephson weak link at various backgate voltages when measured in a small bias current regime. The current is dissipationless, i.e., no voltage drop accompanies the finite current flow, in the flat region beyond which the junction switches to normal state. This behavior is similar to the NbN-based SGS junctions discussed in Chapter 3, despite the smaller critical current that is dictated by the aluminum gap. The gate-dependence of the proximity effect can be seen more clearly in Fig. 4.15(b) where the superconducting state is illustrated by the zero $dV/dI$ region. The proximity effect is strongly suppressed in the region where $V_{BG}$= -15V ~ 0V, showing no sign of the Andreev reflection at $V_{BG}$ around -13 volts as $dV/dI$ peaks at zero current bias.

We ascribe the region with suppressed superconductivity to the vertical, highly-resistive strip observed in the 2-D normal state resistance map (Fig. 4.11(a)), whose origin is not clearly understood from our measurement [8]. In a Josephson weak link, the product of the critical current $I_{c0}$ and the normal state resistance $R_N$ remains constant at a given temperature $T$ below $T_c$[120]. In particular, the relation for a ballistic *S-G-S* junction can be written as[121]

$$I_{c0}R_N = \alpha\Delta_0/e \tag{4.2}$$

---

[8] This strip occurs in all the dual-gated junctions that we have measured. The fact that it shows no dependence on the topgate implies that it may originate from the doping caused by the topgate material.

, where $\alpha = 2.08$ at the Dirac point and 2.44 in the high carrier density regime. Thus when $R_N$ is too large, the maximum Josephson current may become too small to be detected.

#### 4.6.3.1 *Fabry-Pérot oscillation of the maximum Josephson current*

The relation in 4.2 also explains the observed oscillation of the maximum Josephson current $I_c$ in the bipolar domaines, as depicted in Figure 4.16 when $V_{TG}$ <-0.5 V. Here, the differential resistance as a function of the bias current is plotted along the line cut in Figure 4.11 (b), which is also presented here for comparison. Here, $I_c$ , defined by the boundary of the zero $dV/dI$ region, oscillates out-of -phase with the Fabry-Pérot oscillation of normal state resistance $R_N$, as expected from 4.2[24, 113, 4].

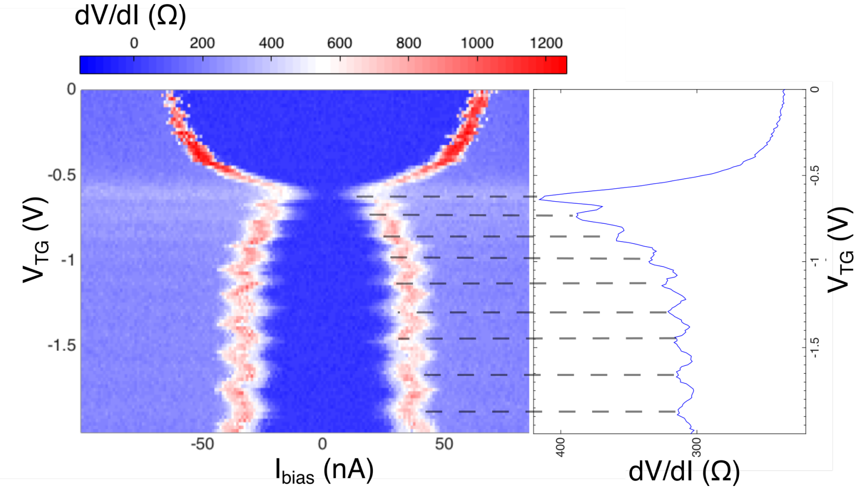

Figure 4.16: Fabry-Pérot oscillation of Josephson effect. The critical current $I_C$ oscillates out-of-phase with the normal state resistance $R_N$ as expected for a Josephson junction.

Figure 4.17 shows the Fabry-Pérot oscillation of $I_c$ along two line-cuts in the 2-D resistance map. Both graphs show pronounced oscillation of $I_c$ in the *n-N-P-N-n* and *n-P-N-P*-n regions. In the measurement along line-cut A, we also observe oscillation in the *n-P-P'-P-n* region, which is equivalent to the bipolar domain (*n-P-n*, in our notation) created by contact doping and the global backgate in ballistic junctions where Fabry-Pérot oscillation of $I_c$ is observed[24, 113, 4]. Analysis shows that the Fabry-Pérot oscillation of $I_c$ has the same periodicity as the oscillation shown in Figure 4.14 (b) which corresponds to the interference across the entire junction length. We conclude that at least a certain fraction of the Josephson current is carried by ballistic transport from lead to lead.

Figure 4.18 plots the same measurement of line-cut A in a different color scale to emphasize the oscillation in both domains.

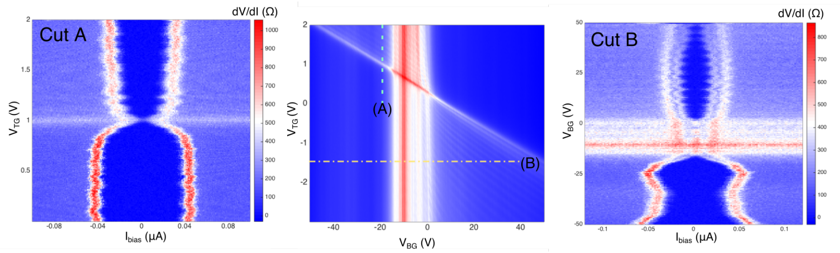

Figure 4.17: $dV/dI$ versus bias current measured along different cuts in the 2-D resistance map. Oscillation in $I_c$ is consistent with the $R_N$ oscillation. Line-cut A shows oscillation of $I_C$ in both regions.

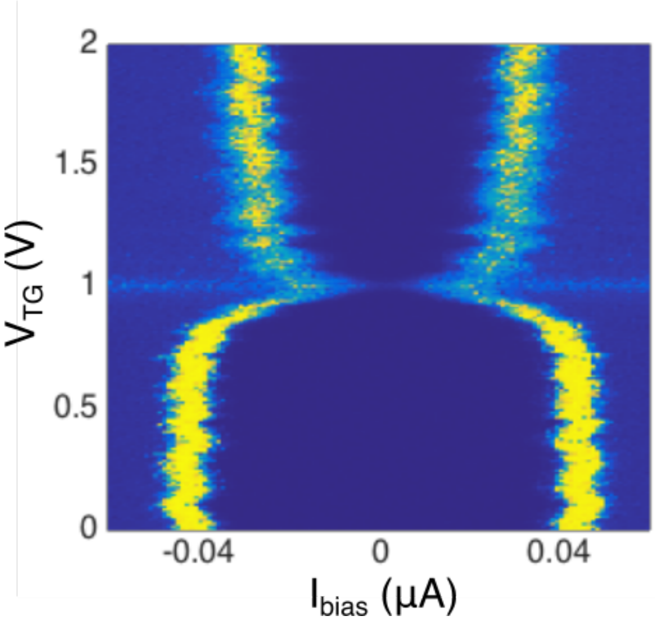

Figure 4.18: Plot of cut A in different color scale to emphasize the oscillation in n-P-P′-P-n regime

### 4.6.3.2 *Ballistic Josephson effect from a scaling point of view*

One of the signatures of the Josephson effect in ballistic graphene is what is referred to as the pseudo-diffusive behavior, according to which for a short and wide junction at the Dirac point ( $\mu \ll \hbar v/L$, $L \ll W, \xi$, where $\xi$ is the coherence length) , $I_c$ scales with the dimension of the junction as [121]

$$I_c = 1.33 \frac{e\Delta_0}{\hbar} \frac{W}{\pi L} \tag{4.3}$$

Thus, at the Dirac point, the critical current in a ballistic *S-G-S* junction is formally identical to that induced in a piece of diffusive metal. This is consistent with the finding that ballistic Dirac fermions have the same shot noise as do diffusive nonrelativistic electrons and that the transport arises from evanescent electronic states [121, 44, 35].

At the high carrier density limit ($\mu \gg \hbar v/L$), $I_c$ in a short and wide ballistic *S-G-S* junction can be expressed as

$$I_c = 1.22 \frac{e\Delta_0}{\hbar} \frac{\mu W}{\pi \hbar v} \tag{4.4}$$

$I_c$ depends on only one geometrical factor, the width $W$ , as the total current is proportional to the number of ballistic channels that mediate the electronic transport.

It is very challenging to measure the critical current at the Dirac point, as the current might be too small to determine. However, we can explore the ballistic characteristics in the opposite limit by comparing critical current $I_c$ measured in two junctions with different dimensions (Fig.4.19). With$V_{BG}$ =35 volt, $V_{TG} = 0.28$ volt ($n_e = 2.5 \times 10^{12} cm^{-2}$) and $L = 850$nm (the longer junction of the two), the ratio between $\mu$ and $\hbar v/L$ is ~ 238:1 (184 meV: 0.77 meV). Thus, it is reasonable to assume the high density limit described by eqn. (4.4).

Table 4.4 summarizes the comparison between the two junctions. We notice that although junction A is more than three times longer than junction B ($L_A/L_B = 3.4$), and wider by only 20%, the maximum supercurrent in junction A is still significantly larger than that in junction B at the same chemical potential [9]. We emphasize that the two junctions were built on a single piece of monolayer graphene on the same h-BN substrate, such that the only varying parameter in eqn. (4.4) is the width $W$. Note that in diffusive metal, the conductance, and thus the $I_c$ it sustains, is expected to scale with aspect ratio $W/L$. The fact that $I_c$ measured in the encapsulated device exhibits very weak or even no dependence on junction length $L$ and increases

---

[9] Junction B is so narrow that we did not implement any topgate in the middle. We compared the two junctions at very similar carrier density, where $V_{BG}$ is kept the same, and the $V_{TG}$ in junction A is very small (0.28 V). Also, as the locally-gated region is only ~12% of the area in junction A, the value of $V_{TG}$ does not affect overall density significantly.

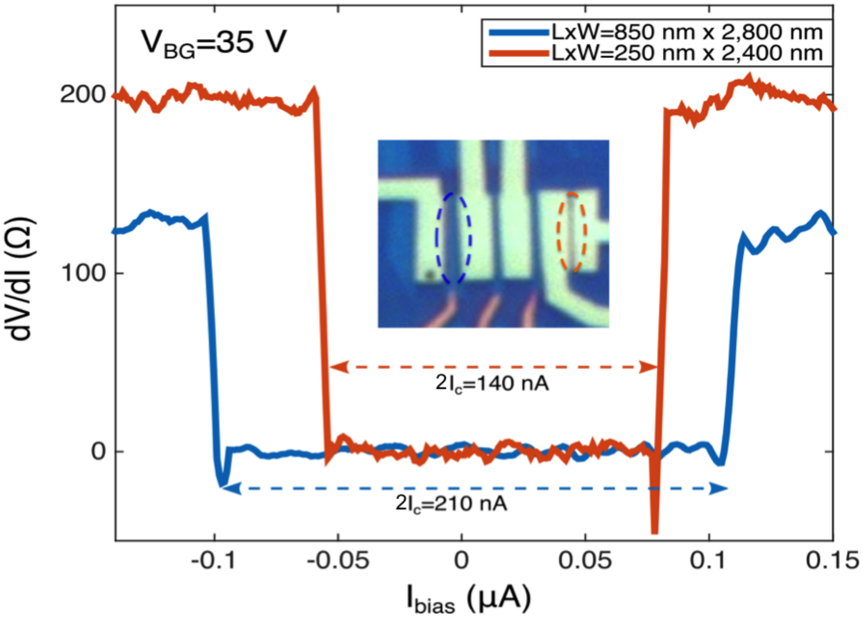

Figure 4.19: Comparison of maximum supercurrent $I_c$ in two junctions of different dimensions. $I_c$ exhibits weak dependence in the junction length $L$ but increases with the width $W$, as expected for ballistic channels. Note that all junctions are built on one single graphene flake and shares the same backgate.

| Junction | $L(\mu m)$ | $\frac{L_A}{L_B}$ | $W(\mu m)$ | $\frac{W_A}{W_B}$ | $I_c(nA)$ | $\frac{I_{cA}}{I_{cB}}$ | $\mu(meV)$ |
|---|---|---|---|---|---|---|---|
| A (blue) | 0.85 | 3.4 | 2.8 | 1.2 | 105 | 1.5 | ~185 |
| B (orange) | 0.25 | | 2.4 | | 70 | | |

Table 4.4: Comparison of critical current in junctions with different dimensions.

with width $W$ suggests that the characteristic is consistent with the ballistic model.

## 4.7 CONCLUSION

We have demonstrated that by encapsulating a graphene flake between clean h-BN sheets, it is possible to achieve an electron mean free path that is comparable to the distance between the most separated leads. In the case presented herein, the longest distance is ~ 850 nm owing to the requirement for the superconducting proximity effect. The phase coherence of electronic transport manifests itself in the Fabry-Pérot oscillation of normal state resistance, suggesting that the electron travels ballistically within cavities defined by interfaces of differently doped regions. Despite the oscillations observed in the n-P-N-P-n, and n-N-P-N-n regions, the existence of oscillations in the *n-P-P′-P-n* region is of particular importance, as the cavity length derived from the periodicity is very close to the length of the junction. This implies that our fabrication method can be used to facilitate appreciable ballistic transport across the entire device.

In the superconducting regime, the oscillation of the maximum supercurrent $I_c$ shows good agreement with the ballistic behavior observed in normal regimes. In addition, by comparing the $I_c$ at two encapsulated Josephson junctions that differ in size, we observe that the scaling with geometry is compatible with the ballistic model at a high-density limit.

We conclude that this fabrication technique is able to produce ballistic *SGS* junctions.

# 5

# TUNNELING SPECTROSCOPY OF SUPERCURRENT-CARRYING ANDREEV STATES IN GRAPHENE

## 5.1 INTRODUCTION

The use of tunneling spectroscopy to study superconductivity has a long history dating back to the 1960's. In fact, this technique, introduced by Giaever in 1960[60, 61], was used at first to measure the existence of the BCS gap in aluminum/aluminum oxide/lead sandwiches. Subsequently, planar tunneling from a normal metal to superconductor and planar tunneling between two superconductors[59, 62] provided more support for the BCS theory and substantiated our understanding of this subject.

The invention of the scanning tunneling microscope (STM) in 1981 by Bining and Rohrer provided a spatially-resolved tunneling spectroscopy tool for the study of solid state systems. The atomic resolution offered by STM makes it a promising tool for studying the proximity effect in a hybrid superconducting system. With a cryogenic AFM+STM system, H. LeSueur et al.[84] measured the induced superconducting gap or mini-gap in a diffusive silver nanowire proximitized by a superconductor on both ends. The size of the measured mini-gap diminishes as the STM tip moves away from the superconductor, and is weaker in longer than in shorter junctions. In addition, the phase-controlled oscillation of the mini-gap is reminiscent of the behavior of Andreev bound states. The proximity effect has also been investigated in a disordered 2-dimensional system[112], whereas superconducting islands are grown in-situ on thin, diffusive metal films, resulting in a network of *SNS* junctions that can be probed by STM. Direct observations of Josephson cores[106] in such a system demonstrate how the macroscopic phase in superconductors strongly influences the proximitized region.

Advances in microfabrication has also promoted the study of the hybrid superconducting system at the mesoscopic scale. Precursors of discrete Andreev levels in ballistic *SNS* channels have been shown to exist in *Nb*-contacted *InAs* 2DEGS samples via energy spectroscopy[94]. However, it was not until an experiment performed by J.D. Pillet et al.[101] that a single Andreev bound state in a hybrid system was directly observed. In this experiment, a carbon nanotube was coupled to an aluminum ring, and a quasi-particle energy spectrum was obtained by a tunneling probe positioned on top of the weak link. The local density of states exhibit a strong gap associated with the aluminum superconducting gap. When a magnetic field is threaded through the loop formed by the aluminum and the carbon nanotube, the size of the induced gap in carbon nanotube oscillates with a periodicity equal to the magnetic flux quantum $\Phi_0$. On the basis of both data analysis and modeling, the conclusion drawn from this experiment is that the Andreev bound states are localized in the quantum dot region, which is defined by superconducting leads and the tunneling probe. In 2013, the existence of the Andreev excited state $E_A^+$ (the higher energy state in each pair in the Andreev bound state solution) was confirmed in the superconducting atomic contacts shown by Landry Bretheau et al.[21].

Also, in 2010, transport through Andreev bound states in a superconductor/oxide/graphene system was reported in ref.[45]. In this experiment, the gate-tunability of graphene manifests itself in the varying quantum dot energy level which is Andreev-coupled to the superconductor. Direct observation of the induced superconducting gap in graphene was presented in 2013[123], in a study in which graphene was grown on a superconducting rhenium film and probed by STM in-situ.

In this chapter, we discuss our study of the superconducting proximity effect in the energy domain, which has not been researched extensively in regard to the graphene proximity effect. Based on the fabrication techniques we developed earlier, as discussed in Chapter 3 and Chapter 4, and innovations introduced for this particular experiment, we are able to probe the local density of states of superconducting-proximitized graphene. Based on a SQUID-like geometry, the phase difference across the weak link can be well-controlled by applying an external magnetic field, resulting in the variation of the gap size that we recognize as a modulation of the Andreev energies.

The purpose of this experiment is to study the superconducting proximity effect in 2-dimensional limit. In this sense, the graphene heterostructure is regarded as an easily accessible host of 2-DEGS. On the other hand, the unique electronic properties of graphene may exhibit novel phenomenology, which can be explored using the spectroscopic technique.

## 5.2 TUNNELING SPECTROSCOPY OF ANDREEV BOUND STATES IN GRAPHENE

### 5.2.1 *Quantum tunneling and the density of state*

In this sub-section, we demonstrate how the density of states (D.O.S.) of a solid state system can be extracted by measuring the tunneling current between the sample and a probe, the latter of which is usually a metallic lead with known density of states.

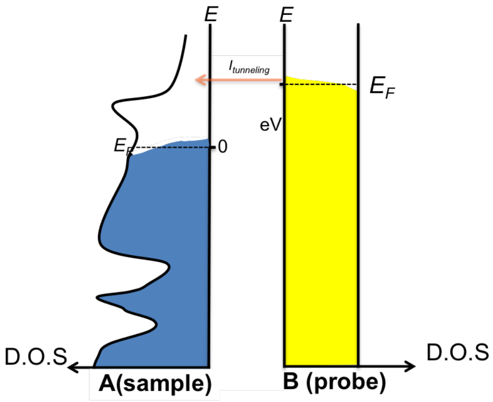

Figure 5.1: Illustration of tunneling spectroscopy as a tool to probe D.O.S.. A barrier, typically a vacuum or thin insulating layers, separates two electrodes and allows tunneling between the two. Particles can tunnel from filled states to the available (empty) states at the same energy. When the bias voltage $V$ is varied, the separation between the two Fermi levels makes it possible to map out the density of states of the sample on the left.

Consider two independent systems $A$ and $B$ separated by a thin barrier that allows quantum tunneling of the electrons (Fig. 5.1). Tunneling current from $B$ to A, up to a proportionality constant omitted here, can be written as[120]

$$I_{b\to a} = \int_{-\infty}^{+\infty} |t|^2 N_a(E)\,[1 - f(E)]\, N_b(E + eV) f(E + eV) dE, \tag{5.1}$$

where $N(E)$ is the density of states, $f(E)$ is the Fermi-Dirac distribution function at temperature $T$, $V$ is the bias voltage across the tunneling barrier, and $t$ denotes the tunneling matrix element between $A$ and $B$, which is assumed to be a constant in this expression. By definition, factors $N_b f$ and $N_a(1 - f)$ represent the number of occupied states in $B$ and the available(empty) states in $A$ per unit energy interval, respectively. Similarly, the tunneling current associated with the inverse process can be expressed as

$$I_{a\to b} = \int_{-\infty}^{+\infty} |t|^2 N_a(E) f(E) N_b(E + eV)\,[1 - f(E + eV)]\, dE. \tag{5.2}$$

The total tunneling current can be obtained by summing up the two processes which yields

$$I_{tunneling} = |t|^2 \int_{-\infty}^{+\infty} N_a(E) N_b(E + eV)\,[f(E) - f(E + eV)]\, dE, \tag{5.3}$$

where we assume an energy-independent tunneling probability $t$. In a tunneling spectroscopy experiment using standard a lock-in technique, we typically measure the differential conductance $G \equiv \frac{dI_{tunneling}}{dV}$, which can be obtained by imposing a small sinusoidal oscillation $dV$ on bias voltage, and measuring the associated change in tunneling current $dI$ as a function of bias voltage. Furthermore, the spectroscopy is typically measured with a probe that has a known or constant density of states. In the latter case, the differential conductance can be expressed as

$$G = \frac{dI_{tunneling}}{dV} = |t|^2 N_b \int_{-\infty}^{+\infty} N_a(E+eV) e \frac{-\partial f(E+eV)}{d(eV)} dE, \quad (5.4)$$

where we assume system $B$ is the probe with a constant density of states $N_b$. Note that the factor $\partial f(E+eV)/\partial V$ is a bell-shaped weighting function peaked at $E = -eV$, with a width of $\sim 4KT$ and a unit area under the curve[120]. As temperature $T \to 0$, $\partial f(E+eV)/\partial V \to \delta(E+eV)$, then

$$G\,|_{T=0} = \frac{dI_{tunneling}}{dV}\,|_{T=0} = |t|^2 N_b N_a(e\,|V|) = const. \times N_a(e\,|V|). \quad (5.5)$$

At $T \to 0$, the density of states of the sample $N_a(eV)$ is proportional to the differential conductance $G$. Varying the bias voltage , thus, allows the density of states $N_a(E)$ to be probed at various energy away from the Fermi level.

In practice, $G$ is measured at a low temperature via a tunneling probe which has a well-defined or constant $N_b(E)$ in the energy range of interest, so that $N_a(E)$ can be extracted directly.

### 5.2.2 *Andreev bound states in 2-dimensional limit*

In Chapter 2 (2.4.2), we discussed Andreev bound states in both long and short 1-dimensional channels. The distinction between the two limits stems from the relative strength between the confinement energy and the superconducting gap. This can be seen from the criteria for the short junction limit $k_F L \frac{E}{E_F} \ll 1$, which is equivalent to stating that the level spacing $\frac{hv_F}{L}$ due to quantization in the longitudinal direction, is much larger than the superconducting gap $\Delta$.

For a 2-dimensional system at the mesoscopic scale, the same argument can be applied and the transverse modes would form Andreev bound states within the superconducting gap when the channels couple to the superconductor. The junction may fall well within the short limit in its longitudinal dimension (in parallel with the supercurrent transport), which allows only one pair of Andreev bound states in the gap (eqn.(2.48)). However the extended dimension in the perpendicular direction may accommodate multiple pairs of Andreev bound states that differ from each other in terms of $E_A$'s. To understand how Andreev bound states may differ from the states we discussed in a 1-dimensional model, let's consider a 2-dimensional *SGS* junction, as

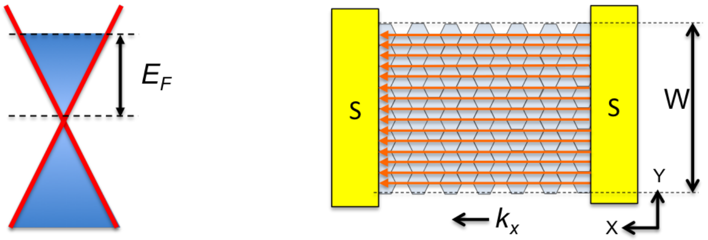

(a) ABS in 2-dimensionl (graphene) system at high carrier density. Transverse modes with energies lower the Fermi energy are populated.These modes may form Andreev bound staets in the weak linke when coupled to superconductors.

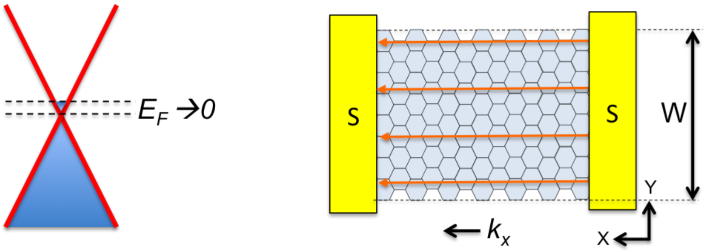

(b) ABS in 2-dimensionl (graphene) system with low carrier density. The number of modes are lmited by the low Fermi energy near charge neutrality point.

Figure 5.2: Andreev bound states in 2-dimensional (graphene) system. Note that we assume single longitudinal mode for the purpose of illustration.

shown in Figure 5.2(a). The number of transverse modes is expected to depend on the width $W$ and the chemical potential $\mu$ of the normal metal. By requiring traveling wave solutions for the supercurrent transport in the $x$-direction with given $W$ and $\mu$

$$k_{Fx}^2 = \left(\frac{\mu}{\hbar v_F}\right)^2 - \left(\frac{\pi}{W}\right)^2 n_y^2 > 0 \tag{5.6}$$

, we can solve for the upper bound for the number of transverse modes $n_y$ as

$$n_y < \frac{W\mu}{\pi\hbar v_F}. \tag{5.7}$$

Thus, the number of transverse modes is proportional to the width $W$ and the chemical potential $\mu$ as expected [1].

Thus for a 2-dimensional *SNS* system in general, the superconducting gap will be populated with Andreev bound states formed by the coupling between these $n_y$ transverse modes and the superconductor. Instead of seeing a single Andreev bound state as in a proximitized carbon nanotube[101], which is exactly one-dimensional, we should expect to see an Andreev band consisting of multiple Andreev bound states at various $E_A's$. Note that the spectra of this Andreev energy band should still vary with the macroscopic phase $\phi$ according to eqn. 2.48 or eqn. 2.49, depending on the junction length in the $x$-direction.

Graphene in general behaves like a purely 2-dimensional system; however, its gate-tunability allows us to tune the Fermi energy to essentially zero. Thus, for a short, ballistic *SGS* junction, it is possible to achieve a very small number of Andreev bound states (Fig.5.2(b)), such that the isolated Andreev bound state can be resolved within the gap by tunneling spectroscopy. The graphene thus behaves like a pseudo 1-dimensional system in terms of superconducting transport.

For a short, ballistic *SGS* junction with $W = 500$nm,$n_y$ <15 can be achieved at $\mu \sim 60$ meV. Such a low chemical potential, corresponding to a carrier density of ~ $2 \times 10^{-11} cm^{-2}$, is achievable (nontrivially!) in a high quality graphene device.

## 5.3 FABRICATION OF TUNNELING DEVICE

The device discussed in this chapter is encapsulated between h-BN top and bottom layers. Thus, techniques developed for the encapsulated device discussed in Chapter 4, such as picking-up, transfer, cleaning, thermal treatment, and device characterization, can be used to fabricate tunneling devices.

---

[1] The result is derived for massless Dirac Fermions in graphene. For massive particles with quadratic dispersion, $n_y$ is proportional to $W\sqrt{\mu}$ as derived in ref.[99].

However, from a fabrication point of view, devices for tunneling spectroscopy differ significantly from the encapsulated devices meant for transport measurement in the following aspects:

1. One of the encapsulation h-BN layers, in our case the top layer, needs to be uniform and of appropriate thickness (see 5.3.1). This is because the top layer h-BN layer serves as the tunneling barrier, instead of merely as a protection for graphene. The thickness and uniformity of a tunneling barrier, especially in a planar tunnel junction, has a significant effect on the signal to noise ratio and on the measurement result.

2. Following point 1, the device can not be regarded as fully protected by h-BN, as a large portion of area (80% in our case) is covered by only one or two layers of h-BN, which is far from sufficient to isolate the electrostatic doping induced by contaminants immediately on top. Thus, more implementation needs to be addressed to reach the truly ballistic regime, especially at low carrier density. We will discuss this issue in the following sections, which focus on measurements and perspectives.

3. In order to measure a "strong induced superconducting gap" in graphene, the tunneling probe must be placed as close to the superconducting lead as possible if the 2-DEGS is not purely ballistic[84]. This means that the device must be as compact as possible, but without shorting the probe to the leads.

4. The choice of tunneling probe is crucial. The tunneling probe is isolated from the exact area of the graphene to be probed by ultra-thin h-BN (less than 1nm), which means that doping from the tunneling lead is non-negligible. This is in remarkable contrast to the dual-gated device where the metallic top-gate is tens of nanometers away from the 2-DEGS.

These considerations, as reasonable and obvious as they now appear to be, were recognized sequentially in the course of our endeavor. This section summarizes what we have learned so far about making these kinds of devices. The fabrication of the device currently being measured (as of November 2015) will be discussed in detail. The latest version with significant improvements based on the measurement results so far will also be presented.

### 5.3.1 *Ultra-thin h-BN as a tunneling barrier*

We have demonstrated that h-BN can be used as an ideal substrate as well as a protective over-layer to render a graphene sample with low-disorder. These properties can be attributed to h-BN's ultra-flatness, crystalline structure, and large band gap which makes it insulating up to a few eV in energy scale. Further, h-BN is a single crystal with a low defect density within the area of a typical nanodevice.

These properties make ultra-thin h-BN an attractive candidate for a tunneling barrier for the spectroscopic study of graphene[6] and other Van der Waals heterostructures. Figure 5.3 shows the I-V characteristics of thin (1~4 L) h-BN flakes measured by conductive AFM (C-AFM)[86] and planar electrodes[23]. Both experiments show that the conductance measured between two conductors, separated from each other by h-BN flakes, decreases exponentially with the number of h-BN layers, as expected for electronic transport dominated by a tunneling process. From the planar junction measurement (Fig.5.3(b)), where tunneling is measured between graphite and gold electrodes, the zero-bias conductivity is deduced to be $\sim 1K\Omega^{-1}\mu m^{-2}$ for monolayer h-BN, and decreases to $0.1G\Omega^{-1}\mu m^{-2}$ for 4-L h-BN[23].

Note that the conductivity derived from this type of experiment depends directly on the type of electrodes being used, as the tunneling current is proportional to the density of states on both sides of the barrier as discussed in 5.2.1.

The resistance map obtained by conductive AFM shows only ~10% variation over tens of square micrometers, and the typical breakdown voltage is $\sim 1 volt \cdot nm^{-1}$. These results suggest that thin h-BN is a uniform [2] insulating layer within the typical energy range of tunneling experiments.

### 5.3.2 *Hunting for ultra-thin h-BN and determining the number of layers with Raman spectroscopy*

Choosing the appropriate number of h-BN layers is crucial in our experiment, as the number of layers dictates the signal to noise ratio of the measurement. In a typical aluminum-contacted device, the upper bound of the induced gap is about 150 $\mu eV$. To resolve features within this gap at sufficient resolution, one should expect to use AC excitation (in a standard lock-in measurement) not exceeding 10% of the gap, namely 15 $\mu eV$. In a measurement setup with a $10^{-12}$ ampere noise floor, this means an upper bound of of 15 MΩ for tunneling resistance. For a metal-hBN-graphene tunneling device, similar to that modeled in Figure 5.3(b), this implies that a h-BN tunneling barrier should not exceed 3L. In a real device, the tunneling area is typically $0.15\mu m(L) \times 1\mu m(W)$; therefore the number of layers must be even smaller. Thus, we are restricted to use 1~2L h-BN for an aluminum-contacted device.

The question is: How do we determine the number of layers for ultra-thin h-BN?

---

[2] Uniform but not defect free. The results in ref.[23, 86] are obtained by C-AFM. In planar (2-D to 2-D) tunneling, the effect of defects is prominent as it averages over the whole tunneling region. See, for example, ref. [28], in which an experiment is performed on h-BN from the same source.

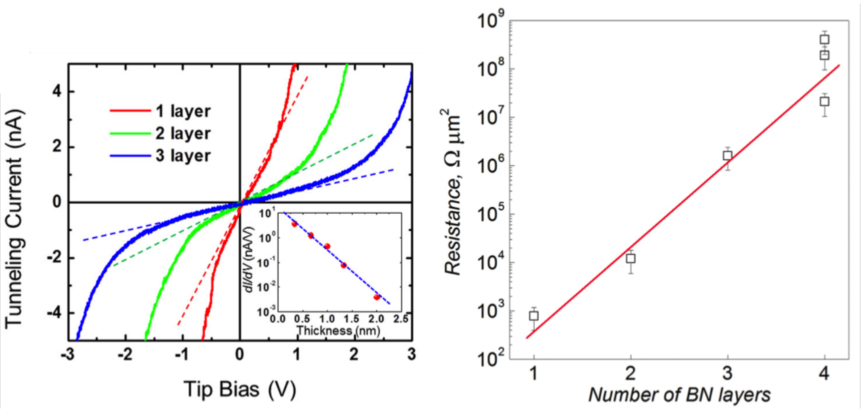

(a) $I - V$ characteristics of h-BN obtained by conductive AFM (image adapted from ref.[86]). Each curve of current shows non-linear dependence on the bias voltage and (inversely to) the number of layers, as expected for the tunneling process.

(b) Zero-bias, area-normalized tunneling resistance of thin h-BN (1L to 4L) sandwiched between the graphite and gold electrodes (image adapted from ref.[23]).

Figure 5.3: h-BN tunneling barrier.

As an insulator with a ~ 5.9eV gap, h-BN deposited on 285 nm-thick $SiO_2$ substrate appears to be much less contrasted than graphene with the same number of layers. Figure 5.4 shows optical images of thin (1L to 3L) h-BN flakes, monolayer graphene(MLG), and bilayer graphene (BLG) on 285 nm-thick $SiO_2$. It is evident that the 3L h-BN is very close to MLG in terms of optical contrast to the background, whereas 2L and 1L h-BN are even fainter. The poor optical contrast of h-BN against the substrate also implies that it is very difficult, if not impossible, to accurately identify the number of layers using an optical microscope. We will see in subsequent sections that we are restricted to using 1L-hBN as a tunneling barrier for aluminum-contacted devices: therefore, exactly determining 1L-hBN becomes the starting point for making our devices.

Also note that although AFM in general has a sub-nanometer vertical resolution and can resolve monolayer h-BN (thickness ~ 300 pm), AFM is not sufficient to determine the number of h-BN layers down to 3L (~1nm thick ) unless the thin flake is deposited on an atomically flat background, such as graphite or h-BN both of which must be thicker than 10 nm. However, the h-BN must be deposited on $SiO_2$ first in order to be picked-up, which is not possible if the flake is on "sticky" h-BN or graphite, and transferred onto graphene to make the device. As we have seen in 4.2.1, the RMS roughness of $SiO_2$ substrate (220 pm) is comparable to the thickness of monolayer h-BN (~300 pm). The local fluctuation of $SiO_2$ surface in height signal is typically 1nm, which completely obscures the distinction between thin layers.

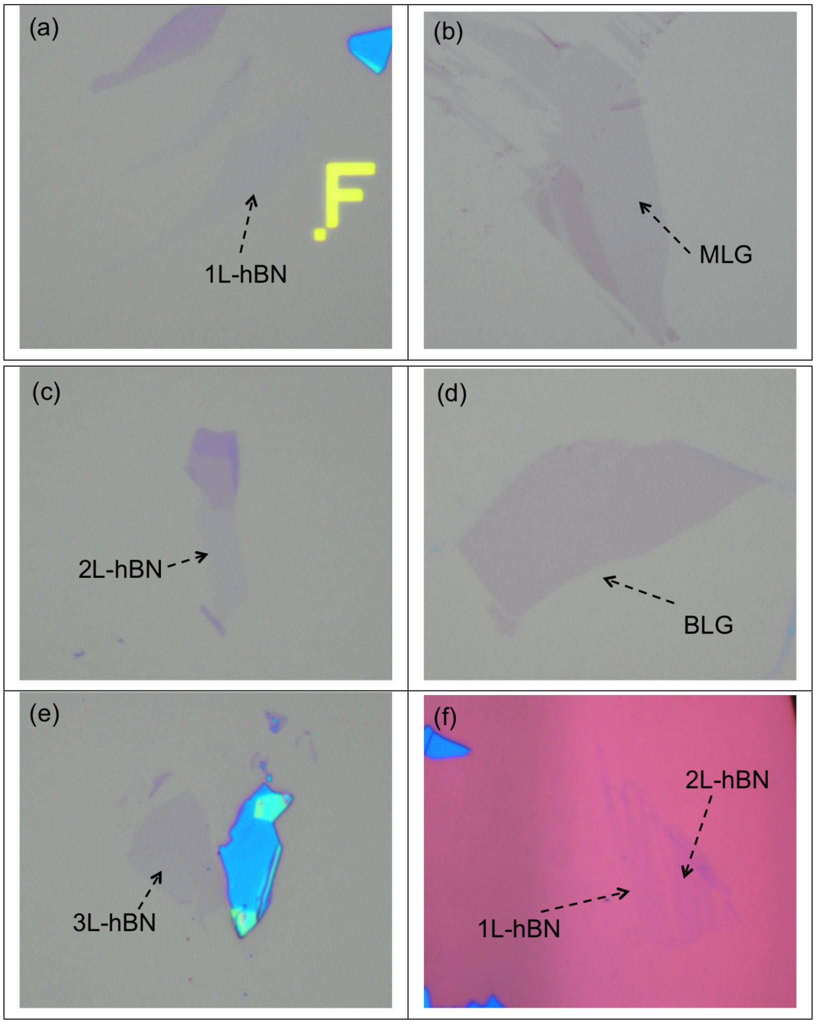

Figure 5.4: Comparison of thin h-BN and graphene with different numbers of layers. Compared with graphene of the same thickness, the h-BN appears much fainter. In our optical setup, 3L-hBN(e) is similar to MLG (b) in terms of contrast. Image (f) shows 1L-hBN and 2L-hBN side-by-side, indicating the difficulty of distinguishing between the two. For the purpose of demonstration, optical images (a) ~ (e) are taken under the same condition of the optical microscope.

#### 5.3.2.1 *Using Raman spectroscopy to determining the number of h-BN layers*

The solution to determining the number of h-BN layers on a $SiO_2$ substrate is to perform Raman spectroscopy on the flake. It has been demonstrated[66] that Raman spectroscopy can reliably identify thin h-BN flakes from a monolayer up to a few layers, beyond which the differentiation is obscured due to saturation, in terms of the position of the Raman peak and the integrated intensity. In particular, with a green laser ($\lambda = 532$nm), bulk h-BN has a Raman peak at 1366 $cm^{-1}$

[3] which shifts to ~ 1369 $cm^{-1}$ when there is only one layer of h-BN, and the integrated intensity decreases linearly with the number of layer $N$. In particular, we have found that, with regard to the setup we used, integrated intensity under the same acquisition conditions is the most reliable parameter for determining the number of h-BN layers on $SiO_2$ substrate.

In practice, Raman spectroscopy setup as a shared facility has significant fluctuations in its signal. We have found that it is not uncommon to obtain very different values of integrated intensity from the same device across sessions separated by a few days or as little as a few hours even when all the controllable parameters are identical. Hence, although capable of differentiating between flakes with different numbers of layers down to $\Delta N = 1$, Raman spectroscopy does not provide the absolute $N$ consistently.

In order to identify the absolute value of $N$ consistently and efficiently before characterizing new samples, we calibrate the Raman signal with respect to a *standard sample* that has h-BN flakes with a definite number of layers. By comparing the signal from new samples to the one obtained from the standard sample, under the same acquisition conditions, we can determine the absolute number of h-BN layers. The result is self-consistent as long as the standard sample and the new sample are measured using identical parameters during one session. In fact, with a standard sample, Raman spectroscopy can be performed consistently across various setups, as is sometimes necessary due to the use of a shared facility.

Figure5.5 shows a typical Raman spectrum of 1L, 2L, and 3L h-BN deposited on a 285 nm $SiO_2$ substrate [4]. Note that in order to exclude probable contributions to the intensity from residues on h-BN (coming from sticky tape), the flakes are thermally annealed in forming gas at 350C for 3 hours before undergoing Raman spectroscopy.

#### 5.3.2.2 *Establishing Raman standard for ultra-thin h-BN*

In our group, the Raman standard h-BN sample is indispensable for anyone who is working on thin h-BN and needs to know the absolute number of layers in the flake. This approach has proved to work consistently in different Raman setups (at Harvard CNS and MIT ISN), for h-BN on either a 90 or 285 nm $SiO_2$ substrate by numerous group members who may use different parameters for the Raman spectroscopy. Figure 5.4 (a) (c) (e) shows images of these standard flakes, each of which has been through hundreds of Raman scanning sessions with no sign of degradation observed (by either Raman or

---

[3] This peak comes from the $E_{2G}$ phono mode and is analogous to the G peak in graphene[66].

[4] At present, we are using 90 nm $SiO_2$ for thin h-BN deposition, as this substrate offers better optical contrast for thin h-BN. However, no change in Raman results has been observed, and we are still using the same reference.

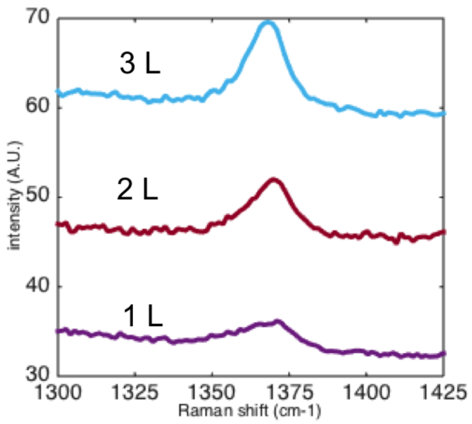

Figure 5.5: Raman spectrum of 1L, 2L, and 3L h-BN deposited on a 285nm $SiO_2$ substrate. The integrated intensity shows dependence on the number of layers.

AFM). Once the first standard sample is made, more can be reproduced by referencing it.

We prepared the standard sample by following this procedure:

1. Mechanically exfoliate h-BN and deposit the flakes onto piranha+HF cleaned (A.1) 285 nm $SiO_2$ substrate.

2. Hunt for flakes with optical microscope. We use 50x objective for h-BN flake hunting in order to increase the probability of finding thin flakes. Take optical images with the same parameters.

3. Categorize images of the flakes according to optical contrast. In our case, only h-BN flakes with L<3 are relevant. Try to find the lowest three levels of contrast recognizable in the optical microscope. Ensure that each category has multiple flakes.

4. Anneal the sample in forming gas ($Ar/H_2$) at $350^oC$ for 3 hours.

5. Perform Raman spectroscopy on each flake in a single session, with 10 sec acquisition time and 15 accumulations for each flake.

6. Categorize the flakes according to the integrated Raman peak intensity of each. This categorization should agree with the sorting in step 3.

7. Prepare an atomically flat surface for the AFM measurement: deposit h-BN on another substrate, select thick (> 15 nm) pieces with a much larger area than any one of the thin h-BN flakes to be determined. Anneal as in step 4, check the homogeneity of hBN surface using AFM.

8. Pick up and transfer (5.3.3) at least one thin flake from each Raman signal category as determined in step 3 onto the thick h-BN substrate. Leave the rest of the thin flakes on the chip, which will eventually become the standard sample.

9. Remove the polymer used for pick-up and transfer in solvent. Anneal the stack as in step 4.

10. Measure the step height of each transferred thin h-BN with respect to the h-BN substrate. Monolayer h-BN should measure ~ 280 pm, with about the same increment size across each extra layer.

11. Establish the correspondence between height (number of layers) information and Raman intensity.

12. The Raman standard sample is made. Keep it with care!

#### 5.3.2.3 *Improving the yield of ultra thin h-BN deposition*

The poor optical contrast of h-BN against $SiO_2$ makes it very difficult to find thin h-BN flakes in what we call the flake hunting practice, namely, scanning the entire chip at high magnification (20X~50X objective). To make the process even more challenging, the h-BN flake has a much lower yield from deposition than does graphene, as the adhesion between h-BN and $SiO_2$ is weaker than that of graphene. Finally, the ultra-thin h-BN flakes are in general much smaller than graphene flakes. This is because h-BN is more brittle than graphene and thus breaks up more easily when subject to mechanical exfoliation with sticky tape.

Empirically, we found that the yield of reasonably-sized (~ 40 $\mu m^2$) thin h-BN flakes can be improved by using the following techniques:

- Perform moderate exfoliation: Exfoliate two to three times with sticky tape to preserve the size of the flakes(Fig. 5.6(a)).

- Deposit on warmed substrate: Heat substrate up to ~ 110C on a hot plate before deposition. This allows uniform adhesion and reduces the number of bubbles trapped between the tape and the substrate (Fig. 5.6(b) (c)).

- Peel the tape from the chip as slowly as possible. Figure 5.6(d) shows a home-made (by Valla Fatemi *et al.*) exfoliation stage (the EXFOLIATRON!) equipped with a micro stepper actuator. This allows the tape to be peeled off in a slow, smooth, and steady way (Fig. 5.6(e)). For ultra-thin h-BN deposition, the speed of the tape motion is ~ 50 $\mu m/sec$.

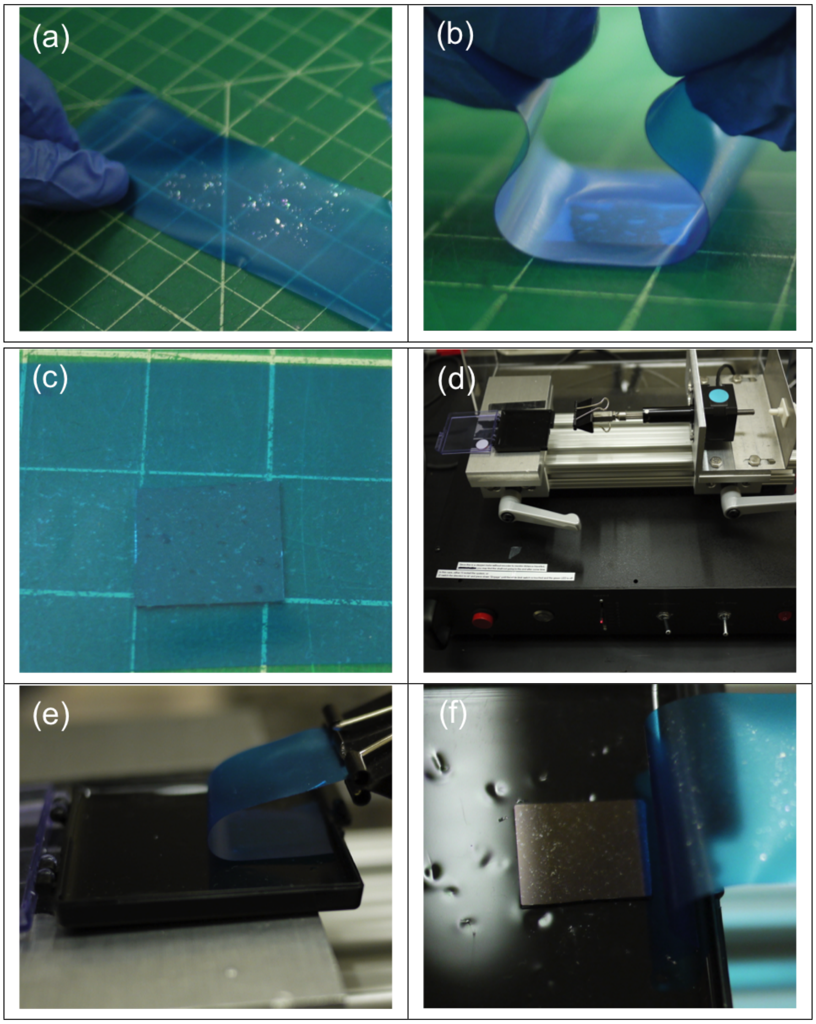

Figure 5.6: Mechanical exfoliation and deposition of ultra-thin h-BN. (a) The tape after two or three exfoliations. The shiny pieces on the tape are thick h-BN crystals. (b) The tape is placed on a warmed chip. The middle of the tape is placed on the chip first and then the rest of the chip is brought into contact with the chip. (c) After 5 minutes of resting, the tape spreads out and adheres to the chip with just a few bubbles trapped between the tape and the chip. (d) The EXFOLIATRON consists of a gel-pad that holds the chip and peels-off the tape with a micro stepper actuator. (e) The tape is peeled off the substrate. (f) h-BN crystals are deposited on a 90 nm $SiO_2$ substrate.

### 5.3.3 *Assembling graphene/h-BN heterostructures for tunneling spectroscopy*

#### 5.3.3.1 *Manipulating ultra-thin h-BN*

Soon after its introduction in 2010 to the field of graphene research, thin h-BN came to be regarded as a promising tunneling barrier. Further, the ability of thin h-BN to function in this way with graphene devices is of particular interest given its high level of compatibility with graphene. On the other hand, the initial transfer method [40, 118] involves depositing graphene or h-BN directly onto a highly-transparent polymer stack. In this scheme, finding thin h-BN with an optical microscope is extremely challenging due to the poor optical contrast given by the thin h-BN. An alternative way is to deposit and locate thin h-BN onto a $SiO_2$ substrate, followed by etching away the substrate in etchants [6]. However, this approach exposes the surface of h-BN to liquids such as etchant, water, and/or solvents. This exposure to liquids inevitably undermines the quality of the final device, as contaminants can become trapped between the h-BN and the graphene.

The pick-up and transfer method for Van der Waals materials developed by Philip Kim's group at Columbia University [42]and also developed independently in our group [31] shed new light on the ways in which these materials can be used. By depositing h-BN on clean $SiO_2$ substrate and picking-up the h-BN flakes with polymer, the dry polymer-based technique allows a h-BN surface to be preserved in a pristine state and brings it in contact with graphene. Although this approach reliably picks up thick h-BN (>5 nm), attempts to pick up atomically thin h-BN with polymers such as *PMMA, MMA* and *PPC* results in very little success.

We started to tackle this issue in early 2014. After trying various kinds of polymers as investigated in the literature [42, 137, 126], we concluded that *PC* (Poly(Bisphenol A) Carbonate, analytical standard, $M_w \sim 28,200$, from *Fluka Analytical*) film on *PDMS* stack is most effective for picking up monolayer h-BN or graphene flakes from a $SiO_2$ substrate. The stronger adhesion of *PC* is responsible for its greater "picking-up power" as compared with that of PMMA or PPC, which allows us to pick up not just thin h-BN or graphene flakes with an appreciable area (~ 10 $\mu m^2$), but also fine graphite nano-rod ($LxW \sim 5\mu m \times 100nm$), which we use as tunneling probes. The robustness of this film also allows us to perform multiple pick-up and transfer iterations in order to make highly complex heterostructures.

Currently, the *PC/PDMS* polymer stack is prepared according to the following procedure:

1. Clean two glass slides with IPA and blow dry with nitrogen.
2. Drop ~5 ml PC solution ( 6% by weight in chloroform) onto one glass slide (Fig. 5.7(a)).
3. Press the other glass slide onto the PC solution and swiftly "smear and glide" this slide across the first glass slide. This process requires practice, but when performed correctly, it will leave a thin PC film on the first glass slide[137]. The film should dry completely in about 1 minute (Fig. 5.7(b),(c)).

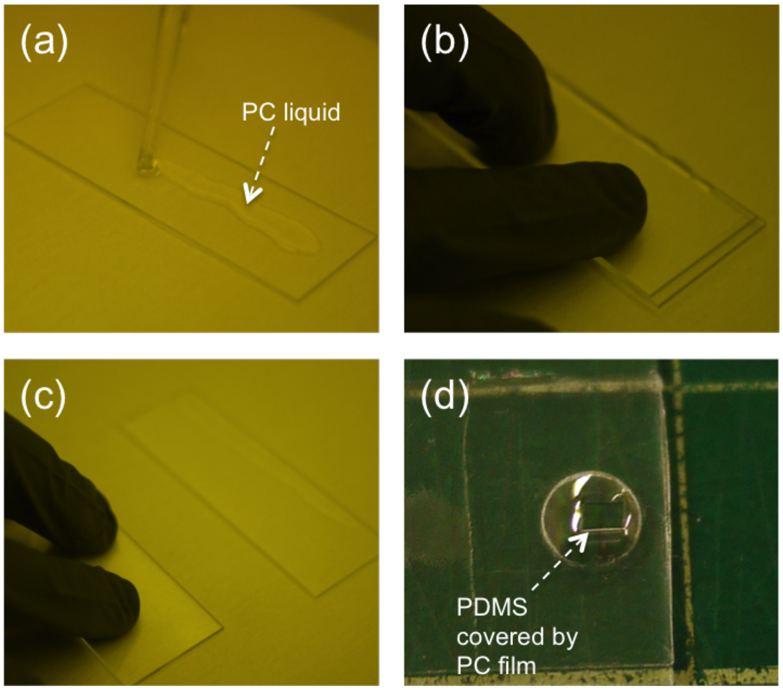

Figure 5.7: Preparation of PC/PDMS polymer stack for picking-up ultra thin h-BN. (a) Drop *PC* liquid onto a clean glass slide. (b) Press and smear the liquid with another glass slide. (c) Slide the tip glass slide over the bottom one swiftly in order to render a uniform film. (d) Use sticky tape to pick up and transfer the PC film onto a PDMS block. Ensure that the film is stretched enough to create a flat surface that conforms to the PDMS.

4. Cut out a piece of PDMS block ($L \times W \times T \sim 2.5\text{mm} \times 2.5\text{mm} \times 1.5\text{mm}$) and place it on another glass slide. Ensure that there are no bubbles between the PDMS and the glass slide. Place double-sided tape around the PDMS block.

5. Punch out a hole with an area larger than that of the PDMS block in step 4 in a piece of double-sided tape. Use this tape to pick up PC film from the glass slide in step 3 [5]. Ensure that the picked-up film remains intact, although it might be rather wrinkled due to the weak support at the edge.

6. Align and center the PDMS block with the circular PC film. Place the PC film on the PDMS, tap around the film with tweezers to ensure that it firmly adheres to the tape around the PDMS. The tension should flatten out the wrinkles in the PC film, thereby resulting in a flat polymer surface (Fig. 5.7(d)).

---

[5] Over time, we have realized that the adhesion between PC film and the glass has a very strong dependence on humidity. During the winter in Cambridge, MA, the film can stick to the glass so firmly that a razor blade is required to peel off the film, and the resultant film is often too strained to be useful.

#### 5.3.3.2 *Pick-up and transfer fine structures with PC/PDMS stack*

The PC/PDMS stack is used to perform multiple pick-up and transfer process. The procedure is basically the same as the one discussed in Chapter 4 (4.3) using the same setup. The only different parameters are the temperatures associated with picking-up and eventually releasing the film onto the bottom stack, as summarized in Table 4.2. Chloroform is the solvent we use to make the PC solution for preparing the films. After the final transfer is complete, the sample is submerged in chloroform for five minutes to dissolve the PC film, followed by rinsing with IPA, and finished with thermal annealing in forming gas.

Figure 5.8 shows one of the devices we made at an earlier stage of this experiment. In this device, the tunneling barrier is made of 2L-hBN that was picked up and transferred onto a graphene/h-BN bottom stack on $SiO_2$. A gold tunneling probe is deposited between the superconducting leads to measure the local density of states. The metal/h-BN/graphene tunneling configuration is similar to the model system shown in Figure 5.3(b). The zero-bias, area-normalized tunneling resistance falls between tens of $K\Omega$ to 150 $K\Omega$, depending on the gate voltage $V_{BG}$. The zero-bias tunneling resistance measured in this device and another one with 3L-hBN in general agrees with the finding in ref. [23]. Further implications associated with this type of device are discussed in the next subsection.

### 5.3.4 *Choice of tunneling probe and tunneling barrier for ABS spectroscopy*

The gate-tunability of graphene allows for the study of physics in either a high density regime or around graphene's charge neutrality point, where density of states essentially diminishes. As discussed in 5.2.2, one of our motivations for studying ABS in a graphene system is because the diminishing density of states around the charge neutrality point may result in isolated Andreev bound states. The ability to address these states independently may lead to a deeper understanding of the proximity effect. A high-quality, low-disorder graphene device is, therefore, required in order to render a measurement that is as close as possible to the charge neutrality point.

In Chapter 4, we show that encapsulating graphene between h-BN flakes is an effective way of obtaining a device of this kind. However, the scenario is not as straightforward as might be expected.

The challenge stems from the local doping of the graphene by the tunneling probe, which is usually made of metal. The transport measurements in Chapter 4 demonstrate that due its proximity to graphene, metallic contact can shift the local chemical potential, regardless of the gate voltage. Even when the metal contact is isolated from the graphene by a relatively thick (>10nm) layer of h-BN, the

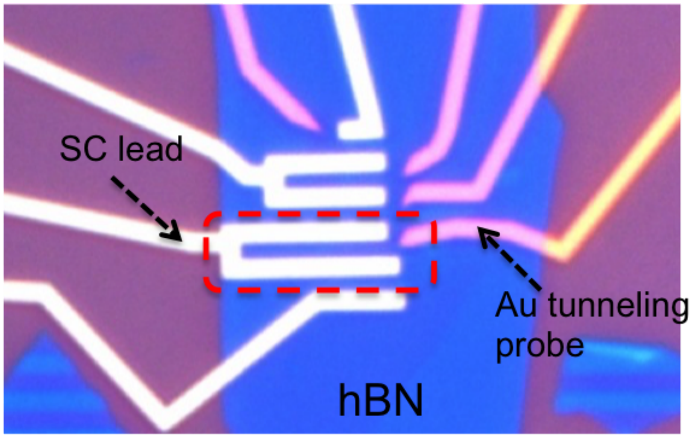

(a) Optical images of a SQUID-like device for tunneling spectroscopy of Andreev bound sates in graphene. The graphene is contacted by Al , whereas the tunneling probe is made of Ti/Au(5nm/30nm), deposited on a 2L-hBN tunneling barrier.

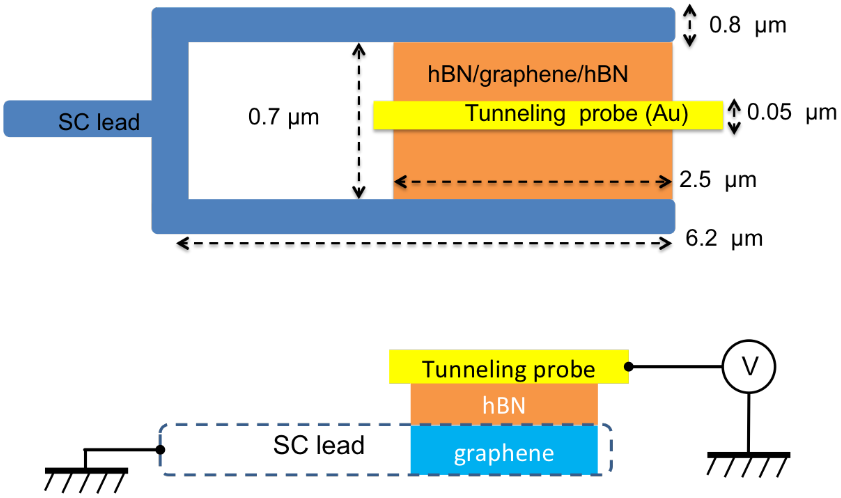

(b) Upper panel:schematic of device with relevant dimensions. Lower panel: measurement configuration for tunneling spectroscopy.

Figure 5.8: SQUID-like tunneling device with a metallic tunneling probe.

shift in electrostatic potential is still pronounced enough to dominate the local chemical potential, within the attainable range of gating. Figure 4.11(a) shows such an effect in the $V_{BG}$= -20V ~ 0V region, where the resistance plateau shows no dependence on the topgate voltage $V_{TG}$ at all.

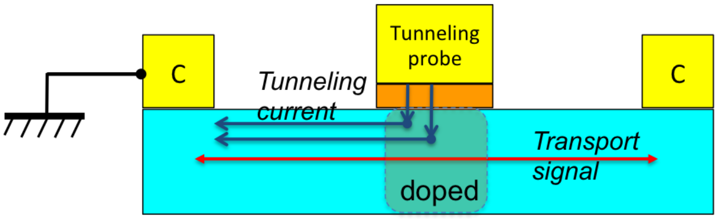

Figure 5.9: Effect of local doping in transport V.S. in tunneling measurements

In a transport measurement, where the overall contribution from the entire device is summed up as the signal, doping from the topgate can be minimized by reducing the area of the locally-gated region. This is not a viable strategy in a tunneling device, as the probe *is* the source of doping, and predominantly measures the locally-doped region (Fig.5.9). Perhaps even more importantly, the tunneling probe must be very close (~ 1nm) to the graphene surface in order to obtain an appreciable tunneling current. The strength of the doping, therefore, is much greater than that from a topgate.

Figure 5.10(a) shows the differential conductance (proportional to the local D.O.S.) obtained by a tunneling measurement performed on the device shown in Figure 5.8. The tunneling probe is a Ti/Au lead deposited on a 2-L h-BN tunneling barrier (thickness ~6Å). The D.O.S. decreases with $V_{BG}$ but never reaches a local minimum within the allowed range of $V_{BG}$ (gate dielectric:15 nm h-BN+285 nm $SiO_2$). This suggests that the region underneath the Au tunneling probe is heavily $p$-doped and and that $V_{CNP} > 50V$.

In Figure 5.10(b) (c), we show the measurement taken on another device, which employs 3-L h-BN (thickness ~ 9Å) as a tunneling barrier and a Ti/Al tunneling probe. Instead of having a SQUID-like configuration, this device is a Josephson junction with a tunneling probe in the middle, similar to the dual-gated Josephson junction discussed in Chapter 4. The configuration of this device makes it possible to perform both tunneling (Fig. 5.10(b)) and transport (Fig. 5.10(c)) measurements across the same junction. The contrast between the two measurements is striking: in the tunneling measurement, $V_{CNP}$, defined by the minimum of D.O.S., appears at ~ -2.5V; in the transport measurement, $V_{CNP}$, defined by the peak of resistance, appears at ~ -0.04V. These measurements imply that the region underneath the tunneling probe is much more strongly $n$-doped than is the entire flake on average [6].

A theoretical calculation based on density function theory [63, 79] shows that doping originates from the difference in work functions between graphene and metal. Figure 5.11 shows the Fermi level shift $\Delta E_F$ as a function of graphene-metal distance for different metals (adapted from ref.[63]). At relevant distances (6Å for Au and 9Å for Al), our observations agrees qualitatively with the theoretical calculation.

As work function mismatch is believed to be the origin of a pronounced Fermi level shift up to hundreds of meV, graphite stands out as the most promising choice for a tunneling probe material [7]. Being almost identical to graphene in regard to work function, the graphite tunneling probe also provides an atomically flat surface that couples to graphene via thin h-BN. Therefore, the graphite tunneling probe can be incorporated into Van der Waals heterostructures without compromising the quality of the device.

Finally, in comparison with a metal/h-BN/graphene system as characterized in Figure 5.3(b), for a graphite/h-BN/graphene tunneling configuration, we expect to measure larger tunneling resistance per unit area. This larger tunneling resistance can be attributed to the fact that graphite has a smaller density of state than metals do[23]. In subsection5.3.2, we estimate that 2L-hBN is suitable for a metal/h-BN/graphene tunneling measurement to have a decent signal to noise ratio. This is confirmed in the measurement performed on the device shown in Figure 5.8.

Thus, in order to obtain signals of similar strength (as from the device shown in Fig. 5.8) using a graphite tunneling probe, we must choose monolayer h-BN as our tunneling barrier. Figure 5.12 shows the device we fabricated to calibrate the tunneling resistance of 1L- and 2L-hBN, each with multiple graphite and aluminum probes. We conclude that the zero-bias resistance in a graphite/1L-hBN/graphite tunneling configuration is about a few tens KΩ per $\mu m^2$ [8].

---

[6] The first device uses a global $Si$ backgate, and the second device uses a local graphite backgate (gate dielectric:10 nm h-BN). Thus, the two devices differ significantly in terms of the range of backgate. Roughly speaking, 1 volt in local backgate is equivalent to 30 volt in global backgate voltage. Therefore, the difference between two $V_{CNP}$'s is equivalent to a 75-volt shift of $V_{CNP}$ in a device on $SiO_2$. We assume that this is of the same order of magnitude as found in the first device, but in opposite polarity. The doping effect is enormous.

[7] In principle, doping can be counter-balanced by applying a large $V_{BG}$, but this inevitably creates $P$-$N$ junctions within the tunneling device. The inhomogeneity thus induced may add unwanted complexity in the measured signal. Also, the Dirac point in the transport data looks much narrower than that obtained in the tunneling measurement, suggesting that a metallic probe not only causes Fermi level shifting, but may also increase local disorder in graphene.

[8] We could only calibrate the order of magnitude of the resistance, as the exact values exhibited a variation up to 50% among all the graphite probes, which might depend on the effective area of tunneling or on local barrier strength. However, the results consistently showed that the graphite tunneling probe yielded larger tunneling resis-

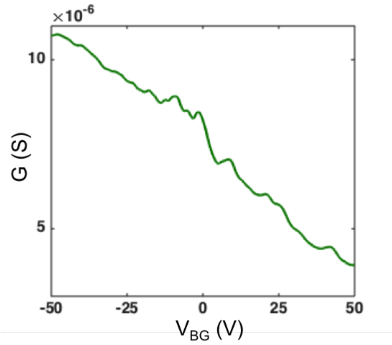

(a) Differential conductance $dI/dV$ versus gate voltage measured in a Au/2L-hBN/graphene tunneling device. $dI/dV$ decreases almost monotonously with $V_{BG}$, showing no local minimum (corresponding to the charge neutrality point) in the allowed range of $V_{BG}$. This measurement suggests that at ~6Å away, the Au probe dopes the graphene into a p-type semiconductor. This observation is consistent with the theoretical prediction based on DFT (Fig. 5.11).

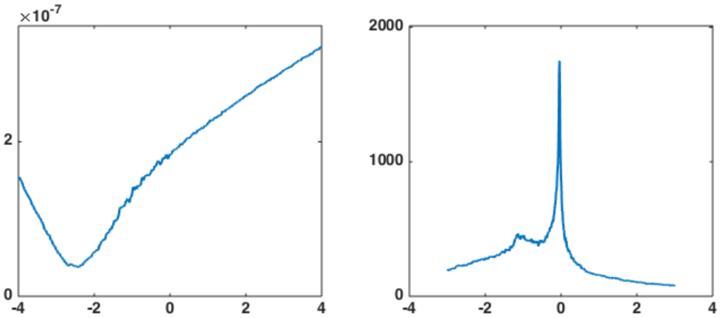

(b) Differential conductance $dI/dV$ versus gate voltage measured in a Al/3L-hBN/graphene tunneling device. $dI/dV$ shows a minimum at $V_{BG} \sim -2.4V$, which is identified as the charge neutrality point of the graphene immediately underneath the probe. This measurement suggests that at ~9Å away, the aluminum probe dopes the graphene into an $n$-type semiconductor. This observation is consistent with the theoretical prediction based on DFT (Fig. 5.11).

(c) Transport measurement of $R$ versus $V_{BG}$ taken from the same device in (b). The two leads positioned on either side of the tunneling probe thus the result includes the overall contribution of the entire flake. In contrast to the tunneling result, the charge neutrality point is very close to zero. This is the case even though the device is still slightly $n$-doped, as can be seen from the shift of $V_{CNP}$ to the left and the resistance plateau in the p-region.

Figure 5.10: Charge neutrality point measured by transport and tunneling measurement.

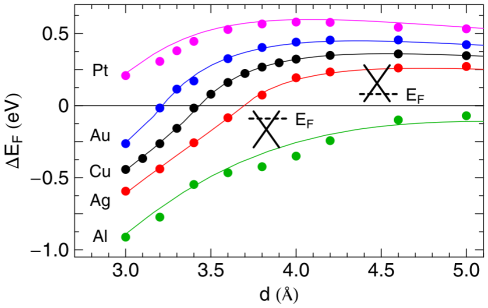

Figure 5.11: Fermi level shift $\Delta E_F$ as a function of graphene-metal distance for different metals, adapted from ref.[63]

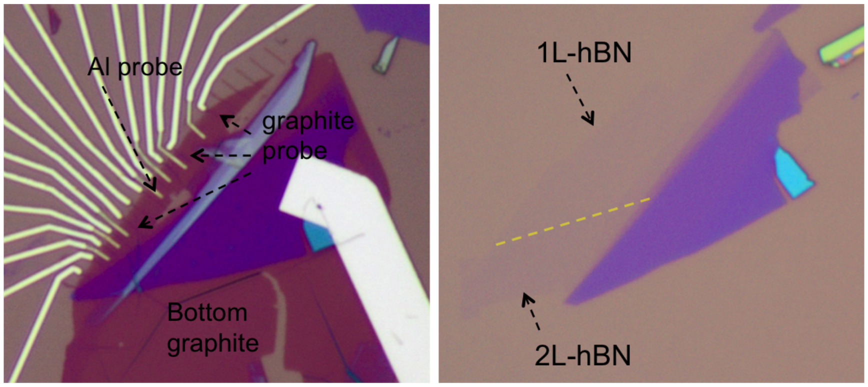

(a) Image of a tunneling device that we fabricated for characterizing tunneling resistance in a graphite/h-BN/graphene system, using the thin h-BN piece shown in (b). Alternating Al and graphite tunneling probes are deposited on both regions in order to tunnel to the graphite underneath.

(b) Ultra thin h-BN flake on a $SiO_2$ substrate before being transferred onto a graphite substrate. Yellow dashed line marks the boundary between the monolayer and bilayer h-BN.

Figure 5.12: Tunneling device made for tunneling resistance calibration.

### 5.3.5 *Making tunneling devices with self-aligned graphite tunneling probe*

Placing a fine graphite tunneling probe in the middle of a Josephson junction, which has an inter-lead distance of ~ 500 nm, seems practically impossible within a typical pick-up and transfer scheme. Therefore, we developed a series of new techniques in order to make a tunneling device with a self-aligned graphite tunneling probe.

---

tance than the metallic probes did. The probes in this calibration sample were of the size and shape we would use for real ABS tunneling. The increase in tunneling resistance is similar in samples (not shown in this thesis) with a much larger tunneling area (~ $6 \mu m^2$).

Figure 5.14 illustrates the procedures we followed to make this type of device. A step-by-step description of the procedures is also given as follows.

Note: Any substrate mentioned below is cleaned by our standard piranha+HF cleaning process in order to preserve a pristine surface that will be in touch with the active area of the device. The pick-up and transfer is carried out with a PC/PDMS stack.

1. Exfoliate graphite and deposit it onto a substrate. Locate homogeneous graphite pieces with area of ~ $15\mu m \times 15\mu m$ and a thickness of 5 ~10 nm.

2. Spin PMMA (950A5, thickness ~300 nm), which will serve as the e-beam lithography resists and as the etch mask. Pattern with e-beam into parallel narrow stripes. The dimensions are typically $L \times W = 150nm \times 5\mu m$ (Fig. 5.13(a)). Note: We always pattern from the edges of the selected graphite flakes in such a way that only three sides of the final graphite nano-probe are exposed to the $O_2$ plasma (RIE) etching. This is extremely important because the $O_2$ plasma tends to "graft" carbon atoms at the edge to the oxide surface very strongly. In our experiments, we found that graphite nano-probes that had been etched all around the edges adhered to the substrate so firmly that they could not be picked up. In fact, we did not succeed in picking up even one graphite nano-probe that had been etched in this way. On the other hand, leaving a short edge (150 nm) that is not exposed to $O_2$ plasma makes it possible to pick-up nano-probes with a reasonable rate of success (> 50 %). This is because the non-exposed edge serves as a "handle" that the PC film can hold-on to in order to start to peel the graphite from the substrate. In a more recent version of the device, we purposely increased the area of this handle, as shown in Figure 5.14, to increase the pick-up success rate.

3. Etch graphite with $O_2$ plasma. The etching is performed via an anisotropic reactive ion etching system. The etching gives a sharp edge with no undercut. Lift-off the PMMA etch mask in acetone followed by IPA rinsing.

4. Pick-up graphite nano-probes and transfer them onto monolayer h-BN as identified with Raman spectroscopy (Fig.5.13(b)).

5. Spin PMMA, pattern with e-beam lithography into the size and shape of a Josephson junction ($L \times W \sim 500nm \times 5\mu m$). This is equivalent to the h-BN mask described in Chapter 4 for encapsulated SGS junctions.

6. Following the same recipe discussed in Chapter 4: Etch the h-BN mask with RIE and remove the PMMA mask in acetone,

followed by IPA rinsing. Anneal in forming gas at $350^o$ C for three hours.

7. Exfoliate graphene and deposit it onto a substrate. We chose narrowly-shaped graphene with diminishing width (Fig.5.13(c)), in order to limit the number of transverse modes. Graphene that is naturally-cleaved has sharp, well-defined edges. This has the advantage of saving an extra round of lithography and etching, and this quality may benefit investigations of edge sensitive modes.

8. Pick up the stack of graphite probe and monolayer h-BN, pick up the graphene flake, and transfer them onto the bottom stack. Remove the PC film in chloroform, rinse with IPA and anneal in forming gas at $500^o$C for at least 3 hours. This annealing is not meant for cleaning, as the graphene is already encapsulated, but rather for smoothing the whole stack. At high temperatures, bubbles trapped between layers of heterostructures can migrate more easily, with a higher chance of escaping from the edge.

9. Perform e-beam patterning and metal deposition, following the recipe described in Chapter 4 for Ti/Al superconducting contacts.

10. Perform PMMA lift-off, after which the sample is ready for measurement.

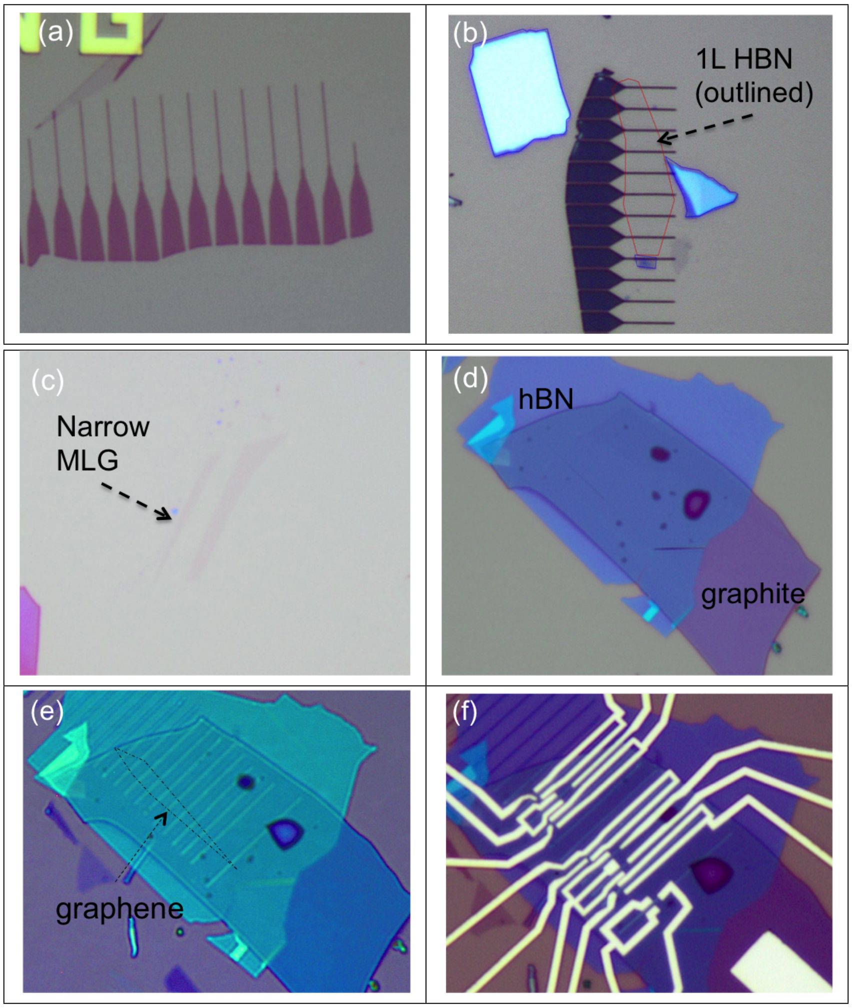

Figure 5.13: Procedures for making a graphene tunneling device with self-aligned graphite tunneling. (a) Graphite tunneling probe made by e-beam lithography and RIE etching. (b) Graphite tunneling probes picked-up and then transferred onto a monolayer h-BN (c) Narrow graphene flakes on a SiO2 substrate. (d) Bottom stack with h-BN and graphite. (e) Full stack of graphite/1L-hBN/graphene/h-BN substrate/graphite backgate. (f) Completed device after Ti/Al deposition and lift-off. Ready for measurement.

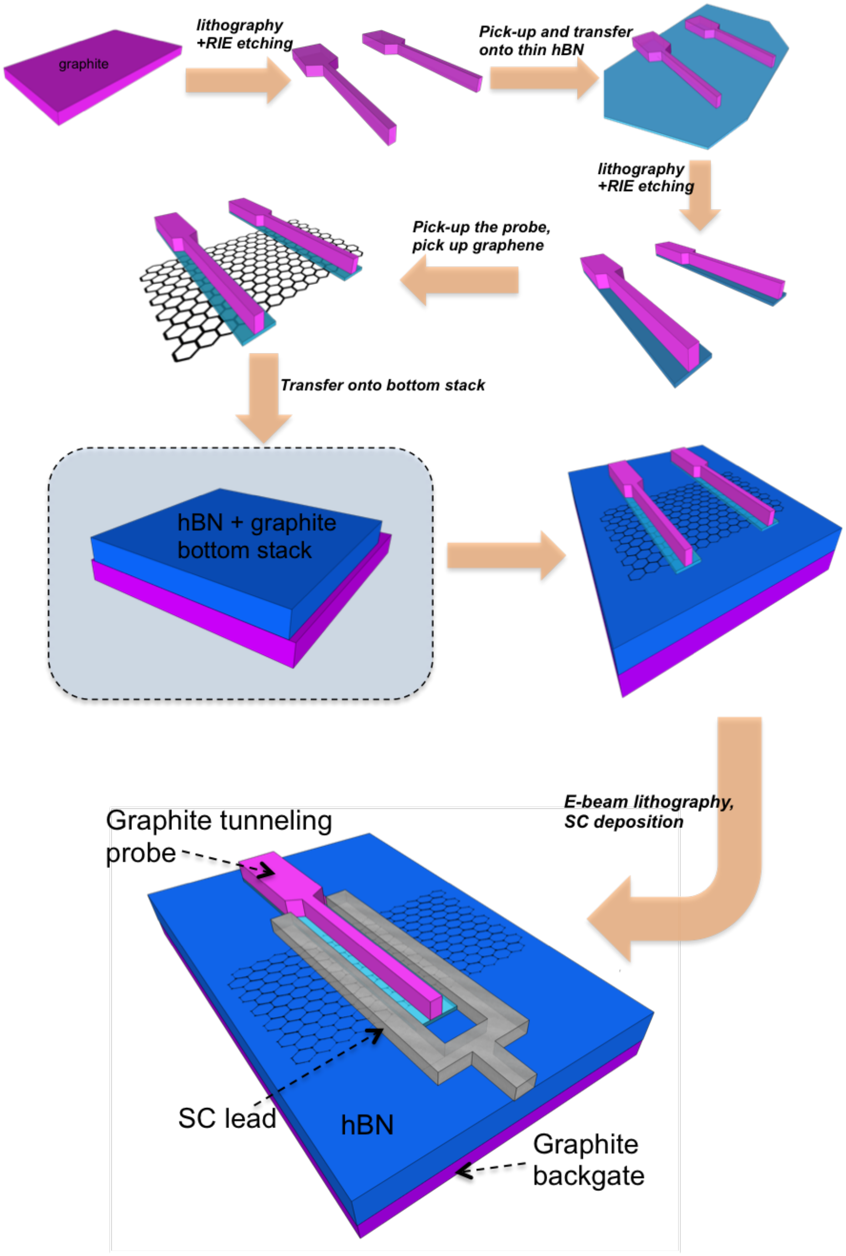

Figure 5.14: Procedures for making a tunneling device with self-aligned graphite tunneling probe

### 5.3.6 *Device structure and geometry*

Figure 5.15 shows the tunneling device for ABS spectroscopy. In particular, we will discuss the measurement from junction A (red dashed line) and junction B (green dashed line) in section 5.5, which is dedicated to measurement results.

In fact, this is the first full device that we constructed by using 1-L h-BN as a tunneling barrier, following the procedure presented in 5.3.5. The materials in these heterostructures, in order from top to bottom, are a graphite tunneling probe → 1L-hBN→MLG→h-BN substrate (~15 nm)→graphite backgate on a SiO2 substrate. AFM images were taken after the completion of the full heterostructures (Fig.5.15(c)). It is evident that the graphite tunneling probes are positioned in the middle of the 1L-hBN tunneling barrier. This mask spans the entire graphene underneath the tunneling barrier, in order to ensure that we are measuring the global signal of the 2-D system. As the graphene is naturally cleaved in exfoliation, the edge is sharp up to the resolution of the AFM. Junction A (red dashed line) appears to be quite flat and uniform; however, ripples and topographic anomalies can be observed in junction B (green dashed line). The dimensions of each junction (the region that overlaps between graphene and the h-BN tunneling barrier) is $L \times W = 500nm \times 700nm$ for junction A, and $L \times W = 500nm \times 2\mu m$ for junction B, whereas *L(tunneling probe)*= 100 nm. Multiple SQUID-like junctions are fabricated in this device. Various SQUID loop sizes and graphene widths allow us to study devices with different $Area_{graphene}/Area_{squid}$ ratios, and the effect of phase gradient in the transverse direction of the junction.

We followed the same recipe presented in Chapter 4(4.5): 7 nm Ti adhesion layer and 70 nm of Al, which was thermally evaporated to make electrical contact to graphene monolayer, tunneling probe, and the graphite backgate.

In principle, the fabrication of this type of device could be simplified by using 1-dimensional edge contact (ref.[127]) for the superconductor. However, for the “development phase” of this type of tunneling device, we decided to start with the long-tested recipe, which consistently provides good superconducting contact, even when it is coupled to very narrow graphene stripes such as in the present case.

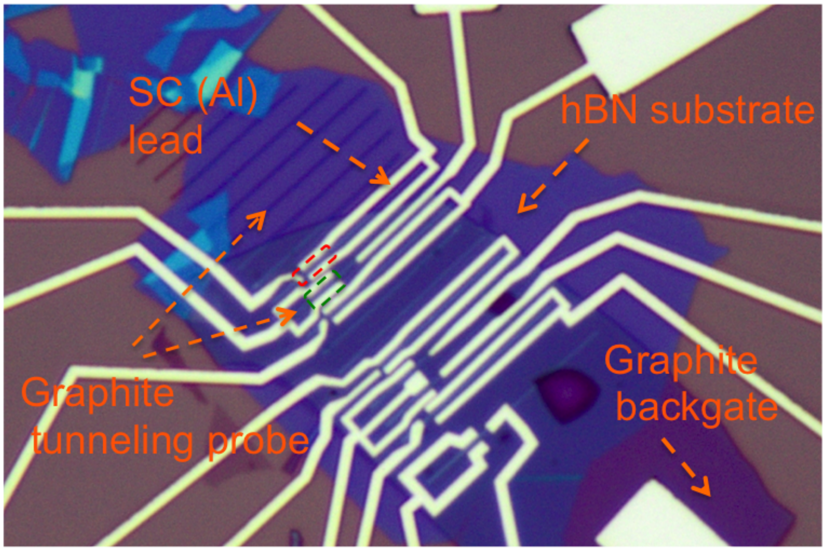

(a) Optical image of device after completion. Measurements taken from junction A (red dashed line) and junction B (green dashed line) are discussed in section 5.5.

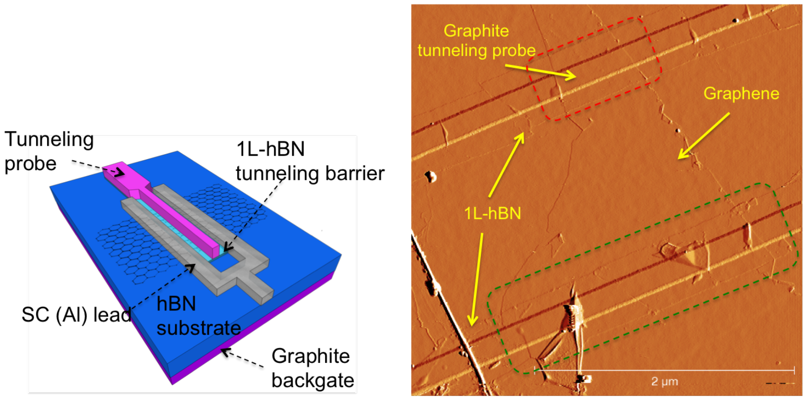

(b) 3-D illustration of ABS spectroscopy device

(c) AFM (amplitude signal) of junction A (red dashed line) and junction B (green dashed line) before Al-contact deposition. The self-aligned graphite tunneling probes are positioned in the middle of the 1L- h-BN tunneling barrier (mask), which spans the entire graphene.

Figure 5.15: Graphene SQUID for ABS spectroscopy.

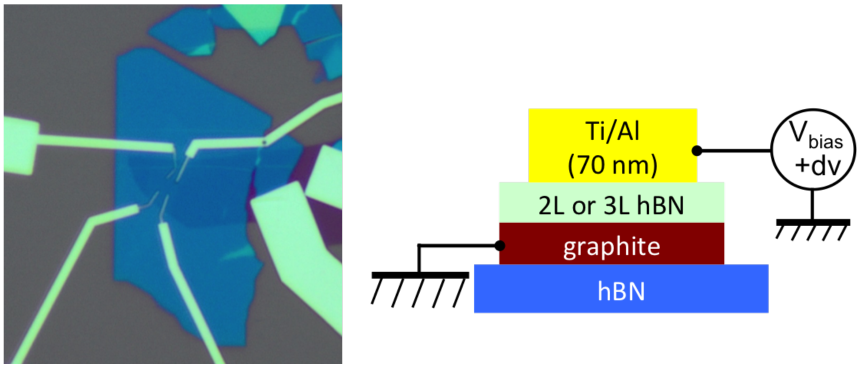

Figure 5.16: Al/h-BN/graphite tunneling device for calibrating the electronic temperature. Four Ti/Al probes are deposited on a 2L-hBN/graphite/h-BN heterostructure.

Before the actual tunneling spectroscopy of proximitized graphene is performed, it is important to validate the feasibility of using graphite and thin h-BN as a tunneling probe and tunneling barrier, respectively. We also need to know the true electronic temperature, as the spectroscopy is a measurement in the energy domain around a relatively small bias range ($\Delta_{Al} \sim 170\mu eV$). Any small fluctuation in voltage induced by thermal noise or magnetic flux picking-up will undermine the energy resolution of the measurement and heat up the device.

To test our assumption, we fabricated tunneling calibration devices, as shown in Figure 5.16. The idea is to tunnel into a BCS superconducting gap with a well-defined temperature dependence[120], in this case the aluminum gap at $T < T_c$, which we then used in subsequent experiments on graphene. By fitting the measured gap to the temperature dependence of the BCS gap in aluminum, we can infer the temperature of the electrons as they enter the device.

For this metal/h-BN/graphite tunneling, 2L- and 3L- h-BN were chosen as the tunneling barrier (see 5.3.4). The device was constructed via the pick-up and transfer method as described previously. Ti/Al (7nm/70 nm) [9] electrodes having the same size and shape as tunneling probes in used actual graphene devices were evaporated on top of the thin h-BN.

Figure 5.17 shows representative results of the characterization: the blue curves are the real measurements, and the green curves are obtained by fitting. We see that by BCS fitting for the 2L-hBN tunneling

---

[9] As we will see later, Al of this thickness yields a gap size that agrees with the theory. In one of the devices for which we evaporated 7 nm Ti but accidentally evaporated only 20 nm of Al, the measured gap was smaller by 40%. This was probably due to the inverse proximity effect from Ti.

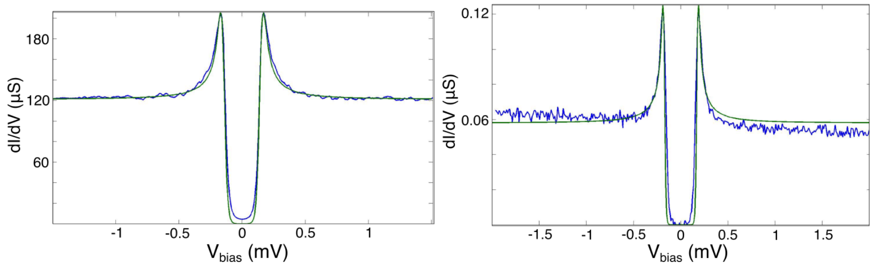

(a) Device with a 2L h-BN tunneling barrier. $\Delta = 142\mu eV$, $T_e = 148mK$, $R_N = 8.26k\Omega$.

(b) Device with a 3L-hBN tunneling barrier. $\Delta = 170\mu eV$, $T_e = 83mK$, $R_N = 17M\Omega$.

Figure 5.17: BCS fitting of the measured Al gap. Blue and green curves plot the measurement data and numerical fitting respectively.

barrier, the normal resistance is $R_N \sim 8.3k\Omega$, the measured gap size is ~142$\mu eV$, and the electronic temperature is $T_e \sim$ 148mK . For the device using 3L-hBN ($R_N \sim 17M\Omega$), the measured gap size is about 170$\mu eV$, and the electron temperature is $T_e \sim$ 83mK.

The deduced value of $T_e$ is in striking contrast to the base temperature measured by the thermometry coupled directly to the mixing chamber ($T_{MC} \sim$ 17mK). This result suggests that there is room for improvement with regard to electronic thermalization and noise filtering.

$T_e$ measured in 3L-hBN devices is generally lower than that obtained in 2L-hBN devices. This is attributed to the much larger $R_N$ in the latter, which can contribute to RC filtering. All 2L-hBN devices show finite zero-bias differential conductance, i.e., non-zero density of states in the superconducting gap, which may suggest the existence of pin-holes or leakage in h-BN at this thickness.

Finally, differential conductance measured above the gap appears to be fairly constant [10]up to ~ $10\Delta_{Al}$, suggesting that graphite is an appropriate tunneling probe.

## 5.5 MEASUREMENT RESULTS

We present major tunneling measurement results in normal and superconducting regimes, with greater emphasis on the latter, in this section. All measurements are taken in the cryo-free dilution refrigerator at base temperature ~ 20 mK. All DC measurement lines are filtered by multi-stage, low-pass filters as discussed in chapter 3 and chapter 4. Without the loss of generality, discussion will focus on the data taken from junction-B, which is more investigated in the time being.

---

[10] A small finite slope is observed in some of the test devices, such as the one shown in Fig. 5.17(b), which may have arisen from the graphite density of states. However, for measurements taken within a few $\Delta$ bias range, the slope can be regarded as negligible.

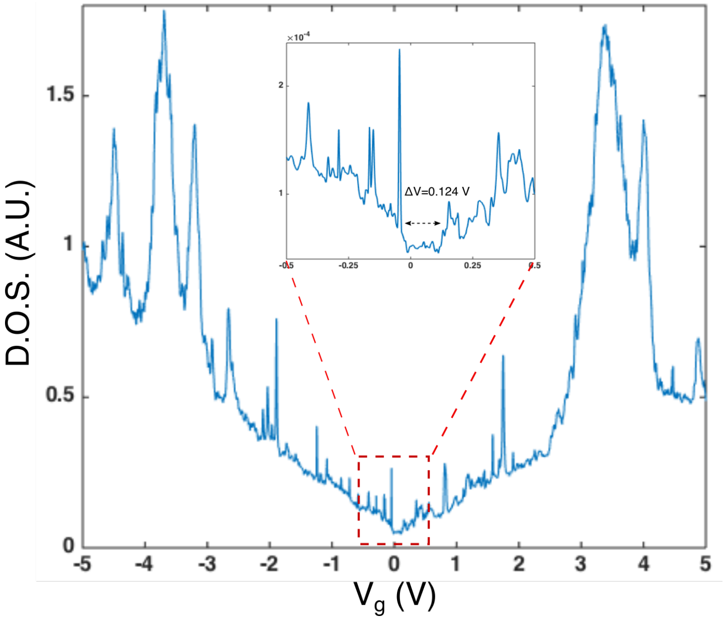

Figure 5.18: *dI/dV* (proportional to density of states) versus $V_g$. In contrast to previous samples made with a metallic probe, the minimum dI/dV, corresponding to the charge neutrality point, is located close to zero gate voltage. Two giant peaks, one at $V_g \sim -3.7V$ and the other at $V_g \sim 3.5V$, accompanied by smaller peaks are observed.

### 5.5.1 *Characterization in normal state*

Figure 5.18 shows the $dI/dV$, a quantity that is proportional to the density of states (D.O.S.), measured as a function of gate voltage $V_g$. The overall shape of the D.O.S. versus $V_g$ is close to the theoretical calculation based on tight-binding models [27]. Minimum D.O.S. occurs close to zero gate voltage with a shift of ~0.045 volts. Around the minimum, D.O.S. does not diminish progressively but flattens out at $n \sim 1.2 \times 10^{11} cm^{-2}$ (inset in Fig.5.18), corresponding to a broadening, to an extent of $\triangle E_F = 40$ meV, of Fermi energy at the Dirac point. The onset density of flattening implies a comparable density of impurities, around which electron-hole puddles build up [89, 6].

Resonant peaks in D.O.S. are observed within the full gate voltage range, $V_{g-max} = \pm 5V$ and $n_{max} \sim 9 \times 10^{12} cm^{-2}$. Two giant peaks appear nearly symmetrically about the Dirac point at $V_g = -3.7V$ and $V_g = 3.5V$, which are assumed to be different in terms of origin from the much weaker satellite peaks due to the contrast in magnitude. The origin of these giant peaks requires more investigation, for example, under a strong magnetic field. However, we notice that they are reminiscent of the Van Hove singularity (VHS), as observed by STM measurement reported in Ref. [87], where a small twist angle between two graphene creates satellite Dirac points that hybridize with the main Dirac point and form saddle point region in D.O.S. (the Van Hove singularity) at a much lower energy than in an isolated (not coupled to any other crystal) graphene.

The resonance peaks of smaller magnitudes are attributed to parasitic quantum dots formed in the path of the tunneling current, which may originate from the disorder in graphene or from defects in the h-BN tunneling barrier[28].

The normal state measurement demonstrates the improvement of our tunneling device, which shows typical characteristics of graphene D.O.S. and a charge neutrality point with a small shift from zero gate voltage. Also, the peak broadening is much smaller in comparison with the measurement shown in Figure 5.10(b).

### 5.5.2 *Measuring induced superconducting gap in graphene as a function of phase*

In this subsection, we discuss measurements at small biases with the presence of a perpendicular magnetic field $B$. The associated energy range is about $\pm 500 \mu eV$, covering at least $3\Delta_{Al}$ in positive and negative energy. The differential conductance $dI/dV$ is measured by a standard lock-in technique with a voltage modulation $dV = 10\mu V$.

Figure 5.19(a) shows the schematics of junction-$B$ that we will discuss in this section. The device is a superconducting ring interrupted by a graphene weak link (Fig. 5.19(c)). In Chapter 2 (2.2.3), we discussed the phase drop across the weak link that can be related to flux penetrating the loop as

$$\phi = -\frac{2\pi\Phi}{\Phi_0} = -\frac{2\pi B \cdot Area}{\Phi_0}.$$

Thus, by varying the B-field, we can twist the phase across the weak link, which is a graphene-based Josephson junction with a tunneling probe, and modulate the Andreev bound state energy by

$$E^{\pm}_{A,L\ll\xi} = \pm\Delta\sqrt{1 - \tau sin^2(\frac{\phi}{2})}, \tag{5.8}$$

where $\tau$ is the transmission probability of the supercurrent carriers.

The Al-enclosed loop area is $\sim 5.9\mu m^2$, and the graphene area is $\sim 1.88\mu m^2$ . The magnetic field corresponding to one flux quantum $\Phi_0$ is $B_{\Phi_0} = \frac{2.067\times10^{-15}(webers)}{5.9\times10^{-12}(m^2)} \sim 0.35mT$.

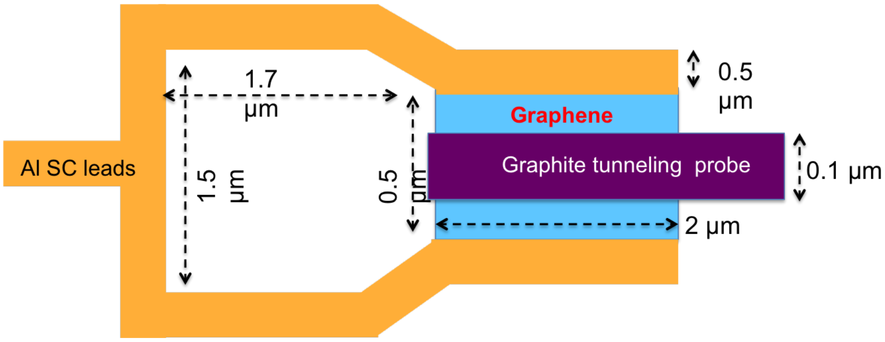

(a) Schematic of junction B (not to scale), showing the relevant dimensions of the device.

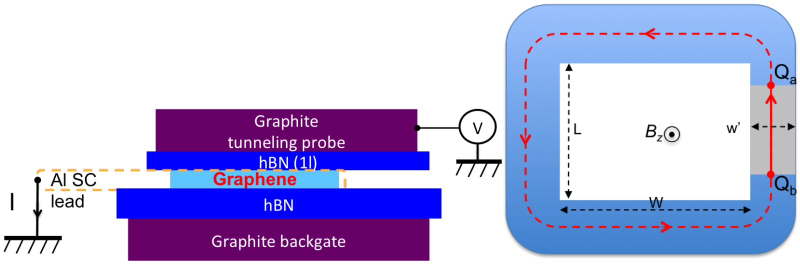

(b) Schematic of tunneling measurement of a graphite/h-BN/graphene/h-BN/graphite heterostructure

(c) A squid-like superconducting loop interrupted by a graphene weak link (2.2.3), on which tunneling spectroscopy is performed to probe the Andreev bound state modulated by varying magnetic flux.

Figure 5.19: Illustrations of device (junction B) geometry and measurement configuration

#### 5.5.2.1 *Phase-modulated induced superconducting gap in graphene*

Figure 5.20(a) shows $dI/dV$ measured as a function of bias voltage $V_b$ and magnetic field $B$. A dip centered around $V_b = 50\mu V$ is observed and $dI/dV$ increases on both sides until two peaks, one at $V_b = -110\mu V$ and the other at $201\mu V$ are reached [11]. From the color plot, we can see that the pattern oscillates with a periodicity of ~ 350 $\mu T$, which agrees with the estimated $B_{\Phi_0}$ within an accuracy of 10%. The agreement indicates that the oscillation is precisely phase dependent along the superconducting loop. Figure 5.20(b) plots line-cuts of the color map within the dashed-line region, corresponding to half of the period.

We attribute the dip in $dI/dV$ to the induced superconducting gap[84, 101] in graphene. The line-cuts in Figure 5.20(b) show a typical soft-gap profile in a proximitized normal metal, with two peaks separated by ~ 311 $\mu V$, corresponding to an induced gap size of $\Delta$~ 155 $\mu eV$, close to the aluminum gap that we characterize in 5.4. In

---

[11] There is a voltage offset consistently in our measurement setup.

order to emphasize the phase modulation, we subtract the average along the vertical $B$-axis at each bias voltage from the entire color plot and re-plot it in Figure 5.20(c). The averaged-background subtracted color plot shows the oscillation with the flux even more vividly. The oscillation of the induced gap is observed within the gap range; however, the oscillatory patterns above the gap can be seen more clearly. The out of gap oscillation will be discussed in 5.5.3.

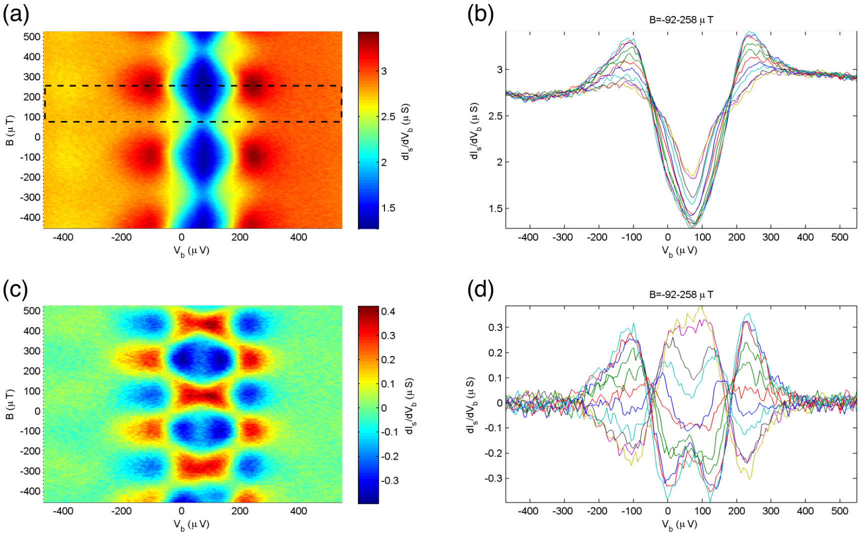

Figure 5.20: Density of states modulated by the perpendicular magnetic field, measured at $Vg$=0.89 V. (a) A typical 2-D scan of $dI/dV$ measured as a function of $B$ and $V_b$. A dip in dI/dV is observed in a range corresponding to the superconducting gap of aluminum, and oscillates with a periodicity equal to the flux quantum. (b) The line-cuts of the $dI/dV$ color plot, which cover half of the period of the oscillation (enclosed by dashed line in (a). (c) Same measurement with averaged background subtracted. Oscillation of signal above the aluminum gap is observed more clearly. (d) Line-cuts of (c), which cover half of the period of the oscillation (enclosed by dashed line in (a).

The phase dependence of the induced gap that we measure agrees qualitatively with eqn. (5.8) , provided that the transmission probability is less than unity, as the gap does not vanish completely at $\phi = \pi$. To further understand the measured oscillation, three line cuts along the B-axis are taken at $V_b = -112, 206$ and $50\mu V$ , which correspond to the two divergence points and the center of the gap (Fig. 5.21(a)), repsectively. The $dI/dV$ curves against $B$ are plotted in figure 5.21(b), which clearly shows a $\pi - shift$ between the divergence point (red and blue curves) and the gap (green curve) oscillation. We interpret this out-of-phase behavior, in light of eqn.(5.8), as a collective motion of multiple Andreev bound states inside the gap: at $\phi = 0$, most of the ABS's are located at the gap edge where D.O.S. peaks, whereas at $\phi = \pi$, the Andreev energies $E_A's$ decrease to their minimum value

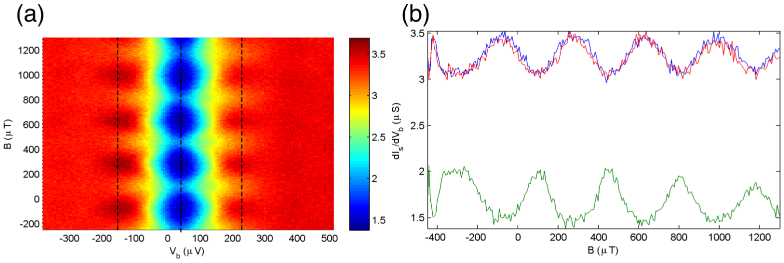

Figure 5.21: $\pi - shift$ between the gap and the divergence peak oscillations. (a) A typical dI/dV map taken at $V_g = -0.8V$. Three dashed lines indicate the location of the line-cuts. (b) Line cut of $dI/dV$ along the $B$-axis. Upper (red and blue) plots are taken at $V_b = -112\ \mu V$ and $206\ \mu V$ where the divergence in $dI/dV$ appears. The green line at the bottom is take in the middle of gap. The upper and lower plots are compensating perfectly to each other, as expected for Andreev bounds states.

and the Andreev bound states move from the gap-edge to the middle of the gap, as indicated by the increase in D.O.S..

Note that although we refer to the short junction limit of ABS (eqn. (5.8)) to qualitatively explain our data, as well as to demonstrate the existence of Andreev bound states, we do not observe purely short-junction behavior in any of the devices we have measured so far. The non-vanishing, compared to the "base-line" obtained by the calibration measurements (see 5.4), density of states inside that gap at all fields suggests that the gap is filled with Andreev bound sates whose $E_A's$ span the full spectrum within the gap. These Andreev bound states can be regarded effectively as contributed by a set of long junction modes, whose origin may be the weak coupling between graphene and the superconductor, impurity scattering within the normal region, and low-energy transverse modes.

### 5.5.2.2 *Andreev bound states that couples strongly to superconductor and the complete closing of the induced gap*

Even though the gap is filled with a mixture of numerous short and long Andreev modes, it is still possible to observe Andreev bound states explicitly associated with a short ballistic junction.

Figure 5.22 shows the measurement taken at $V_g = 2.4$ ($n_e = 4.5 \times 10^{12} cm^{-2}$), where the gap closes almost completely at $\phi = \pi$. In the line-cut shown in Figure 5.22(b), we can see clearly the filling of the gap, which suggests that the modes that contribute to the observable oscillation at this point have $\tau \sim 1$. Note that $\tau$is a generic parameter that describes the overall transmission probability across the Josephson junction [10]. The enhancement of $\tau$may be attributed to various causes such as the screening of impurity scattering at high carrier density, stronger coupling between the channel and superconductor, and/or the gate dependent contact resistance of graphene[132].

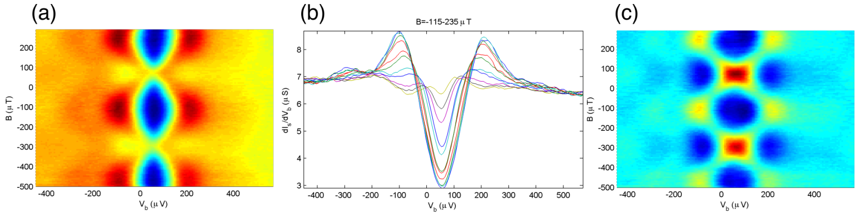

Figure 5.22: Complete closing of the induced gap at $\phi = \pi$. The closing is an indication that coupling strength $\tau$is close to unity.

### 5.5.2.3 *Difference in p- and n-doped regions*

In Chapter 4, we see the effect of contact doping and the effect of P-N junctions on the size of the maximum supercurrent that the device is able to sustain. In general, aluminum-based *SGS* is $n$-doped by contacts, so a suppression of $I_C$ is always observed when the flake is gated to a $p$-type semiconductor. The built-in P-N-P junctions in the device introduce stronger scattering and a lower probability of transmission, which results in a larger effective length since the particle must make multiple attempts (probabilistically) to enter the weak link[10].

We can see signs that are consistent with this model by performing Andreev spectroscopy in the n-doped and p-doped regions with comparable carrier densities. Figure 5.23 shows two representative plots of gaps measured for this comparison. In general we observe that the gaps are sharper and narrower in the p-doped region than in the n-doped region.

The narrower gap corresponds to a set of lower $E_A$, and suggests that the behavior of the junction is closer to that in the long-junction limit, compared to when the device is operated in the n-doped regime.

### 5.5.2.4 *Andreev spectroscopy near the charge neutrality point: the disappearance of phase modulation*

One of the motivations for this experiment is to study the Andreev bound states in graphene around the Dirac point, where the small number of transverse modes allows for the isolated Andreev bound states instead of an "Andreev energy band".

However, as we measure the phase-dependent gap oscillation progressively toward the Dirac point, in the $V_g = 0 \sim 0.1V$ region where $dI/dV$ flattens out (Fig. 5.18), we observe that the modulation becomes weaker and weaker and disappears entirely at around $V_g = 0.15V \sim 0.2V$ (Fig.5.26 ). The oscillation revives after $V_g = 0.3V$ and returns to the normal oscillation that we typically observe.

Figure 5.24 shows the progression of the phase-dependent oscillation versus various gate voltages that span from p-doped to n-doped regimes. The suppression of oscillation is observed from $V_g =$

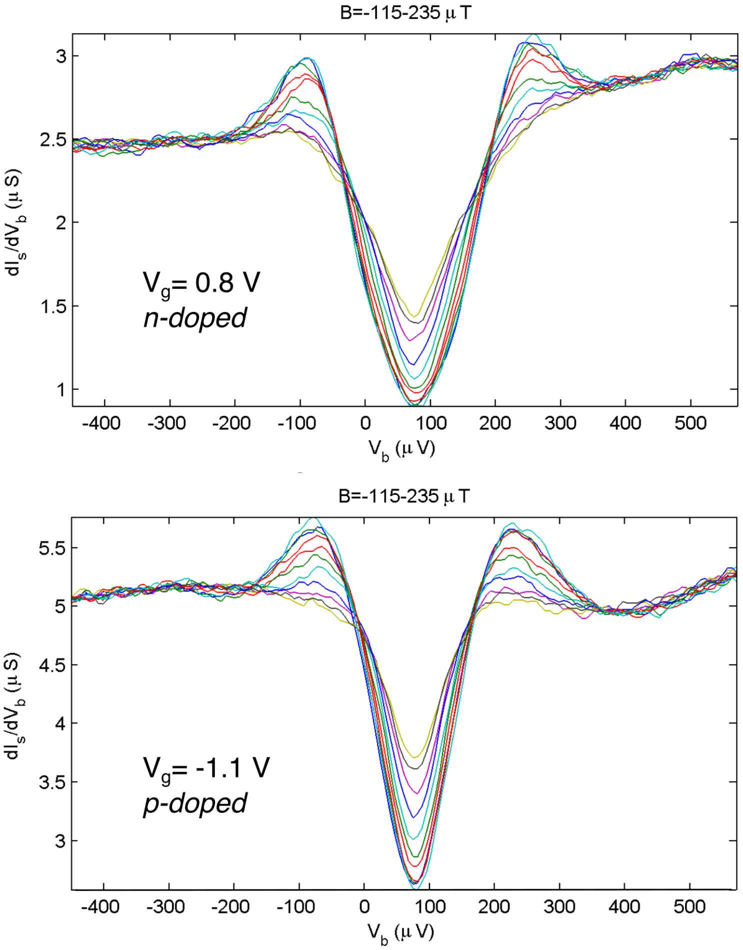

Figure 5.23: Comparison of the induced gap in the n- and p-doped regions. The gap in the n-region is generally wider than that in p-region, suggesting a higher $E_A$ in the n-doped region.

$0 \sim 0.15V$. Figure 5.25 shows the same set of data with an averaged background removed from the color maps. Consistently, the typical checker-board pattern becomes blurry in $V_g = 0 \sim 0.15V$.

The suppression of oscillation can be attributed to the diminishing number of strongly-coupled ($\tau \sim 1$) Andreev bound states in the low density regime. Note that the densities where oscillation is suppressed overlap significantly with the density window where $dI/dV$ flattens out (fig.5.18). Microscopically, when the charge carrier density is lowered to a level that is comparable to the density of electron-hole puddles, the charge carriers are expected scatter more with the impurities before completing the transport. Therefore, the transmission probability $\tau$ becomes smaller, and the phase dependence of the gap is substantially suppressed.

This picture also implies that in order to observe an isolated Andreev mode within the gap, we need to further improve the quality of the samples. We will address this point in the final section.

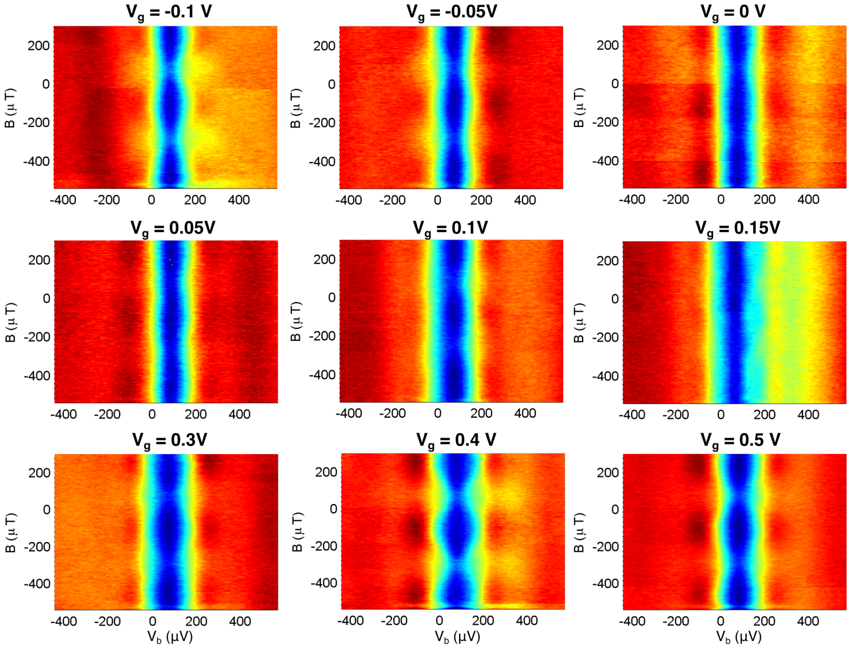

Figure 5.24: ABS measured around the Dirac point. The oscillation damps out progressively as the gate voltage moves toward the flattened-out region of $dI/dV$ ($V_g = 0 \sim 0.1V$) and revives again with pronounced oscillations

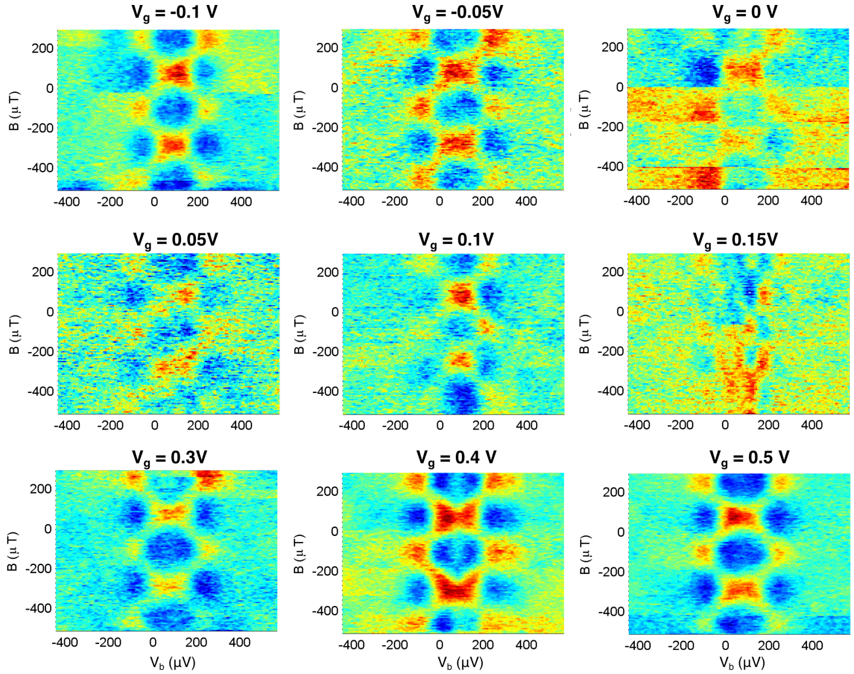
$V_g$ = -0.1 V

$V_g$ = -0.05V

$V_g$ = 0 V

$V_g$ = 0.05V

$V_g$ = 0.1V

$V_g$ = 0.15V

$V_g$ = 0.3V

$V_g$ = 0.4 V

$V_g$ = 0.5 V

Figure 5.25: ABS measured around the Dirac point with averaged background subtracted. The modulation pattern is smeared-out progressively as the gate voltage moves toward the flattened-out region of *dI/dV* ($V_g = 0 \sim 0.1V$) and becomes vivid again.

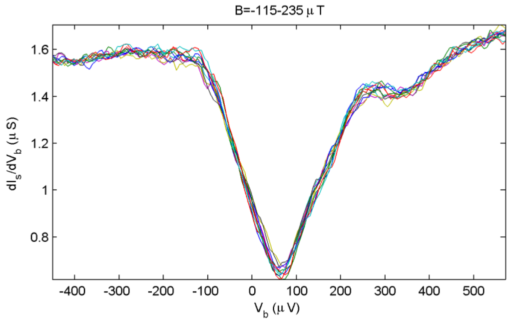
B=-115-235 μT

Figure 5.26: Line-cut at $V_g = 0.2V$, showing complete suppression of phase-dependent modulation.

### 5.5.2.5 *Andreev spectroscopy at high carrier density*

Figure 5.27 shows the Andreev spectroscopy at the opposite limit of the carrier density. Measurements at three high-density points in the n-doped region are presented. We see that the Andreev bound states at point *C*, which is near the peak of the giant resonance, differs from the other two points [12] significantly. The same results (not shown) are

---

[12] Although the 2-D *dI/dV* plots look different at point A and point B, they seem to be of the same nature as can be seen from the subtracted map (rightmost panel).

observed in the p-doped region. This anomaly is still under investigation.

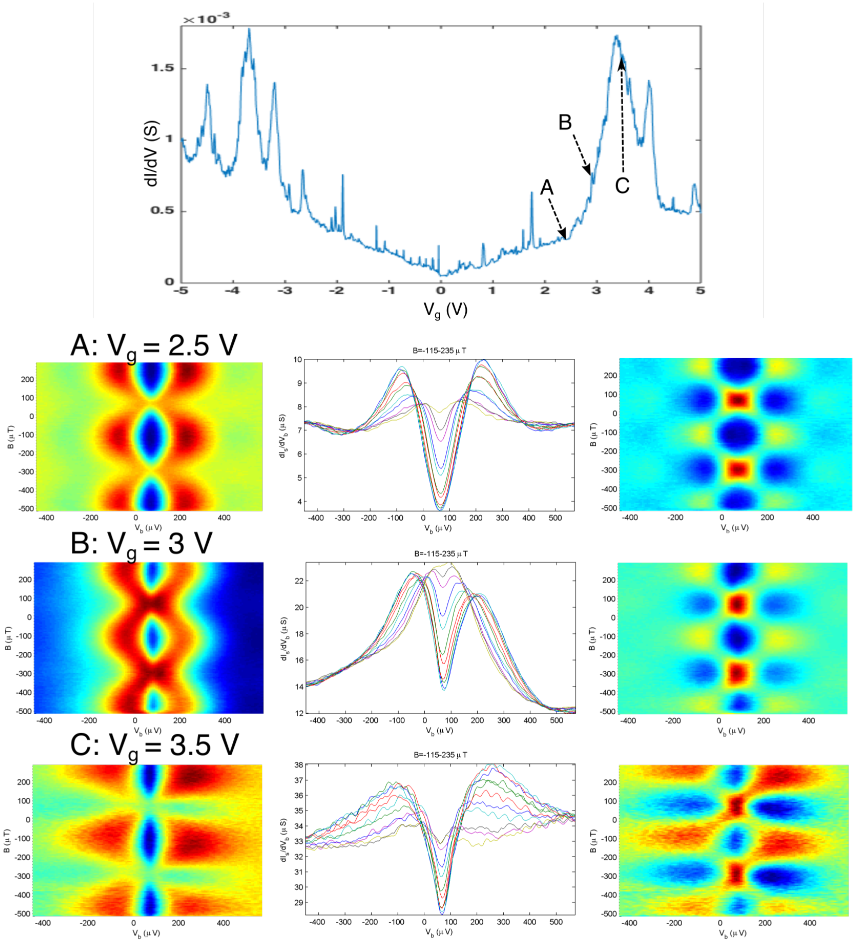

Figure 5.27: Andreev spectroscopy performed in a high carrier density regime. Measurements are performed at three distinct points around the giant resonance peak. The induced gap is superimposed on top of a large density of state at each point. The Andreev bound state measured at point *C* looks strikingly different in raw data and the background-subtracted map

### 5.5.3 *Observation of Andreev scattering sates and strong coupling above the superconducting gap*

One of the most striking features we have observed so far in the Andreev spectroscopy is a periodic pattern that occurs above the superconducting gap (Fig. 5.28). This pattern is readily seen in the $dI/dV$ map, but is even more evident when the background is removed. Along the $B$-axis, the out-of-gap pattern oscillates in phase at the same periodicity as do the Andreev bound states within the gap. Along the $V_b$-axis, the periodicity is $\sim 2\Delta$. This oscillation is ubiqui-

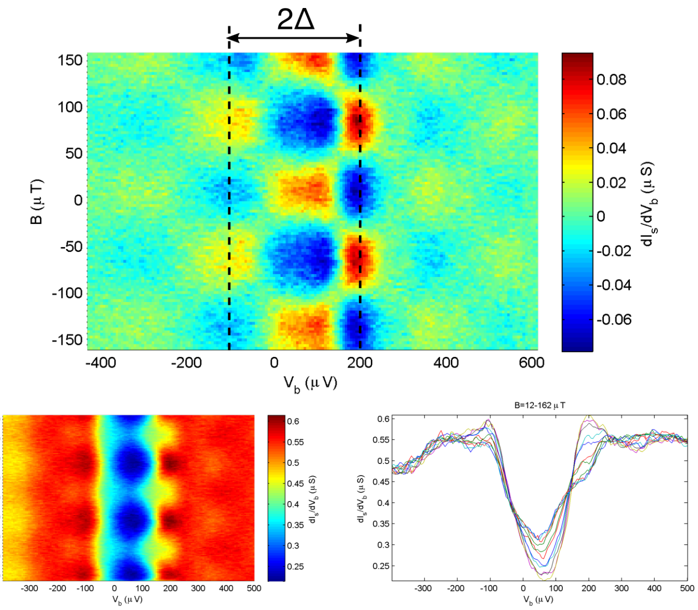

Figure 5.28: ABS scattering state above the superconducting gap. Top panel:background-removed $dI/dV$ measurement as a function of $B$ and $V_g$. Lower left panel: raw data of $dI/dV$ map. Lower right panel: line-cuts in the half flux period.Note that this data is measured from junction-A.

tous in our measurements with varying contrast and extends to at least 3Δ in energy.

The fact that this "checker-board" pattern is modulated by the macroscopic phase of the superconductor and is quantized in Δ on the $V_b$-axis implies that it is the oscillation of the energy continuum above the superconducting gap. This energy continuum consists of the solutions to the Bogoliubov-de-Gennes equation with eigen-energy larger than the superconducting gap ($|E| > \Delta$). The Andreev continuum also contributes to the transport of the supercurrent, but is negligible in the short junction limit ($L \ll \xi_0$)[10].

Unlike Andreev levels with $|E| < \Delta$ , which are localized in the weak link, the Andreev continuum can be regarded aa "leaky" Andreev bound states[12, 10]. At $|E| > \Delta$, the electron or hole composing the Andreev bound state has a finite probability of escaping from the junction by transmitting over the superconducting gap. Therefore the particle is no longer bounded by the gap, but merely scatters coherently with the pairing potential instead.

It is still unclear to us why these *Andreev scattering states* are so evident in the tunneling spectroscopy of supercurrent-carrying graphene. One possible explanation is that some of the scattering states couple strongly to the superconductor, so that their oscillation with the phase becomes more evident than others.

We have seen that the Andreev continuum exhibits phase-dependent oscillation at an energy scale that is close to the gap. This suggests that particles with energy slightly above the superconducting gap can still scatter with the pairing potential Δ, and remain its phase coherence to some extent.

The top panel in Figure 5.29 shows such a resonant peak whose energy is very close to the gap. Andreev spectroscopy is performed at four different densities ($V_g$), with increasing resonance strength (in terms of amplitude of the signal) from $A$ to $D$ (fig.5.29 left panel). In the middle panel, which shows 2-dimensional $dI/dV$ maps, an Andreev scattering state emerges at $V_g \sim 400\mu V$ , whereas the contrast and the pattern become more and more well-defined as the resonance strength increases from $A$ to $D$. The fact that we can trace this oscillation as a single peak, particularly in cut-$B$ and cut-$C$ , and the amplitude $\sim \Delta$, implies that we are observing a *single Andreev scattering state* formed by the coupling between the superconductor and a resonance state.

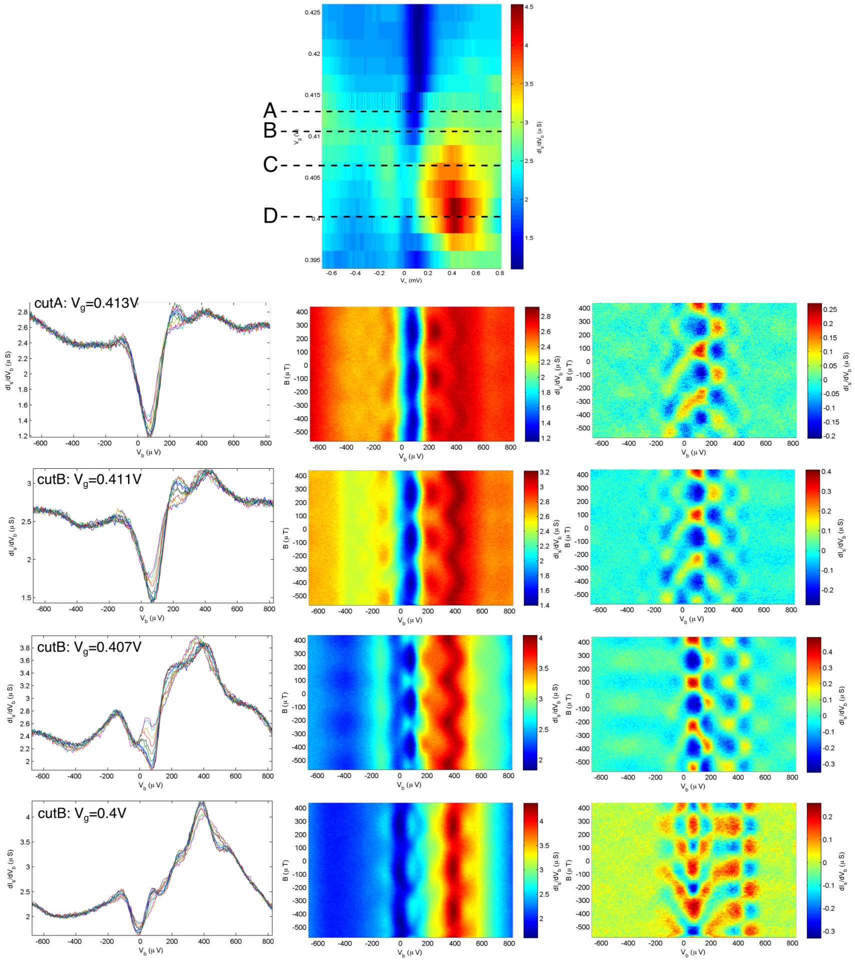

Figure 5.29: Strong resonant state coupled to the superconducting leads. Single Andreev scattering state occurs at $V_g \sim 400\mu V$.

## 5.6 DISCUSSION AND PERSPECTIVES

In this chapter, we investigated the proximity effect in the energy domain by performing tunneling spectroscopy on aluminum-contacted graphene. Andreev bound states in the 2-dimensional limit are measured in a device with squid-like geometry, which allows us to accurately control the phase difference across the weak link. Within the superconducting gap, the measured density of states behave like a collection of Andreev bound states associated with channels of various transmission probability $\tau$.

The oscillation of Andreev bound states is strongly suppressed around the Dirac point, which prevents us from observing an isolated Andreev bound state in a 2-dimensional system. Normal state characterization also shows a flattening out of the density of state at low carrier density.

We realize that all the tunneling devices we have measured so far are of lower quality, compared to the encapsulated devices we fabricated for transport measurement. This is because the top h-BN can not be thicker than ~ 1nm if it is to be an effective tunneling barrier. In the specific case of tunneling spectroscopy at the $\Delta_{Al}$ energy scale measured by a graphite tunneling probe, we are obliged to use only 1L-hBN as the top layer. Thus, a large portion of the graphene area is "encapsulated" by only one atomic layer of h-BN, which is obviously not enough to isolate graphene from the organic residue that results from nanofabrication.

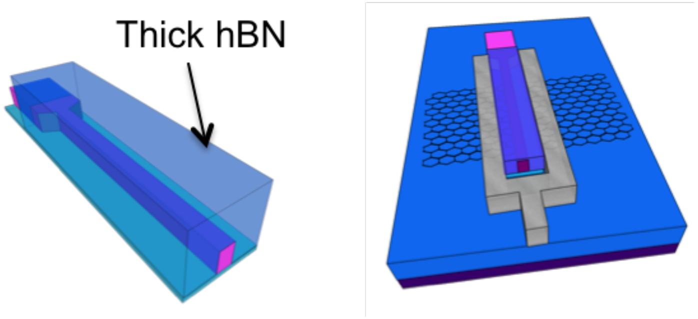

(a) 3-D illustration of the fully encapsulated tunneling device. The graphite tunneling probe is encapsulated between thick h-BN on top and 1L-hBN at the bottom. The entire tunneling module will be used to pick up a graphene flake and transfer it to a bottom stack.

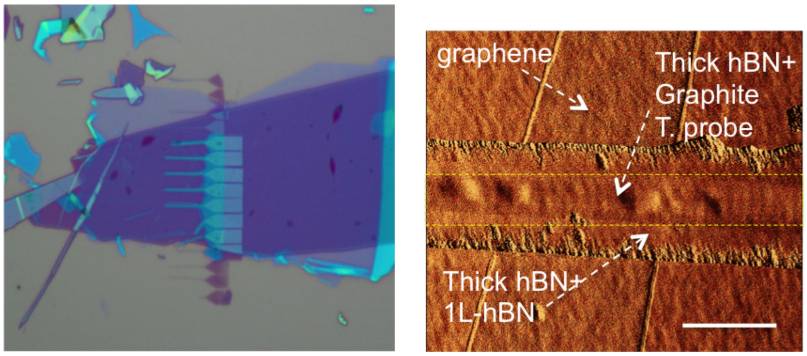

(b) Optical image of the next device: A fully-encapsulated *(thick)h-BN/graphite/1L-hBN/graphene/h-BN/graphite* stack, which is ready for superconductor deposition.

(c) AFM micrograph (amplitude signal) of the fully encapsulated stack.

Figure 5.30: Next measurement: a fully-encapsulated tunneling device

Figure 5.30 shows the latest version of our sample, which will be measured soon. As illustrated in Figure 5.30(a), the graphite probe is encapsulated with a thick h-BN layer (at least 10 nm) from top and by 1L-hBN from the bottom in order to form a "tunneling module". This structure will be used to pick up a graphene flake and the entire stack will be placed on a bottom stack (of h-BN/graphite backgate). In this design, the entire graphene flake is either covered by a thick h-BN layer or the metallic contact with no separation in between. In such a way, any organic residue resulting from nanofabrication will be isolated from the graphene by a thick h-BN layer. Figure 5.30(b)(c) shows the optical and AFM images , respectively, of a stack that is to be contacted by superconducting electrodes. Another improvement rendered in this new design is that it allows us to make a shorter junction (smaller separation between the superconducting leads) without the risk of shorting the tunneling probe to the leads. This new device will be contacted with Al superconducting leads and used to repeat the series of measurements discussed in this chapter.

This new fabrication will also be used to make devices that we intend to proximitize with NbN superconducting leads. With a superconducting gap that is ten times larger than that of Al, NbN allows a larger energy window for spectroscopy[111]. In principle, the measurement will be less sensitive to thermal noise, which broadens the spectroscopic features. Using NbN leads for Andreev spectroscopy also allows us to study the Andreev bound states in a large magnetic field. Measuring induced superconducting gap in quantum Hall regime will be of particular interest.

# APPENDIX

# A

# WAFER AND SAMPLE CLEANING RECIPES

## A.1 PIRANHA + HF CLEANING RECIPE FOR $SIO_2$ WAFER

This cleaning is performed on the $SiO_2$ substrate onto which any 2-D material is deposited.

1. Dice the wafer into chips of desired size and load the chips in a Teflon chip carrier (Fig. A.1). then Successively sonicate subsequently in Acetone, IPA and then DI water, for 2 minutes in each liquid.
2. Move the chips into a glass beaker of piranha solution (a 3:1 mixture of sulfuric acid ($H_2SO_4$) and hydrogen peroxide($H_2O_2$)) and clean for 30mins. Piranha is also made in a separate glass beaker, which will be cleaned and used as a water bath after the cleaning.
3. Empty the water bath beaker and fill the beaker with DI water. Transfer the chips into the water bath beaker and flush with running DI water until at least 20-times volume of water has been replaced.
4. Prepare a 1:10, 50% $HF$ to $H_2O$ , solution in a plastic beaker. Submerge the chip in the diluted $HF$ for 15 seconds. After the $HF$ dip, chips are transferred into a water beaker and then flushed in the sink with at least 20-times volume of water.
5. Sonicate the chip in water beaker for two minutes. Transfer the chip into a beaker filled with IPA and sonicate another 2 minutes.
6. Dry the chip, one at a time, with nitrogen gas.

## A.2 HEAT ANNEALING OF VAN DER WAAL HETEROSTRUCTURES

Heat annealing is performed on the h-BN flakes or heterostructures in order to remove residue or flatten the surface. The standard heat annealing recipe is described as follows:

1. Place the sample on a quartz boat and insert the boat into a quartz tube.
2. Close both ends of the quartz tube. Connect the inlet of the tube to the flow regulator of argon and hydrogen gas. The annealing

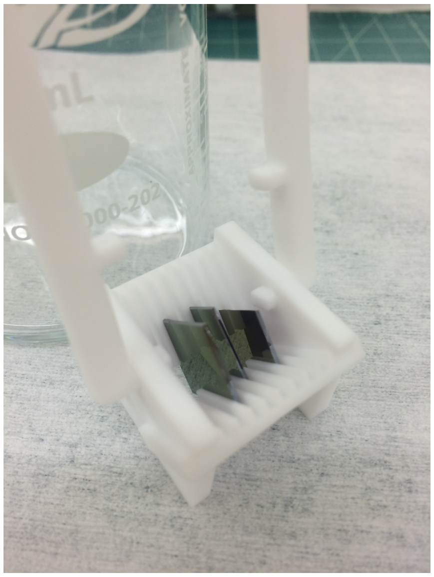

Figure A.1: Si chips in a teflon carrier.

(a) Sample on a quartz boat before loading into the quartz tube.

(b) Image of the furnace with sample loaded inside the quartz tube.

Figure A.2: Heat annealing of samples.

is performed under the atmospheric pressure, with flow controlled at ~ 30 sccm for both gases. The ratio is kept roughly at 1:1.

3. Ramp up the temperature from room temperature to $350^o C$ in 1 hour. Anneal at $350^o C$ for three hours.

## A.3 MECHANICAL CLEANING OF 2-DIMENSIONAL MATERIAL

Following [65], we occasionally perform the mechanical cleaning of h-BN or graphene using AFM operated in the contact mode. This technique is particularly useful when the heat annealing can not remove completely the organic residue on h-BN or graphene.

Figure A.3shows a demonstration of this technique. The sample is a piece of graphite deposited on $SiO_2$ substrate. The graphite was spun with PMMA 950A, baked at $180^o C$ for 10 minutes, and dipped

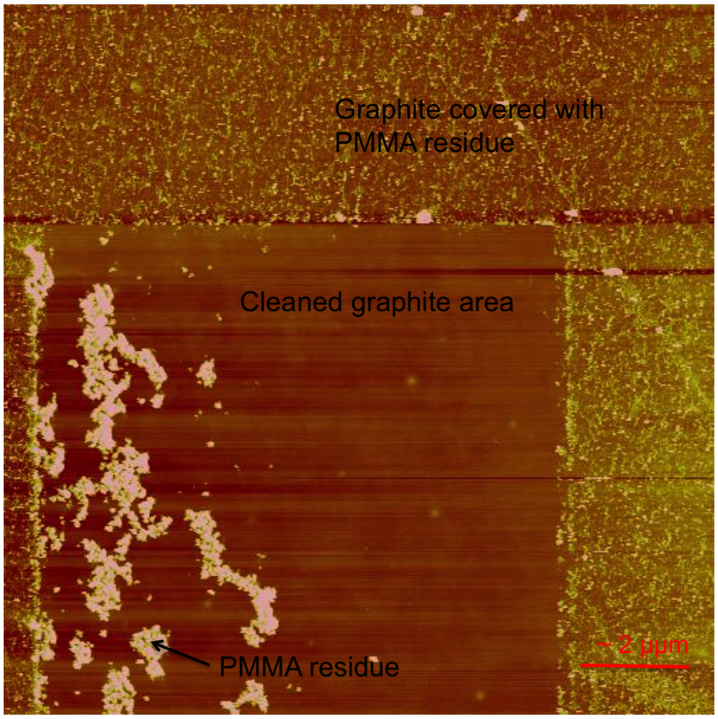

Figure A.3: Demonstration of the mechanical cleaning using contact mode AFM. The sample is a piece of graphite contaminated with baked PMMA. The contact mode AFM swept out a square area at the center of sample. The PMMA residue accumulated in the lower left portion of the sample, indicating that the AFM tip did not pick up the residue but merely swept the residue aside.

in acetone for lifting-off the resist, in order to emulate the condition of graphene surface after resists lift-off. As can be seen clearly on the upper right corner, the sample is covered with an appreciable amount of PMMA residue. The mechanical cleaning leaves a clean area in the central part of the sample. Blocks of PMMA residue observed around the lower left corner indicate that the mechanical cleaning only sweep the residue aside instead of picking up the residue.

This technique can also be used for cleaning the developed area of graphene after exposure, in order to lower the contact resistance due to the PMMA residue.

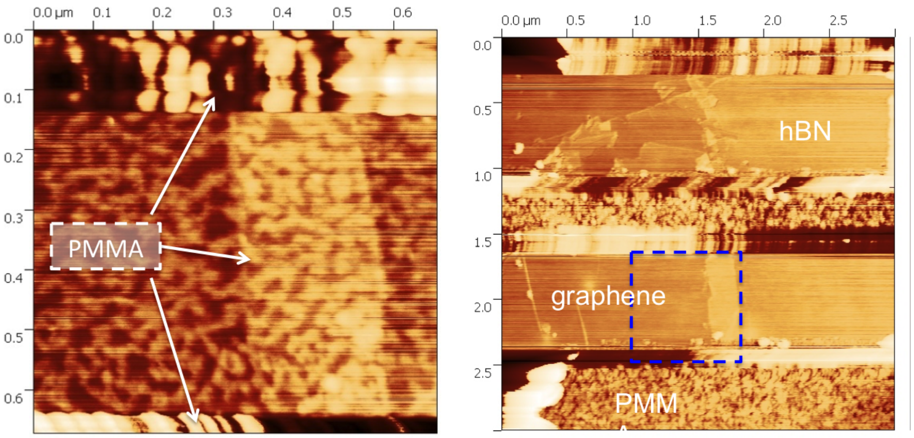

(a) AFM height signal image of a graphene area covered with PMMA residue after e-beam exposure and standard development precess. The large structures on top and bottom of the image are un-exposed PMMA. The central part was e-beam exposed and then developed in a MIBK/IPA solution ( the standard recipe). A substantial coverage of PMMA remains on the developed area. This residue is expected to increase the contact resistance.

(b) AFM height signal image of graphene sample after mechanical cleaning with contact mode AFM. The dashed blue line encloses the area shown in (a). The graphene and hBN surfaces are residue free up to the resolution of the AFM.

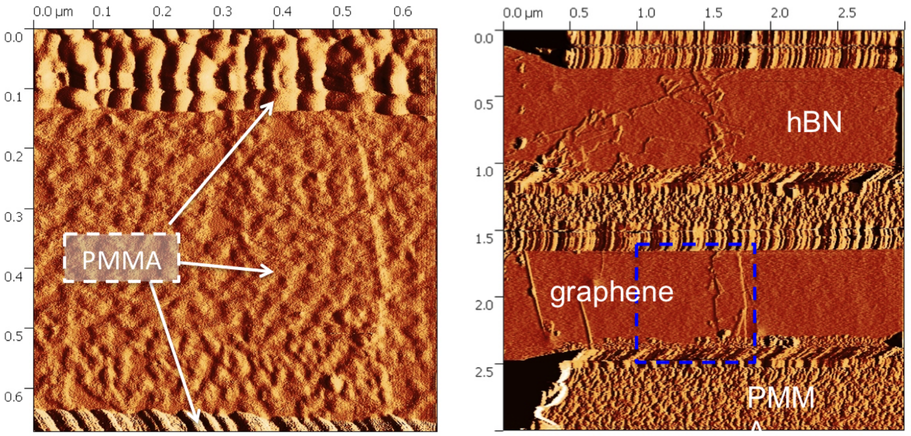

(c) AFM amplitude signal of (a).

(d) AFM amplitude signal of (b).

Figure A.4: Removing the PMMA residue that remains after development in an e-beam exposed graphene area.

# BIBLIOGRAPHY

[1] What is sputtering? - AJA International. URL `http://www.ajaint.com/what-is-sputtering.html`. (Cited on page 40.)

[2] Dmitry a. Abanin and Leonid S. Levitov. Conformal invariance and shape-dependent conductance of graphene samples. *Physical Review B - Condensed Matter and Materials Physics*, 78(3):1–9, 2008. ISSN 10980121. doi: 10.1103/PhysRevB.78.035416. (Cited on page 54.)

[3] Adrien Allain, Zheng Han, and Vincent Bouchiat. Electrical control of the superconducting-to-insulating transition in graphene–metal hybrids. *Nature Materials*, 11(7):590–594, 2012. (Cited on page 12.)

[4] M. T. Allen, O. Shtanko, I. C. Fulga, J. I. J. Wang, D. Nurgaliev, K. Watanabe, T. Taniguchi, A. R. Akhmerov, P. Jarillo-Herrero, L. S. Levitov, and A. Yacoby. Visualization of phase-coherent electron interference in a ballistic graphene Josephson junction. jun 2015. URL `http://arxiv.org/abs/1506.06734`. (Cited on pages 12, 66, and 85.)

[5] Monica T. Allen, Oles Shtanko, Ion Cosma Fulga, Anton Akhmerov, Kenji Watanabi, Takashi Taniguchi, Pablo Jarillo-Herrero, Leonid S. Levitov, and Amir Yacoby. Spatially resolved edge currents and guided-wave electronic states in graphene. page 31, apr 2015. URL `http://arxiv.org/abs/1504.07630`. (Cited on pages 58 and 66.)

[6] F. Amet, J. R. Williams, A. G. F. Garcia, M. Yankowitz, K. Watanabe, T. Taniguchi, and D. Goldhaber-Gordon. Tunneling spectroscopy of graphene-boron-nitride heterostructures. *Physical Review B*, 85(7):073405, feb 2012. ISSN 1098-0121. doi: 10.1103/PhysRevB.85.073405. URL `http://link.aps.org/doi/10.1103/PhysRevB.85.073405`. (Cited on pages 64, 97, 104, and 120.)

[7] F Amet, A J Bestwick, J R Williams, L Balicas, K Watanabe, T Taniguchi, and D Goldhaber-Gordon. Composite fermions and broken symmetries in graphene. *Nature communications*, 6:5838, jan 2015. ISSN 2041-1723. doi: 10.1038/ncomms6838. URL `http://www.nature.com/ncomms/2015/150106/ncomms6838/abs/ncomms6838.html`. (Cited on page 63.)

[8] P. Anderson and J. Rowell. Probable Observation of the Josephson Superconducting Tunneling Effect. *Physical Review Let-*

*ters*, 10(6):230–232, mar 1963. ISSN 0031-9007. doi: 10.1103/PhysRevLett.10.230. URL `http://link.aps.org/doi/10.1103/PhysRevLett.10.230`. (Cited on page 18.)

[9] P.W. Anderson. Theory of dirty superconductors. *Journal of Physics and Chemistry of Solids*, 11(1-2):26–30, 1959. ISSN 00223697. doi: 10.1016/0022-3697(59)90036-8. (Cited on page 32.)

[10] Philip F. Bagwell. Suppression of the Josephson current through a narrow, mesoscopic, semiconductor channel by a single impurity. *Physical Review B*, 46(19):12573–12586, 1992. ISSN 01631829. doi: 10.1103/PhysRevB.46.12573. (Cited on pages 35, 36, 124, 125, and 130.)

[11] J. Bardeen, L. N. Cooper, and J. R. Schrieffer. Theory of Superconductivity. *Physical Review*, 108(5):1175–1204, dec 1957. ISSN 0031-899X. doi: 10.1103/PhysRev.108.1175. URL `http://link.aps.org/doi/10.1103/PhysRev.108.1175`. (Cited on page 15.)

[12] John Bardeen and Jared L. Johnson. Josephson Current Flow in Pure Superconducting-Normal-Superconducting Junctions. *Physical Review B*, 5(1):72–78, jan 1972. ISSN 0556-2805. doi: 10.1103/PhysRevB.5.72. URL `http://link.aps.org/doi/10.1103/PhysRevB.5.72`. (Cited on page 130.)

[13] C. W. J. Beenakker. Specular Andreev Reflection in Graphene. *Physical Review Letters*, 97(6):067007, 2006. ISSN 0031-9007. doi: 10.1103/PhysRevLett.97.067007. URL `http://link.aps.org/doi/10.1103/PhysRevLett.97.067007`. (Cited on pages 11, 12, and 61.)

[14] C. W. J. Beenakker. <i>Colloquium</i> : Andreev reflection and Klein tunneling in graphene. *Reviews of Modern Physics*, 80 (4):1337–1354, 2008. ISSN 0034-6861. doi: 10.1103/RevModPhys.80.1337. URL `http://link.aps.org/doi/10.1103/RevModPhys.80.1337`. (Cited on pages 11 and 62.)

[15] CWJ Beenakker, AR Akhmerov, P Recher, and J Tworzydło. Correspondence between andreev reflection and klein tunneling in bipolar graphene. *Physical Review B*, 77(7):075409, 2008. (Cited on pages 11 and 72.)

[16] Annica M. Black-Schaffer and Sebastian Doniach. Self-consistent solution for proximity effect and Josephson current in ballistic graphene SNS Josephson junctions. *Physical Review B - Condensed Matter and Materials Physics*, 78(2):1–7, 2008. ISSN 10980121. doi: 10.1103/PhysRevB.78.024504. (Cited on page 12.)

[17] K Bladh, D Gunnarsson, E Hürfeld, S Devi, C Kristoffersson, B Smålander, S Pehrson, T Claeson, P Delsing, and M Taslakov. Comparison of cryogenic filters for use in single electronics experiments. *Review of scientific instruments*, 74(3):1323–1327, 2003. (Cited on page 46.)

[18] G. E. Blonder, M. Tinkham, and T. M. Klapwijk. Transition from metallic to tunneling regimes in superconducting microconstrictions: Excess current, charge imbalance, and supercurrent conversion. *Physical Review B*, 25(7):4515–4532, 1982. ISSN 01631829. doi: 10.1103/PhysRevB.25.4515. (Cited on page 31.)

[19] K.I. Bolotin, K.J. Sikes, Z. Jiang, M. Klima, G. Fudenberg, J. Hone, P. Kim, and H.L. Stormer. Ultrahigh electron mobility in suspended graphene. *Solid State Communications*, 146 (9-10):351–355, 2008. ISSN 00381098. doi: 10.1016/j.ssc.2008.02.024. URL `http://linkinghub.elsevier.com/retrieve/pii/S0038109808001178`. (Cited on page 63.)

[20] Kirill I Bolotin, Fereshte Ghahari, Michael D Shulman, Horst L Stormer, and Philip Kim. Observation of the fractional quantum Hall effect in graphene. *Nature*, 475(7354):122, 2011. ISSN 0028-0836. doi: 10.1038/nature10186. URL `http://dx.doi.org/10.1038/nature08582`. (Cited on page 63.)

[21] L Bretheau, ÇÖ Girit, Hugues Pothier, D Esteve, and C Urbina. Exciting andreev pairs in a superconducting atomic contact. *Nature*, 499(7458):312–315, 2013. (Cited on page 91.)

[22] L. Britnell, R. V. Gorbachev, R. Jalil, B. D. Belle, F. Schedin, a. Mishchenko, T. Georgiou, M. I. Katsnelson, L. Eaves, S. V. Morozov, N. M. R. Peres, J. Leist, a. K. Geim, K. S. Novoselov, and L. a. Ponomarenko. Field-Effect Tunneling Transistor Based on Vertical Graphene Heterostructures. *Science*, 335(6071):947–950, 2012. ISSN 0036-8075. doi: 10.1126/science.1218461. (Cited on page 64.)

[23] Liam Britnell, Roman V. Gorbachev, Rashid Jalil, Branson D. Belle, Fred Schedin, Mikhail I. Katsnelson, Laurence Eaves, Sergey V. Morozov, Alexander S. Mayorov, Nuno M R Peres, Antonio H. Castro Neto, Jon Leist, Andre K. Geim, Leonid a. Ponomarenko, and Kostya S. Novoselov. Electron tunneling through ultrathin boron nitride crystalline barriers. *Nano Letters*, 12(3):1707–1710, 2012. ISSN 15306984. doi: 10.1021/nl3002205. (Cited on pages 64, 97, 98, 106, and 109.)

[24] V E Calado, S Goswami, G Nanda, M Diez, A R Akhmerov, K Watanabe, T Taniguchi, T M Klapwijk, and L M K Vandersypen. Ballistic Josephson junctions in edge-contacted

graphene. *Nature nanotechnology*, 10(9):761–764, jul 2015. ISSN 1748-3395. doi: 10.1038/nnano.2015.156. URL http://dx.doi.org/10.1038/nnano.2015.156. (Cited on pages 12, 70, and 85.)

[25] L C Campos, Andrea Franchini Young, Kawin Surakitbovorn, K Watanabe, T Taniguchi, and Pablo Jarillo-Herrero. Quantum and classical confinement of resonant states in a trilayer graphene fabry-pérot interferometer. *Nat. Commun.*, 3(1239): 1239, 2012. (Cited on pages 72 and 80.)

[26] Eduardo V. Castro, H. Ochoa, M. I. Katsnelson, R. V. Gorbachev, D. C. Elias, K. S. Novoselov, a. K. Geim, and F. Guinea. Limits on charge carrier mobility in suspended graphene due to flexural phonons. *Physical Review Letters*, 105(26):16–18, 2010. ISSN 00319007. doi: 10.1103/PhysRevLett.105.266601. (Cited on page 63.)

[27] a. H.. Castro Neto, Nmr M. R.. Peres, K. S.. Novoselov, a. K.. Geim, F. Guinea, and Ahc Neto. The electronic properties of graphene. *Reviews of Modern Physics*, 81(1):109–162, 2009. ISSN 0034-6861. doi: 10.1103/RevModPhys.81.109. URL http://link.aps.org/doi/10.1103/RevModPhys.81.109$\delimiter"026E30F$n/citations?view_op=view_citation&continue=/scholar?hl=en&start=100&as_sdt=0,5&scilib=1&citilm=1&citation_for_view=fLRxLRkAAAAJ:DJbcl8HfkQkC&hl=en&oi=p. (Cited on pages 4, 5, 9, and 120.)

[28] U. Chandni, K. Watanabe, T. Taniguchi, and J. P. Eisenstein. Evidence for defect-mediated tunneling in hexagonal boron nitride-based junctions. page 5, jul 2015. URL http://arxiv.org/abs/1507.01058. (Cited on pages 64, 97, and 121.)

[29] V. V. Cheianov, V. Fal'ko, and B. L. Altshuler. The Focusing of Electron Flow and a Veselago Lens in Graphene p-n Junctions. *Science*, 315(5816):1252–1255, 2007. ISSN 0036-8075. doi: 10.1126/science.1138020. URL http://www.sciencemag.org/cgi/doi/10.1126/science.1138020. (Cited on page 72.)

[30] C.-T. Chen, E. a. Casu, M. Gajek, and S. Raoux. Low-damage high-throughput grazing-angle sputter deposition on graphene. *Applied Physics Letters*, 103(3):033109, 2013. ISSN 00036951. doi: 10.1063/1.4813911. URL http://scitation.aip.org/content/aip/journal/apl/103/3/10.1063/1.4813911. (Cited on page 41.)

[31] Yu-An Chen, Joel I-Jan Wang, Kenji Watanabe, Takashi Taniguchi, and Pablo Jarillo-Herrero. Superconducting Graphene Nanodevices in Ballistic Transport Regime, mar 2013. URL http://meetings.aps.org/link/BAPS.2013.MAR.F7.4. (Cited on page 104.)

[32] Zengguang Cheng, Qiaoyu Zhou, Chenxuan Wang, Qiang Li, Chen Wang, and Ying Fang. Toward intrinsic graphene surfaces: a systematic study on thermal annealing and wet-chemical treatment of SiO2-supported graphene devices. *Nano letters*, 11(2):767–71, mar 2011. ISSN 1530-6992. doi: 10.1021/nl103977d. URL `http://dx.doi.org/10.1021/nl103977d`. (Cited on page 66.)

[33] Sungjae Cho and Michael S. Fuhrer. Charge transport and inhomogeneity near the minimum conductivity point in graphene. *Physical Review B*, 77(8):081402, 2008. ISSN 1098-0121. doi: 10.1103/PhysRevB.77.081402. URL `http://link.aps.org/doi/10.1103/PhysRevB.77.081402`. (Cited on page 51.)

[34] W. G. Cullen, M. Yamamoto, K. M. Burson, J. H. Chen, C. Jang, L. Li, M. S. Fuhrer, and E. D. Williams. High-Fidelity Conformation of Graphene to <math display="inline"> <msub> <mi>SiO</mi> <mn>2</mn> </msub> </math> Topographic Features. *Physical Review Letters*, 105(21):215504, 2010. ISSN 0031-9007. doi: 10.1103/PhysRevLett.105.215504. URL `http://link.aps.org/doi/10.1103/PhysRevLett.105.215504`. (Cited on page 62.)

[35] R Danneau, F Wu, MF Craciun, S Russo, MY Tomi, J Salmilehto, AF Morpurgo, and PJ Hakonen. Shot noise in ballistic graphene. *Physical review letters*, 100(19):196802, 2008. (Cited on page 87.)

[36] S. Das Sarma, Shaffique Adam, E. H. Hwang, and Enrico Rossi. Electronic transport in two-dimensional graphene. *Reviews of Modern Physics*, 83(2):407–470, 2011. ISSN 00346861. doi: 10.1103/RevModPhys.83.407. (Cited on page 10.)

[37] Supriyo Datta. *Electronic transport in mesoscopic systems*. Cambridge university press, 1997. (Cited on page 62.)

[38] P. G. DE GENNES. Boundary Effects in Superconductors. *Reviews of Modern Physics*, 36(1):225–237, jan 1964. ISSN 0034-6861. doi: 10.1103/RevModPhys.36.225. URL `http://link.aps.org/doi/10.1103/RevModPhys.36.225`. (Cited on pages viii and 27.)

[39] PG De Gennes. *Superconductivity of Metals and Alloys (Advanced Book Classics)*. Addison-Wesley Publ. Company Inc, 1999. (Cited on pages 15 and 31.)

[40] C R Dean, a F Young, I Meric, C Lee, L Wang, S Sorgenfrei, K Watanabe, T Taniguchi, P Kim, K L Shepard, and J Hone. Boron nitride substrates for high-quality graphene electronics. *Nature nanotechnology*, 5(10):722–726, 2010. ISSN 1748-3387. doi: 10.1038/nnano.2010.172. (Cited on pages 63, 64, and 104.)

[41] C. R. Dean, A. F. Young, P. Cadden-Zimansky, L. Wang, H. Ren, K. Watanabe, T. Taniguchi, P. Kim, J. Hone, and K. L. Shepard. Multicomponent fractional quantum Hall effect inÂ graphene. *Nature Physics*, 7(9):693–696, may 2011. ISSN 1745-2473. doi: 10.1038/nphys2007. URL `http://dx.doi.org/10.1038/nphys2007`. (Cited on page 63.)

[42] C R Dean, L Wang, P Maher, C Forsythe, F Ghahari, Y Gao, J Katoch, M Ishigami, P Moon, M Koshino, T Taniguchi, K Watanabe, K L Shepard, J Hone, and P Kim. Hofstadter's butterfly and the fractal quantum Hall effect in moiré superlattices. *Nature*, 497(7451):598–602, may 2013. ISSN 1476-4687. doi: 10.1038/nature12186. URL `http://dx.doi.org/10.1038/nature12186`. (Cited on pages 63 and 104.)

[43] Kevin A Delin and TP Orlando. *Foundations of Applied Superconductivity*. Addison-Wesley Reading, MA, 1991. (Cited on page 24.)

[44] L Dicarlo, J R Williams, Yiming Zhang, D T McClure, and C M Marcus. Shot noise in graphene. *Physical review letters*, 100(15):156801, apr 2008. ISSN 0031-9007. doi: 10.1103/PhysRevLett.100.156801. URL `http://www.ncbi.nlm.nih.gov/pubmed/18518138`. (Cited on page 87.)

[45] Travis Dirks, Taylor L. Hughes, Siddhartha Lal, Bruno Uchoa, Yung-Fu Chen, Cesar Chialvo, Paul M. Goldbart, and Nadya Mason. Transport Through Andreev Bound States in a Graphene Quantum Dot. *Nature Physics*, 7(5):25, 2010. ISSN 1745-2473. doi: 10.1038/nphys1911. URL `http://arxiv.org/abs/1005.2749`. (Cited on page 91.)

[46] B. Dlubak, P. Seneor, A. Anane, C. Barraud, C. Deranlot, D. Deneuve, B. Servet, R. Mattana, F. Petroff, and A. Fert. Are Al[sub 2]O[sub 3] and MgO tunnel barriers suitable for spin injection in graphene? *Applied Physics Letters*, 97(9):092502, aug 2010. ISSN 00036951. doi: 10.1063/1.3476339. URL `http://scitation.aip.org/content/aip/journal/apl/97/9/10.1063/1.3476339`. (Cited on page 41.)

[47] Xu Du, Ivan Skachko, and Eva Y. Andrei. Josephson current and multiple Andreev reflections in graphene SNS junctions. *Physical Review B*, 77(18):184507, 2008. ISSN 1098-0121. doi: 10.1103/PhysRevB.77.184507. URL `http://link.aps.org/doi/10.1103/PhysRevB.77.184507`. (Cited on pages 12 and 78.)

[48] Xu Du, Ivan Skachko, Anthony Barker, and Eva Y. Andrei. Approaching ballistic transport in suspended graphene. *Nature Nanotechnology*, 3(8):491–495, 2008. ISSN 1748-3387.

doi: 10.1038/nnano.2008.199. URL http://www.nature.com/doifinder/10.1038/nnano.2008.199. (Cited on page 63.)

[49] D. K. Efetov, L. Wang, C. Handschin, K. B. Efetov, J. Shuang, R. Cava, T. Taniguchi, K. Watanabe, J. Hone, C. R. Dean, and P. Kim. Specular Interband Andreev Reflections in Graphene. may 2015. URL http://arxiv.org/abs/1505.04812. (Cited on pages 12, 66, and 70.)

[50] Jack Ekin. *Experimental Techniques for Low-Temperature Measurements: Cryostat Design, Material Properties and Superconductor Critical-Current Testing: Cryostat Design, Material Properties and Superconductor Critical-Current Testing*. Oxford University Press, 2006. (Cited on pages viii, 44, and 45.)

[51] J. Eroms, D. Weiss, J. De Boeck, G. Borghs, and U. Zülicke. Andreev Reflection at High Magnetic Fields: Evidence for Electron and Hole Transport in Edge States. *Physical Review Letters*, 95 (10):107001, 2005. ISSN 0031-9007. doi: 10.1103/PhysRevLett.95.107001. URL http://link.aps.org/doi/10.1103/PhysRevLett.95.107001. (Cited on page 39.)

[52] M. V. Feigel'man, M. a. Skvortsov, and K. S. Tikhonov. Proximity-induced superconductivity in graphene. (1):1–4, 2008. doi: 10.1134/S0021364008230100. URL http://arxiv.org/abs/0810.0109http://dx.doi.org/10.1134/S0021364008230100. (Cited on page 12.)

[53] Benjamin E. Feldman, Jens Martin, and Amir Yacoby. Broken-symmetry states and divergent resistance in suspended bilayer graphene. *Nature Physics*, 5(12):889–893, 2009. ISSN 1745-2473. doi: 10.1038/nphys1406. URL http://www.nature.com/doifinder/10.1038/nphys1406. (Cited on page 63.)

[54] G. Frossati. Experimental techniques: Methods for cooling below 300 mK. *Journal of Low Temperature Physics*, 87(3-4):595–633, 1992. ISSN 00222291. doi: 10.1007/BF00114918. (Cited on pages ix, 44, and 46.)

[55] A K Geim and I V Grigorieva. Van der Waals heterostructures. *Nature*, 499(7459):419–25, jul 2013. ISSN 1476-4687. doi: 10.1038/nature12385. URL http://dx.doi.org/10.1038/nature12385. (Cited on pages 1, 63, and 70.)

[56] a K Geim and K.S. Novoselov. The rise of graphene. *Nature Mater.*, 6(3):183–191, 2007. ISSN 1476-1122. doi: 10.1038/nmat1849. URL http://www.nature.com/doifinder/10.1038/nmat1849. (Cited on page 2.)

[57] Andrey K. Geim and Allan H. MacDonald. Graphene: Exploring carbon flatland. *Physics Today*, 60(8):35–41, 2007. ISSN 0031-9228. doi: 10.1063/1.2774096. URL `http://scitation.aip.org/content/aip/magazine/physicstoday/article/60/8/10.1063/1.2774096`. (Cited on pages 2 and 62.)

[58] I. Giaever, H. R. Hart, and K. Megerle. Tunneling into Superconductors at Temperatures below 1Â°K. *Physical Review*, 126(3): 941–948, may 1962. ISSN 0031-899X. doi: 10.1103/PhysRev.126.941. URL `http://link.aps.org/doi/10.1103/PhysRev.126.941`. (Cited on page 15.)

[59] I. Giaever, H. R. Hart, and K. Megerle. Tunneling into superconductors at temperatures below 1K. *Physical Review*, 126(3): 941–948, 1962. ISSN 0031899X. doi: 10.1103/PhysRev.126.941. URL `http://dx.doi.org/10.1103/PhysRev.126.941`. (Cited on page 90.)

[60] Ivar Giaever. Electron tunneling between two superconductors. *Physical Review Letters*, 5(10):464–466, 1960. ISSN 00319007. doi: 10.1103/PhysRevLett.5.464. (Cited on page 90.)

[61] Ivar Giaever. Energy gap in superconductors measured by electron tunneling. *Physical Review Letters*, 5(4):147–148, 1960. ISSN 00319007. doi: 10.1103/PhysRevLett.5.147. (Cited on page 90.)

[62] Ivar Giaever. Electron tunneling and superconductivity. *Reviews of Modern Physics*, 46(2):245, 1968. ISSN 0034-6861. doi: 10.1103/RevModPhys.46.245. URL `http://dx.doi.org/10.1103/RevModPhys.46.245`. (Cited on page 90.)

[63] G. Giovannetti, P. a. Khomyakov, G. Brocks, V. M. Karpan, J. Van Den Brink, and P. J. Kelly. Doping graphene with metal contacts. *Physical Review Letters*, 101(2):3–6, 2008. ISSN 00319007. doi: 10.1103/PhysRevLett.101.026803. (Cited on pages xii, 56, 81, 109, and 111.)

[64] Gianluca Giovannetti, Petr A. Khomyakov, Geert Brocks, Paul J. Kelly, and Jeroen van den Brink. Substrate-induced band gap in graphene on hexagonal boron nitride: Ab initio density functional calculations. *Physical Review B*, 76(7):073103, aug 2007. ISSN 1098-0121. doi: 10.1103/PhysRevB.76.073103. URL `http://link.aps.org/doi/10.1103/PhysRevB.76.073103`. (Cited on page 64.)

[65] AM Goossens, VE Calado, A Barreiro, K Watanabe, T Taniguchi, and LMK Vandersypen. Mechanical cleaning of graphene. *Applied Physics Letters*, 100(7):073110, 2012. (Cited on page 137.)

[66] Roman V Gorbachev, Ibtsam Riaz, Rahul R Nair, Rashid Jalil, Liam Britnell, Branson D Belle, Ernie W Hill, Kostya S Novoselov, Kenji Watanabe, Takashi Taniguchi, Andre K Geim, and Peter Blake. Hunting for monolayer boron nitride: optical and Raman signatures. *Small (Weinheim an der Bergstrasse, Germany)*, 7(4):465–8, mar 2011. ISSN 1613-6829. doi: 10.1002/smll.201001628. URL `http://www.ncbi.nlm.nih.gov/pubmed/21360804`. (Cited on pages 99 and 100.)

[67] Rudolf Gross, Achim Marx, and Frank Deppe. *Applied superconductivity: Josephson effect and superconducting electronics*. De Gruyter, 2015. (Cited on page 24.)

[68] Anya L Grushina, Dong-Keun Ki, and Alberto F Morpurgo. A ballistic pn junction in suspended graphene with split bottom gates. *Appl. Phys. Lett.*, 102(22):223102, 2013. (Cited on page 72.)

[69] H. Haugen, a. Brataas, X. Waintal, and G. E. W. Bauer. Focused crossed Andreev reflection. *EPL (Europhysics Letters)*, 93(6):67005, 2011. ISSN 0295-5075. doi: 10.1209/0295-5075/93/67005. URL `http://stacks.iop.org/0295-5075/93/i=6/a=67005?key=crossref.5892c9848577a03b5e04b9db39d924b4`. (Cited on pages 39 and 61.)

[70] Hubert B. Heersche, Pablo Jarillo-Herrero, Jeroen B. Oostinga, Lieven M. K. Vandersypen, and Alberto F. Morpurgo. Bipolar supercurrent in graphene. *Nature*, 446(7131):56–59, 2007. ISSN 0028-0836. doi: 10.1038/nature05555. URL `http://www.nature.com/doifinder/10.1038/nature05555`. (Cited on pages viii, xvi, 11, 58, and 78.)

[71] H Hoppe, U Zulicke, and G Schon. Andreev reflection in strong magnetic fields. *Physical review letters*, 84(8):1804–7, 2000. ISSN 1079-7114. doi: 10.1103/PhysRevLett.84.1804. URL `http://www.ncbi.nlm.nih.gov/pubmed/11017630`. (Cited on page 39.)

[72] B. Hunt, J. D. Sanchez-Yamagishi, A. F. Young, M. Yankowitz, B. J. LeRoy, K. Watanabe, T. Taniguchi, P. Moon, M. Koshino, P. Jarillo-Herrero, and R. C. Ashoori. Massive Dirac Fermions and Hofstadter Butterfly in a van der Waals Heterostructure. *Science*, 340(6139):1427–1430, may 2013. ISSN 0036-8075. doi: 10.1126/science.1237240. URL `http://www.sciencemag.org/content/340/6139/1427.abstract`. (Cited on page 63.)

[73] E. H. Hwang, S. Adam, and S. Das Sarma. Carrier Transport in Two-Dimensional Graphene Layers. *Physical Review Letters*, 98(18):186806, may 2007. ISSN 0031-9007. doi: 10.1103/PhysRevLett.98.186806. URL `http://link.aps.org/doi/10.1103/PhysRevLett.98.186806`. (Cited on page 51.)

[74] Zhi Jin, Yongbo Su, Jianwu Chen, Xinyu Liu, and Dexin Wu. Study of AlN dielectric film on graphene by Raman microscopy. *Applied Physics Letters*, 95(23):233110, dec 2009. ISSN 00036951. doi: 10.1063/1.3271676. URL `http://scitation.aip.org/content/aip/journal/apl/95/23/10.1063/1.3271676`. (Cited on page 41.)

[75] B.D. Josephson. Possible new effects in superconductive tunnelling. *Physics Letters*, 1(7):251–253, jul 1962. ISSN 00319163. doi: 10.1016/0031-9163(62)91369-0. URL `http://www.sciencedirect.com/science/article/pii/0031916362913690`. (Cited on page 18.)

[76] Anand Kamlapure, Mintu Mondal, Madhavi Chand, Archana Mishra, John Jesudasan, Vivas Bagwe, L Benfatto, Vikram Tripathi, and Pratap Raychaudhuri. Measurement of magnetic penetration depth and superconducting energy gap in very thin epitaxial nbn films. *Applied Physics Letters*, 96(7):072509, 2010. (Cited on page 58.)

[77] M. I. Katsnelson, K. S. Novoselov, and a. K. Geim. Chiral tunnelling and the Klein paradox inÂ graphene. *Nature Physics*, 2 (9):620–625, 2006. ISSN 1745-2473. doi: 10.1038/nphys384. URL `http://www.nature.com/doifinder/10.1038/nphys384`. (Cited on pages viii, 9, 10, and 80.)

[78] BM Kessler, ÇÖ Girit, A Zettl, and Vincent Bouchiat. Tunable superconducting phase transition in metal-decorated graphene sheets. *Physical review letters*, 104(4):047001, 2010. (Cited on page 12.)

[79] P. a. Khomyakov, G. Giovannetti, P. C. Rusu, G. Brocks, J. Van Den Brink, and P. J. Kelly. First-principles study of the interaction and charge transfer between graphene and metals. *Physical Review B - Condensed Matter and Materials Physics*, 79(19):1–12, 2009. ISSN 10980121. doi: 10.1103/PhysRevB.79.195425. (Cited on pages 56 and 109.)

[80] Oskar Klein. Die reflexion von elektronen an einem potentialsprung nach der relativistischen dynamik von dirac. *Zeitschrift für Physik*, 53(3-4):157–165, 1929. (Cited on page 8.)

[81] A Kou, B E Feldman, A J Levin, B I Halperin, K Watanabe, T Taniguchi, and A Yacoby. Bilayer graphene. Electron-hole asymmetric integer and fractional quantum Hall effect in bilayer graphene. *Science (New York, N.Y.)*, 345(6192):55–7, jul 2014. ISSN 1095-9203. doi: 10.1126/science.1250270. URL `http://www.sciencemag.org/content/345/6192/55.abstract`. (Cited on page 63.)

[82] Shugo Kubo, Masayoshi Asahi, Makoto Hikita, and Masaru Igarashi. Magnetic penetration depths in superconducting NbN films prepared by reactive dc magnetron sputtering. *Applied Physics Letters*, 44(2):258, jan 1984. ISSN 00036951. doi: 10.1063/1.94690. URL `http://scitation.aip.org/content/aip/journal/apl/44/2/10.1063/1.94690`. (Cited on page 58.)

[83] I. O. Kulik. Macroscopic Quantization and the Proximity Effect in S-N-S Junctions. *Soviet Journal of Experimental and Theoretical Physics*, 30:944, 1969. ISSN 1063-7761. URL `http://adsabs.harvard.edu/abs/1969JETP...30..944K`. (Cited on page 33.)

[84] H Le Sueur, P Joyez, H Pothier, C Urbina, and D Esteve. Phase controlled superconducting proximity effect probed by tunneling spectroscopy. *Physical review letters*, 100(19):197002, 2008. (Cited on pages 90, 96, and 122.)

[85] Hélène le Sueur and Philippe Joyez. Microfabricated electromagnetic filters for millikelvin experiments. *Review of scientific instruments*, 77(11):115102, 2006. (Cited on page 46.)

[86] Gwan-Hyoung Lee, Young-Jun Yu, Changgu Lee, Cory Dean, Kenneth L. Shepard, Philip Kim, and James Hone. Electron tunneling through atomically flat and ultrathin hexagonal boron nitride. *Applied Physics Letters*, 99(24):243114, 2011. ISSN 00036951. doi: 10.1063/1.3662043. URL `http://scitation.aip.org/content/aip/journal/apl/99/24/10.1063/1.3662043`. (Cited on pages 64, 97, and 98.)

[87] Guohong Li, A. Luican, J. M. B. Lopes dos Santos, A. H. Castro Neto, A. Reina, J. Kong, and E. Y. Andrei. Observation of Van Hove singularities in twisted graphene layers. *Nature Physics*, 6(2):109–113, 2009. ISSN 1745-2473. doi: 10.1038/nphys1463. URL `http://www.nature.com/doifinder/10.1038/nphys1463`. (Cited on page 120.)

[88] Chun Hung Lui, Li Liu, Kin Fai Mak, George W. Flynn, and Tony F. Heinz. Ultraflat graphene. *Nature*, 462(7271):339–341, nov 2009. ISSN 0028-0836. doi: 10.1038/nature08569. URL `http://dx.doi.org/10.1038/nature08569`. (Cited on page 63.)

[89] Jens Martin, N Akerman, G Ulbricht, T Lohmann, JH Smet, K Von Klitzing, and Amir Yacoby. Observation of electron–hole puddles in graphene using a scanning single-electron transistor. *Nature Physics*, 4(2):144–148, 2008. (Cited on pages 11, 51, 62, and 120.)

[90] John M Martinis, Michel H Devoret, and John Clarke. Experimental tests for the quantum behavior of a macroscopic degree

of freedom: The phase difference across a Josephson junction. *Physical Review B*, 35(10):4682–4698, 1987. (Cited on page 46.)

[91] Alexander S Mayorov, Roman V Gorbachev, Sergey V Morozov, Liam Britnell, Rashid Jalil, Leonid A Ponomarenko, Peter Blake, Kostya S Novoselov, Kenji Watanabe, Takashi Taniguchi, and A K Geim. Micrometer-scale ballistic transport in encapsulated graphene at room temperature. *Nano letters*, 11(6):2396–9, jun 2011. ISSN 1530-6992. doi: 10.1021/nl200758b. URL `http://dx.doi.org/10.1021/nl200758b`. (Cited on page 68.)

[92] N Mizuno, B Nielsen, and X Du. Suspended Graphene Ballistic Josephson Weak Links. *Nature communications*, 4:2716, 2013. URL `http://arxiv.org/abs/1305.2180`. (Cited on pages 12 and 66.)

[93] Naomi Mizuno, Bent Nielsen, and Xu Du. Ballistic-like supercurrent in suspended graphene Josephson weak links. *Nature communications*, 4:2716, jan 2013. ISSN 2041-1723. doi: 10.1038/ncomms3716. URL `http://www.nature.com/ncomms/2013/131114/ncomms3716/full/ncomms3716.html`. (Cited on pages 63 and 66.)

[94] a. Morpurgo, B. van Wees, T. Klapwijk, and G. Borghs. Energy Spectroscopy of Andreev Levels between Two Superconductors. *Physical Review Letters*, 79(20):4010–4013, 1997. ISSN 0031-9007. doi: 10.1103/PhysRevLett.79.4010. (Cited on page 90.)

[95] Alberto Morpurgo. *Andreev bound states and spin-orbit Berry's phase in high quality InAs/AISb heterostructures*. PhD thesis, University of Groningen, 1998. (Cited on page 28.)

[96] K. S. Novoselov. Nobel Lecture: Graphene: Materials in the Flatland. *Reviews of Modern Physics*, 83(3):837–849, 2011. ISSN 00346861. doi: 10.1103/RevModPhys.83.837. (Cited on page 62.)

[97] K S Novoselov, A K Geim, S V Morozov, D Jiang, Y Zhang, S V Dubonos, I V Grigorieva, and A A Firsov. Electric field effect in atomically thin carbon films. *Science (New York, N.Y.)*, 306(5696): 666–669, 2004. ISSN 1095-9203. doi: 10.1126/science.1102896. (Cited on pages 1, 2, and 39.)

[98] D. E. Oates, Alfredo C. Anderson, C. C. Chin, J. S. Derov, G. Dresselhaus, and M. S. Dresselhaus. Surface-impedance measurements of superconducting NbN films. *Physical Review B*, 43(10):7655–7663, apr 1991. ISSN 0163-1829. doi: 10.1103/PhysRevB.43.7655. URL `http://link.aps.org/doi/10.1103/PhysRevB.43.7655`. (Cited on page 58.)

[99] R. Otadoy and a. Lodder. Andreev bound states and self-consistent gap functions in clean layered superconductor/normal metal systems with finite transverse width. *Physical Review B*, 65(2):1–12, 2001. ISSN 0163-1829. doi: 10.1103/PhysRevB.65.024521. (Cited on page 95.)

[100] Barbaros Ozyilmaz, Pablo Jarillo-Herrero, Dmitri Efetov, Dmitry Abanin, Leonid Levitov, and Philip Kim. Electronic transport and quantum hall effect in bipolar graphene p-n-p junctions. *Phys. Rev. Lett.*, 99(16):166804, October 2007. (Cited on page 72.)

[101] Jean-Damien Pillet, Charis Quay, Pascal Morfin, Cristina Bena, a. Levy Yeyati, and Philippe Joyez. Revealing the electronic structure of a carbon nanotube carrying a supercurrent. *Nature Physics*, 6(12):965–969, 2010. ISSN 1745-2473. doi: 10.1038/nphys1811. URL `http://arxiv.org/abs/1005.0443`. (Cited on pages 90, 95, and 122.)

[102] L A Ponomarenko, R V Gorbachev, G L Yu, D C Elias, R Jalil, A A Patel, A Mishchenko, A S Mayorov, C R Woods, J R Wallbank, M Mucha-Kruczynski, B A Piot, M Potemski, I V Grigorieva, K S Novoselov, F Guinea, V I Fal'ko, and A K Geim. Cloning of Dirac fermions in graphene superlattices. *Nature*, 497(7451):594–7, may 2013. ISSN 1476-4687. doi: 10.1038/nature12187. URL `http://dx.doi.org/10.1038/nature12187`. (Cited on page 63.)

[103] Peter Rickhaus, Markus Weiss, Laurent Marot, and Christian Schönenberger. Quantum hall effect in graphene with superconducting electrodes. *Nano Letters*, 12(4):1942–1945, 2012. ISSN 15306984. doi: 10.1021/nl204415s. (Cited on pages 12, 61, and 66.)

[104] Peter Rickhaus, Romain Maurand, Ming-Hao Liu, Markus Weiss, Klaus Richter, and Christian Schönenberger. Ballistic interferences in suspended graphene. *Nature Communications*, 4:1–6, 2013. ISSN 2041-1723. doi: 10.1038/ncomms3342. URL `http://www.nature.com/doifinder/10.1038/ncomms3342`. (Cited on pages 80 and 82.)

[105] Peter Rickhaus, Romain Maurand, Ming-Hao Liu, Markus Weiss, Klaus Richter, and Christian Schönenberger. Ballistic interferences in suspended graphene. *Nat. Commun.*, 4:2342, 2013. (Cited on page 72.)

[106] Dimitri Roditchev, Christophe Brun, Lise Serrier-Garcia, Juan Carlos Cuevas, Vagner Henrique Loiola Bessa, Milorad Vlado Milošević, François Debontridder, Vasily Stolyarov,

and Tristan Cren. Direct observation of Josephson vortex cores. *Nature Physics*, 11(4):332–337, feb 2015. ISSN 1745-2473. doi: 10.1038/nphys3240. URL `http://dx.doi.org/10.1038/nphys3240`. (Cited on page 90.)

[107] M J Rooks, E Kratschmer, R Viswanathan, J Katine, R E Fontana, and S A MacDonald. Low stress development of poly(methylmethacrylate) for high aspect ratio structures. *Journal of Vacuum Science & Technology B*, 20(6):2937–2941, 2002. ISSN 0734211X. doi: Doi10.1116/1.1524971. URL `<GotoISI>://WOS:000180307300138`. (Cited on page 75.)

[108] P. San-Jose, J. L. Lado, R. Aguado, F. Guinea, and J. Fernández-Rossier. Majorana Zero Modes in Graphene. pages 1–9, 2015. URL `http://arxiv.org/abs/1506.04961`. (Cited on page 12.)

[109] Elton J G Santos and Efthimios Kaxiras. Electric-field dependence of the effective dielectric constant in graphene. *Nano letters*, 13(3):898–902, mar 2013. ISSN 1530-6992. doi: 10.1021/nl303611v. URL `http://dx.doi.org/10.1021/nl303611v`. (Cited on page 65.)

[110] Christian P. Scheller, Sarah Heizmann, Kristine Bedner, Dominic Giss, Matthias Meschke, Dominik M. Zumbühl, Jeramy D. Zimmerman, and Arthur C. Gossard. Silver-epoxy microwave filters and thermalizers for millikelvin experiments. *Applied Physics Letters*, 104(21):211106, 2014. ISSN 00036951. doi: 10.1063/1.4880099. (Cited on page 46.)

[111] J. Schindele, a. Baumgartner, R. Maurand, M. Weiss, and C. Schönenberger. Nonlocal spectroscopy of Andreev bound states. *Physical Review B - Condensed Matter and Materials Physics*, 89(4):1–8, 2014. ISSN 10980121. doi: 10.1103/PhysRevB.89.045422. (Cited on page 134.)

[112] L. Serrier-Garcia, J. C. Cuevas, T. Cren, C. Brun, V. Cherkez, F. Debontridder, D. Fokin, F. S. Bergeret, and D. Roditchev. Scanning tunneling spectroscopy study of the proximity effect in a disordered two-dimensional metal. *Physical Review Letters*, 110(15):1–5, 2013. ISSN 00319007. doi: 10.1103/PhysRevLett.110.157003. (Cited on page 90.)

[113] M Ben Shalom, M J Zhu, V I Fal, a Mishchenko, a V Kretinin, K S Novoselov, and C R Woods. Proximity superconductivity in ballistic graphene, from Fabry-Perot oscillations to random Andreev states in magnetic field. *arXiv*, page 1504.03286, 2015. URL `http://arxiv.org/abs/1504.03286`. (Cited on pages 12, 70, and 85.)

[114] D. H. Slichter, O. Naaman, and I. Siddiqi. Millikelvin thermal and electrical performance of lossy transmission line filters. *Applied Physics Letters*, 94(19):192508, 2009. ISSN 00036951. doi: 10.1063/1.3133362. URL `http://scitation.aip.org/content/aip/journal/apl/94/19/10.1063/1.3133362`. (Cited on page 46.)

[115] Lafe Spietz, John Teufel, and R. J. Schoelkopf. A Twisted Pair Cryogenic Filter. pages 1–12, 2006. URL `http://arxiv.org/abs/cond-mat/0601316`. (Cited on pages 46 and 48.)

[116] Michael Stone and Yiruo Lin. Josephson Currents in Quantum Hall Devices. 945(1993), 2011. doi: 10.1103/PhysRevB.83.224501. URL `http://arxiv.org/abs/1102.5265http://dx.doi.org/10.1103/PhysRevB.83.224501`. (Cited on page 39.)

[117] Hideaki Takayanagi and Tatsushi Akazaki. Semiconductor-coupled superconducting junctions using NbN electrodes with high Hc2 and Tc. *Physica B: Condensed Matter*, 249-251:462–466, 1998. ISSN 09214526. doi: 10.1016/S0921-4526(98)00164-1. (Cited on page 39.)

[118] Thiti Taychatanapat, Kenji Watanabe, Takashi Taniguchi, and Pablo Jarillo-Herrero. Quantum Hall effect and Landau-level crossing of Dirac fermions in trilayer graphene. *Nature Physics*, 7(8):621–625, jun 2011. ISSN 1745-2473. doi: 10.1038/nphys2008. URL `http://dx.doi.org/10.1038/nphys2008`. (Cited on pages 63, 64, 66, 68, and 104.)

[119] Thiti Taychatanapat, Kenji Watanabe, Takashi Taniguchi, and Pablo Jarillo-Herrero. Electrically tunable transverse magnetic focusing in graphene. *Nature Physics*, 9(4):225–229, feb 2013. ISSN 1745-2473. doi: 10.1038/nphys2549. URL `http://dx.doi.org/10.1038/nphys2549`. (Cited on pages 63, 66, and 72.)

[120] Michael Tinkham. *Introduction to superconductivity*. Courier Corporation, 2012. (Cited on pages 15, 24, 55, 58, 84, 92, 93, and 118.)

[121] M. Titov and C. W J Beenakker. Josephson effect in ballistic graphene. *Physical Review B - Condensed Matter and Materials Physics*, 74(4):1–4, 2006. ISSN 10980121. doi: 10.1103/PhysRevB.74.041401. (Cited on pages 11, 12, 61, 84, and 87.)

[122] Nikolaos Tombros, Alina Veligura, Juliane Junesch, J. Jasper van den Berg, Paul J. Zomer, Magdalena Wojtaszek, Ivan J. Vera Marun, Harry T. Jonkman, and Bart J. van Wees. Large yield production of high mobility freely suspended graphene electronic devices on a polydimethylglutarimide based organic polymer. *Journal of Applied Physics*, 109

(9):093702, may 2011. ISSN 00218979. doi: 10.1063/1.3579997. URL `http://scitation.aip.org/content/aip/journal/jap/109/9/10.1063/1.3579997`. (Cited on page 63.)

[123] C. Tonnoir, a. Kimouche, J. Coraux, L. Magaud, B. Delsol, B. Gilles, and C. Chapelier. Induced superconductivity in graphene grown on rhenium. *Physical Review Letters*, 111(24): 1–5, 2013. ISSN 00319007. doi: 10.1103/PhysRevLett.111.246805. (Cited on page 91.)

[124] D. Vion, P. F. Orfila, P. Joyez, D. Esteve, and M. H. Devoret. Miniature electrical filters for single electron devices. *Journal of Applied Physics*, 77(6):2519, March 1995. ISSN 00218979. doi: 10.1063/1.358781. URL `http://scitation.aip.org.ezp-prod1.hul.harvard.edu/content/aip/journal/jap/77/6/10.1063/1.358781`. (Cited on pages 45 and 46.)

[125] P. R. Wallace. The band theory of graphite. *Physical Review*, 71 (9):622–634, 1947. ISSN 0031899X. doi: 10.1103/PhysRev.71.622. (Cited on pages 2, 4, and 5.)

[126] Joel I-Jan Wang, Yafang Yang, Yu-An Chen, Kenji Watanabe, Takashi Taniguchi, Hugh O. H. Churchill, and Pablo Jarillo-Herrero. Electronic Transport of Encapsulated Graphene and WSe <sub>2</sub> Devices Fabricated by Pick-up of Prepatterned hBN. *Nano Letters*, 15(3):1898–1903, 2015. ISSN 1530-6984. doi: 10.1021/nl504750f. URL `http://pubs.acs.org/doi/abs/10.1021/nl504750f`. (Cited on pages 69, 70, 82, and 104.)

[127] L Wang, I Meric, P Y Huang, Q Gao, Y Gao, H Tran, T Taniguchi, K Watanabe, L M Campos, D a Muller, J Guo, P Kim, J Hone, K L Shepard, and C R Dean. One-dimensional electrical contact to a two-dimensional material. *Science (New York, N.Y.)*, 342(6158):614–7, 2013. ISSN 1095-9203. doi: 10.1126/science.1244358. URL `http://www.ncbi.nlm.nih.gov/pubmed/24179223`. (Cited on pages 64, 70, and 116.)

[128] Hideaki Wasa, Kiyotaka, Kitabatake, Makoto, Adachi. *Thin Films Material Technology - Sputtering of Compound Materials*. Springer-Verlag Berlin Heidelberg, 2004. URL `http://www.springer.com/us/book/9783642059315`. (Cited on page 41.)

[129] Kenji Watanabe, Takashi Taniguchi, and Hisao Kanda. Direct-bandgap properties and evidence for ultraviolet lasing of hexagonal boron nitride single crystal. *Nature materials*, 3(6):404–9, jun 2004. ISSN 1476-1122. doi: 10.1038/nmat1134. URL `http://dx.doi.org/10.1038/nmat1134`. (Cited on page 64.)

[130] J. R. Williams, L. DiCarlo, and C. M. Marcus. Quantum hall effect in a gate-controlled p-n junction of graphene. *Science*, 317 (5838):638–641, 2007. (Cited on page 72.)

[131] J. R. Williams, D. a. Abanin, L. Dicarlo, L. S. Levitov, and C. M. Marcus. Quantum Hall conductance of two-terminal graphene devices. *Physical Review B - Condensed Matter and Materials Physics*, 80(4):1–7, 2009. ISSN 10980121. doi: 10.1103/PhysRevB. 80.045408. (Cited on page 54.)

[132] Fengnian Xia, Vasili Perebeinos, Yu-ming Lin, Yanqing Wu, and Phaedon Avouris. The origins and limits of metal-graphene junction resistance. *Nat. Nano.*, 6(3):179–184, 03 2011. (Cited on page 124.)

[133] Jiamin Xue, Javier Sanchez-Yamagishi, Danny Bulmash, Philippe Jacquod, Aparna Deshpande, K. Watanabe, T. Taniguchi, Pablo Jarillo-Herrero, and Brian J. LeRoy. Scanning tunnelling microscopy and spectroscopy of ultra-flat graphene on hexagonal boron nitride. *Nature Materials*, 10(4): 282–285, 2011. ISSN 1476-1122. doi: 10.1038/nmat2968. URL `http://www.nature.com/doifinder/10.1038/nmat2968`. (Cited on pages ix, 64, and 65.)

[134] Matthew Yankowitz, Jiamin Xue, Daniel Cormode, Javier D. Sanchez-Yamagishi, K. Watanabe, T. Taniguchi, Pablo Jarillo-Herrero, Philippe Jacquod, and Brian J. LeRoy. Emergence of superlattice Dirac points in graphene on hexagonal boron nitride. *Nature Physics*, 8(5):382–386, mar 2012. ISSN 1745-2473. doi: 10.1038/nphys2272. URL `http://dx.doi.org/10.1038/nphys2272`. (Cited on page 63.)

[135] Duhee Yoon, Young-Woo Son, and Hyeonsik Cheong. Negative thermal expansion coefficient of graphene measured by Raman spectroscopy. *Nano letters*, 11(8):3227–31, aug 2011. ISSN 1530-6992. doi: 10.1021/nl201488g. URL `http://dx.doi.org/10.1021/nl201488g`. (Cited on page 66.)

[136] Andrea F. Young and Philip Kim. Quantum interference and Klein tunneling in graphene heterojunctions. *Nature Physics*, 5 (3):13, 2008. ISSN 1745-2473. doi: 10.1038/nphys1198. URL `http://arxiv.org/abs/0808.0855`. (Cited on pages 72, 80, and 81.)

[137] P. J. Zomer, M. H. D. Guimarães, J. C. Brant, N. Tombros, and B. J. van Wees. Fast pick up technique for high quality heterostructures of bilayer graphene and hexagonal boron nitride. *Applied Physics Letters*, 105(1):013101, jul 2014. ISSN 0003-6951. doi: 10.1063/1.4886096. URL `http://scitation.aip.org/`

content/aip/journal/apl/105/1/10.1063/1.4886096. (Cited on pages 64 and 104.)

[138] A Yu Zyuzin. Superconductor–normal-metal–superconductor junction in a strong magnetic field. *Physical Review B*, 50(1):323, 1994. (Cited on page 39.)